

**NANOSTRUCTURED OXYGEN CARRIERS FOR CHEMICAL LOOPING
COMBUSTION AND CHEMICAL LOOPING HYDROGEN PRODUCTION**

by

Rahul Dushyantrao Solunke

Bachelor in Chemical Engineering,

Institute of Chemical Technology (formerly UDCT), Mumbai, India, 2006

Submitted to the Graduate Faculty of
Swanson School of Engineering in partial fulfillment
of the requirements for the degree of
Doctor of Philosophy

University of Pittsburgh

2010

UNIVERSITY OF PITTSBURGH
SWANSON SCHOOL OF ENGINEERING

This dissertation was presented

by

Rahul Dushyantrao Solunke

It was defended on

September 28, 2010

and approved by

Robert Enick, PhD, Professor, Department of Chemical and Petroleum Engineering

Joseph McCarthy, PhD, Professor, Department of Chemical and Petroleum
Engineering

Rongchao Jin, PhD, Professor, Department of Chemistry, Carnegie Mellon University

Dissertation Director: Götz Vesper, PhD, Professor, Department of Chemical and
Petroleum Engineering

Copyright © by Rahul Dushyantrao Solunke

2010

NANOSTRUCTURED OXYGEN CARRIERS FOR CHEMICAL LOOPING COMBUSTION AND CHEMICAL LOOPING HYDROGEN PRODUCTION

Rahul Dushyantrao Solunke, PhD

University of Pittsburgh, 2010

Chemical looping combustion (CLC) is an emerging technology for clean energy-production. In CLC, an oxygen carrier is periodically oxidized with air and then reduced in contact with a fuel. CLC is thus a flame-less oxy-fuel combustion without an air separation unit, producing sequestration-ready CO₂-streams without significant energy penalty. However, a major hurdle towards technical implementation of CLC is the development of robust oxygen carrier materials.

In this thesis, we report on a combined study of theoretical and experimental investigations of oxygen carriers for CLC. A detailed thermodynamic screening of oxygen carriers based on several comparison criteria was carried out to come up with the best candidates for CLC and then effect of sulfur contamination in the fuel stream on the performance of these selected oxygen carriers was studied. In sulfur-free streams the carriers show stable and fast reduction and re-oxidation kinetics. Sulfur contamination results not only in sulfidation of the metal carrier component, but also in partial sulfidation of the support matrix which marginally alters the redox kinetics but does not affect carrier stability. Interestingly, the support sulfidation leads to a significant increase in the oxygen carrying capacity of the carriers. Further investigation of Cu-based carriers showed that efficient desulfurization of the fuel reactor exit stream is achievable with quantitative S-recovery in the air reactor effluent.

Beyond combustion, chemical looping can be used to produce hydrogen by replacing air with steam as oxidant in a ‘chemical looping steam reforming’ process (CLSR). The effluent of

the oxidizer is PEMFC-ready hydrogen without further purification steps, resulting in significant process intensification. Challenges in CLSR are slower steam vs air oxidation kinetics, high-temperature carrier stability, and attrition due to large solids transport in a two-bed process.

In the final part of the thesis, we report on experimental investigations of Fe-based nanostructured carriers to study their oxidation kinetics and high-temperature stability. Effect of temperature and particle size on hydrogen production and carrier utilization was studied which further demonstrated the importance of nano-sizing of the carrier. Finally, a reactor model was developed demonstrating that a fixed-bed approach is feasible for CLSR.

TABLE OF CONTENTS

ACKNOWLEDGEMENTS	XVI
1.0 INTRODUCTION.....	1
1.1 CHEMICAL LOOPING COMBUSTION (CLC)	3
1.1.1 Exergy	5
1.1.2 Brief insight into economic analysis	6
1.1.3 Literature review	7
1.2 HYDROGEN PRODUCTION BY CHEMICAL LOOPING STEAM REFORMING (CLSR).....	10
1.2.1 Literature review	12
2.0 THERMODYNAMIC EVALUATION OF OXYGEN CARRIERS.....	15
2.1 CLC OF SYNTHESIS GAS USING METALS AS OXYGEN CARRIERS	16
2.1.1 Equilibrium syngas conversion.....	17
2.1.2 Coking	18
2.1.3 Effect of sulfur contamination	19
2.1.4 Thermal stability	20
2.1.5 Excess over stoichiometry	21
2.2 CLC OF SYNTHESIS GAS USING METAL SULFIDES AS OXYGEN CARRIERS	24

2.2.1	Equilibrium conversion and coking	25
2.2.2	Sulfur loss from metal sulfide	25
2.3	CLC OF NATURAL GAS USING METALS AS OXYGEN CARRIERS ..	27
2.3.1	Equilibrium conversion and selectivity.....	28
2.3.2	Selectivity towards hydrogen production and coking	29
2.3.3	Anomalous behavior of iron.....	30
2.3.4	Effect of sulfur contamination	32
2.4	SUMMARY	33
3.0	NANOCOMPOSITE OXYGEN CARRIERS FOR CHEMICAL LOOPING COMBUSTION OF SULFUR CONTAMINATED SYNTHESIS GAS	34
3.1	EXPERIMENTAL.....	35
3.1.1	Synthesis and characterization	35
3.1.2	Reactive tests	38
3.2	RESULTS AND DISCUSSION	39
3.2.1	Structural stability	39
3.2.2	Ni-BHA.....	42
3.2.3	Cu-BHA	47
3.2.4	Material balance calculations	51
3.2.5	Effect of BaSO ₄ on oxygen carrying capacity	52
3.3	SUMMARY	54
4.0	INTEGRATING DESULFURIZATION WITH CO ₂ CAPTURE IN CHEMICAL LOOPING COMBUSTION	55
4.1	CHOICE OF THE CARRIER	57

4.2	EXPERIMENTAL.....	58
4.2.1	Synthesis and characterization	58
4.2.2	Reactive tests	60
4.3	RESULTS AND DISCUSSION	61
4.3.1	Reactivity of Cu-BHA.....	61
4.3.2	Cyclic operation with sulfur free synthesis gas	62
4.3.3	Impact of sulfur contaminants.....	63
4.3.4	Cyclic operation with sulfur containing synthesis gas.....	65
4.3.5	Mechanism of sulfidation	67
4.3.6	Effect of BaSO₄ on sulfidation of CuO	69
4.3.7	Effect of temperature.....	70
4.4	SUMMARY	76
5.0	HYDROGEN PRODUCTION VIA CHEMICAL LOOPING STEAM REFORMING (CLSR) IN A PERIODICALLY OPERATED FIXED BED REACTOR.....	77
5.1	CHOICE OF THE CARRIER	78
5.2	EXPERIMENTAL.....	81
5.2.1	Synthesis and characterization	82
5.2.2	Reactive tests	83
5.3	RESULTS AND DISCUSSION	84
5.3.1	Thermal stability	84
5.3.2	Effect of temperature.....	87
5.3.3	Effect of particle size.....	89

5.3.4	Fixed bed reactor calculations	91
5.4	SUMMARY	96
6.0	SUMMARY AND OUTLOOK.....	98
6.1	SUMMARY	98
6.1.1	CLC of sulfur contaminated synthesis gas	98
6.1.2	Hydrogen production via CLSR in periodically operated fixed bed reactor	99
6.2	OUTLOOK.....	100
6.2.1	Non-reducible and sulfur resistant supports for CLC with sulfur capture	100
6.2.2	Fe supported on silica for CLSR	101
APPENDIX A		102
BIBLIOGRAPHY		103

LIST OF TABLES

Table 1. NG-fired CC v/s SC-CA v/s CLC (400MW capacity) [9].....	7
Table 2. Composition of syngas obtained from EASTMAN gasifier, Morgantown, WV	17
Table 3. Composition of natural gas[35]	28
Table 4. Composition of syngas used for TGA tests	39
Table 5. A typical recipe for Cu-BHA (40.04 wt% Cu) synthesis	102

LIST OF FIGURES

Figure 1. Schematic for chemical looping combustion using syngas	4
Figure 2. Schematic of chemical-looping steam reforming (CLSR) using syngas as fuel	11
Figure 3. Equilibrium conversion of syngas using metals (left), resistance of metals to coking (right)	18
Figure 4. Resistance of metals to sulfide formation during syngas combustion	20
Figure 5. Thermal stability of solids in CLC	21
Figure 6. Equilibrium syngas conversion v/s excess Fe_2O_3 (left), equilibrium syngas conversion v/s excess Fe_2O_3 at 1200°C (right)	22
Figure 7. Different iron oxide phases at equilibrium at 1200°C (left), gas phase distribution at equilibrium at 1200°C (right).....	23
Figure 8. Equilibrium conversion of syngas (left), coke formation when different metal sulfides were used as oxygen carrier (right).....	25
Figure 9. Permanent sulfur loss from metal sulfate in fuel reactor, in one reduction cycle (left), equilibrium composition of CaCO_3 and H_2S in fuel reactor after first reduction cycle (right)	26
Figure 10. Equilibrium natural gas conversion v/s temperature (left), selectivity of metal oxides towards complete combustion (right)	29
Figure 11. Selectivity towards hydrogen production (left), coke formation (right)	30
Figure 12. Temperature dependent reduction of Fe_2O_3	31
Figure 13. Resistance of Oxygen carriers to sulfide formation during natural gas combustion...	32
Figure 14. Schematic synthesis of nanocomposite oxygen carriers	37

Figure 15. TEM image of a typical nanocomposite Ni-BHA (37wt% Ni).....	38
Figure 16. XRD patterns of NiO-BHA after 30 min. exposure to 10,000 ppm H ₂ S in Ar at 300 ⁰ C (top left), 500 ⁰ C (top right), 700 ⁰ C (bottom left) and 800 ⁰ C (bottom right)	41
Figure 17. XRD pattern of NiO-BHA after exposure to 10,000 ppm H ₂ S in argon for 30 min (see also figure 16, bottom right graph) and re-oxidization in air at 800 ⁰ C.....	42
Figure 18. BET pore analysis of NiO-BHA before, after sulfidation and after re-oxidation at 800 ⁰ C.....	42
Figure 19. Sample weight versus time for Ni-BHA during cyclic TGA redox experiments at 900 ⁰ C with sulfur-free syngas (t=125-300 min), followed by sulfur-contaminated syngas (t=300 – 500min), and again by sulfur-free syngas (t>550 min, as indicated by the shadings)	43
Figure 20. Effect of H ₂ S on redox kinetics of Ni-BHA: Conversion during a single redox cycle before (dotted line), during (solid line), and after sulfur exposure (dashed line; T= 900 ⁰ C)	45
Figure 21. Sample weight versus time for Cu-BHA during cyclic TGA redox experiments at 900 ⁰ C with sulfur-free syngas (t=35-190 min), followed by sulfur-contaminated syngas (t=190 – 490 min), and again by sulfur-free syngas (t >4900 min, as indicated by the shadings)	48
Figure 22. Effect of H ₂ S on redox kinetics of Cu-BHA: Conversion during a single redox cycle before (dotted line), during (solid line), and after sulfur exposure (dashed line; T= 900 ⁰ C)	49
Figure 23. Schematic for material balance calculations	51
Figure 24. Extent of sulfidation per cycle: Ni-BHA (left) and Cu-BHA (right)	52
Figure 25. Effect of H ₂ S on oxygen carrying capacity (as percentage of total reduced carrier weight) in subsequent redox cycles with S-contaminated syngas for Ni-BHA (left) and Cu-BHA (right)	53
Figure 26. Schematic representation of a CLC process scheme with integrated sulfur capture...	56
Figure 27. Equilibrium amount of sulfur species in the reducer exhaust at 900 ⁰ C, 30 atm for select oxygen carriers (left); and the equilibrium amount of sulfur species for Cu as function of temperature (T =600-1000 ⁰ C, P= 30 atm; right graph).....	58
Figure 28. TEM image of a typical nanocomposite Cu-BHA (40wt% Cu).....	59

Figure 29. Nitrogen adsorption isotherm (left) and pore size distribution (right) of 40wt% Cu-BHA	60
Figure 30. XRD diffractogram of Cu-BHA reduced in sulfur-free syngas (left) and re-oxidized in air (right) at 900°C	61
Figure 31. Top: Select representative redox cycles for Cu-BHA oxidized and reduced in air and sulfur-free syngas, respectively (flow rates of syngas and air= 5 sccm, T= 900°C, P= 1atm). Bottom: Blow-up of a single reduction half-cycle (left) and oxidation half-cycle (right)	63
Figure 32. X-ray diffractogram of CuO-BHA reduced in syngas with 1% H ₂ S (left) and re-oxidized in air at 900°C (right)	65
Figure 33. Reduction of CuO-BHA in syngas with 1% H ₂ S (left) and oxidation in air (right) at 900°C.....	67
Figure 34. Equilibrium constants for Cu, Cu ₂ O, and CuO sulfidation reactions between 600°C and 900°C.....	69
Figure 35. Reduction of CuO-BHA in syngas with 1% H ₂ S (left) and oxidation in air (right) at 700°C.....	71
Figure 36. Reduction of CuO-BHA in syngas with 1% H ₂ S (left) and oxidation in air (right) at 600°C.....	71
Figure 37. SO ₂ production during reduction (left) and oxidation (right) at three different temperatures (T= 600°C, 700°C, 900°C)	72
Figure 38. Sulfur species during the reduction (shaded) and oxidation (solid) at the three different temperatures	75
Figure 39. Equilibrium conversion of steam versus temperature for select metals and metal oxides (left), and Fe/oxide phases versus temperature for a stoichiometric FeO:steam ratio (right)	79
Figure 40. Fe/oxide phases v/s temperature for stoichiometric Fe ₃ O ₄ :syngas ratio (left), conversion of FeO to Fe ₃ O ₄ v/s excess steam for four different temperatures (right). Steam "excess" is defined relative to stoichiometric feed for complete conversion to Fe ₃ O ₄ (excess = 0). 100% excess thus refers to 2-fold stoichiometric supply	79
Figure 41. TEM image (left) and BET isotherm (right) of a typical nanostructured Fe-BHA (40wt% Fe) after calcination at 600°C.....	82
Figure 42. XRD spectra of Fe-BHA completely reduced in H ₂ at 800°C (left) and corresponding sample oxidized in steam at 500°C (right).....	83

Figure 43. Six redox cycles for Fe-BHA oxidized and reduced in a mixture of steam (98.5%) in Argon and syngas, respectively (top) and a single, enlarged reduction and oxidation cycle showing the gas phase concentrations	86
Figure 44. Hydrogen stream produced over one oxidation phase during steam oxidation of Fe-BHA at different temperatures (left), and corresponding carrier conversions (i.e. fractional oxidation) as function of time (right)	88
Figure 45. Particle size distribution of Fe-BHA calcined at 800°C (top left), 900°C (top right) and 1000°C (bottom).....	89
Figure 46. Effect of particle size of Fe on hydrogen production (left) and carrier conversion (right) at 800°C	90
Figure 47. Maximum temperature difference during oxidation with air or steam, and during reduction with syngas as a function of FeO loading in the fixed bed (left graph); and maximum temperature rise during oxidation with different diluted steam streams (right graph; steam weight fraction increasing from 5% to 100% from bottom to top; the balance is inert gas).....	94

NOMENCLATURE

C_p = heat capacity (J/kg.K)

ΔH_R = heat of reaction (J/ mol)

M_{act} = molecular weight of reactive component in solid carrier (kg/mol)

M_{H_2O} = molecular weight of steam (kg/mol)

T_0 = initial temperature (K)

T_{max} = maximum temperature (K)

ΔT_{max} = maximum temperature rise (K)

v_g = gas velocity (m/s)

v_h = heat front velocity (m/s)

v_r = reaction front velocity (m/s)

w_{act} = weight fraction of reactive component in solid carrier

w_{g,H_2O}^{in} = weight fraction of steam in the feed

ρ = density (kg/m³)

ε_s = porosity

ξ = stoichiometric factor (ratio of number of moles of gas to moles of solid in the oxidation reaction)

ACKNOWLEDGEMENTS

First and foremost, I would like to thank my research advisor, Dr. Götz Vesper, not only for his valuable advice but also for the constant encouragement and support during my four years in his group. His way of leading the group is exceptional and I always enjoyed our discussions. His group seminar was a really great platform to improve my presentation skills and to keep myself updated with what others were doing. He has been like a friend, a mentor and a father whenever I needed him most. Götz, hats off to you!!!

I would like to thank my lab mates Tengfei Liu, Tom Sanders, Katie Barillas, Gianalfredo Rossi, Yi Zhang, Shuang Liang, Lu Zhang, Michelle Najera, Sen Liu, Anmin Cao, Yanan Wang, Saurabh Bhavsar and Karen Uffalussy for their help and cooperation in the lab. I would also like to thank Dr. Jason Monnell for his help in TGA studies and DOE-NETL for their funding for my research.

In addition, I would like to thank the faculty, staff and students of the Chemical Engineering Department and Material Science Department at the University of Pittsburgh for their friendly support and help.

Last but not the least; I salute my parents and sister for giving me the strength to achieve this dream. This was not possible without you!

1.0 INTRODUCTION

In the last decades, significant research has been carried out to better understand the world climate and the long-term impact of climate change. There is now evidence that the mean annual temperature at the earth's surface increased over the past 200 years [1]. This temperature increase is commonly known as global warming. Emissions of greenhouse gases, CO_2 , NO_x , SO_x , CH_4 , is considered as main contributor to global warming and among these gases CO_2 is the most common gas emission. Combustion of fossil fuels releases a significant amount of carbon dioxide into the atmosphere. It is estimated that total carbon dioxide released from fossil fuel based power generation is about one third of the total carbon dioxide released from fuel combustion [2]. One obvious approach to minimize CO_2 emissions is to increase the use of renewable energy resources, such as biomass, solar and wind energies. Being renewable, these alternative energy sources have the intrinsic advantage of not generating CO_2 or contributing with a zero net CO_2 emissions. However, considering their current state of development and/or availability, it is almost impossible for them to fully replace the existing fossil fuels-based power generation. Thus, we heavily depend on the use of fossil fuels as the dominant source for the world's energy, and no significant change is anticipated for the next few decades [3]. Thus, in the near future power generation via fossil fuel combustion with efficient CO_2 capture is going to be the key contributor to world's energy supply. The CO_2 capture can be done by number of available processes which can be broadly classified in three categories as follows: (i) pre-combustion, in which the fuel is de-carbonized prior to combustion (ii) oxy-fuel combustion, in

which pure oxygen obtained from the cryogenic separation of nitrogen from air is used and (iii) post-combustion, in which CO₂ is separated from flue gases using different capture technologies. There are number of technologies currently available for CO₂ capture although the majority of them were not specifically developed for CO₂ sequestration. These processes have been practiced for a long time in chemical and petrochemical industries [1]. They are based on physical and chemical separation of CO₂ which includes absorption, adsorption, cryogenic separation and membrane separation. Absorption techniques use a suitable solvent to absorb CO₂ from the flue gas stream. Alkanolamines such as monoethanolamine (MEA) and diethanolamine (DMEA) are typically used in chemical absorption while methanol, dimethylether, polyethylene glycol and sulfolane are used in physical absorption [1]. Equipment corrosion in presence of oxygen and the energy intensive solvent regeneration are the major bottlenecks in absorption techniques. In addition, the presence of common flue gas contaminants such as SO_x, NO_x can negatively impact the process performance.

Adsorption capture technologies use a solid adsorbent such as zeolites, alumina and activated carbon to selectively adsorb CO₂ from flue gases. These techniques require energy intensive adsorbent regeneration. Porous membranes separate gas molecules based on their sizes. Major drawback of membrane separation is its low gas throughput which makes a multistage operation a must and hence makes the process energy intensive.

All these techniques are energy intensive and hence introduce a significant penalty on the overall power plant efficiency and therefore result in a net increase in the price of the produced electricity. Considering all these factors, chemical-looping combustion (CLC) appears to have the potential to stand out as an efficient and low cost technology. This process was initially

proposed to increase thermal efficiency in power plants, but later on proposed as a technology with inherent CO₂ capture with minimal energy losses [4-5].

1.1 CHEMICAL LOOPING COMBUSTION (CLC)

Chemical looping combustion (CLC) is a novel combustion technology which offers an elegant and highly efficient route towards clean fossil fuel combustion [6]. In CLC, the combustion of a fuel is broken down into two, spatially separated steps (see figure 1): The oxidation of an oxygen carrier (typically a metal or metal sulfide) with air, and the subsequent reduction of this carrier via reaction with a fuel (i.e. combustion). After combustion, the reduced metal is transferred back to the oxidation stage, closing the materials “loop”. Among the main advantages of the CLC concept are the fact that the combustion is flame-less, it operates at sufficiently low temperatures to avoid NO_x formation in the air-blown oxidizer, and it completely suppresses prompt-NO_x formation by avoiding any contact between the fuel and air. Finally, CLC ideally produces a pure mixture of CO₂ and H₂O as combustion gases, from which high-concentration, high-pressure (i.e. sequestration-ready) CO₂-streams can be easily produced by condensation of water. Thus, the concept results in no significant efficiency penalty for CO₂ capture, making it rather unique among current and emerging capturing technologies [7-8].

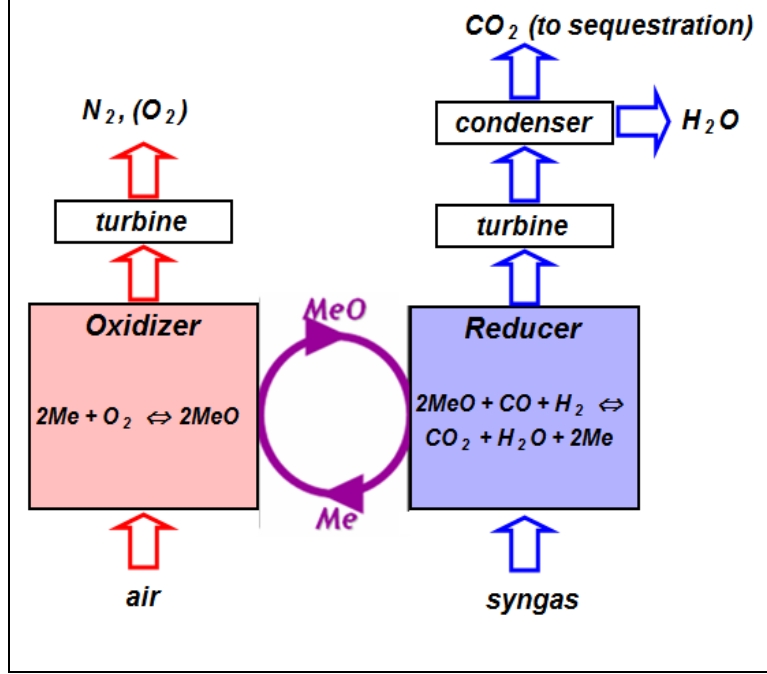
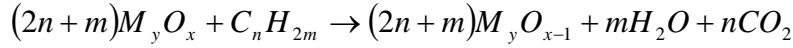
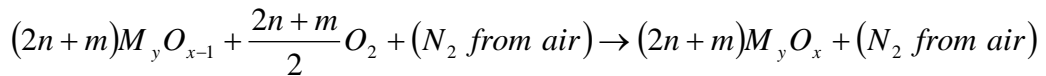


Figure 1. Schematic for chemical looping combustion using syngas

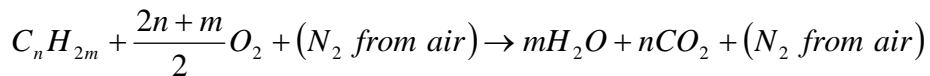
A generalized combustion reaction in the fuel reactor can be written as follows:



Once fuel combustion is complete the reduced metal oxide M_yO_{x-1} (or metal) is transferred back to the air reactor where it is re-oxidized according to the following reaction:



Thus, the overall reaction of the entire process is simply the conventional combustion of fuel using air,



The reduction reaction in the fuel reactor is generally endothermic whereas the oxidation reaction in the air reactor is exothermic. Heat of the reaction in the fuel reactor depends on fuel type and on the metal oxide used as oxygen carrier. However the net total heat evolved for the

combined reduction and oxidation steps remains the same, as the one in a conventional combustion where the fuel is burned in direct contact with air. Thus, CLC does not bring any enthalpy gains or losses; given the overall heat generation is equal to the heat of combustion of fuel. Its major advantage, however, is the inherent separation of CO₂ from the flue gases. In addition, CLC also minimizes NO_x formation since the fuel burns in the fuel reactor in an air free environment and the reduced oxygen carrier is re-oxidized in the air reactor at a temperature (usually lower than 1200°C) which is low enough to avoid any NO_x formation.

1.1.1 Exergy

Exergy is a measure of the maximum theoretical work that can be extracted from a combined system of a process and the environment as the process passes from one given state to the equilibrium with the environment. When the process comes to equilibrium with the environment the net exergy of the system is zero. Exergy in contrast to energy is destroyed in all real processes and can not be recovered. An exergy analysis can be used for evaluating new processes by testing if the new process has lower exergy destruction than the original process.

Two step combustion of the fuel in CLC is claimed to reduce exergy destruction in combustion [7]. A detailed exergy analysis showed that in CLC with Ni as oxygen carrier 7% lesser exergy is destroyed than conventional combustion power plant [7]. The same exergy analysis showed that CLC has 12.5% higher exergetic power efficiency, which is the fraction of fuel energy converted into net power output, and approximately 8% lesser exergy leaving the power plant in exhaust gases [7]. The analysis does not consider the major advantage of CLC which is inherent CO₂ capture, which when taken into account makes the process even more superior to conventional combustion.

1.1.2 Brief insight into economic analysis

Table 1 summarizes a case study that compares the natural gas fired combined cycle (NG-fired CC) power plant, semi-closed cycle power plant with chemical absorption (SC-CA) for CO₂ capture and unfired CLC power plant [9] based on the net plant capacity, capital cost, electricity cost and net CO₂ emissions. The CLC plant considered for economic assessment was sized to a power output of about 400 MW, to avoid discrepancies coming from different scales. It can be observed that CLC gives higher net power output than NG-fired CC and this is because of the lesser exergy destruction in CLC as discussed in previous section 1.1.1. The decrease in net plant power (~11%) in SC-CA compared to NG-fired CC is due to the energy penalty it receives from the separation process whereas there is no such energy penalty on CLC because of an in-situ separation of CO₂. The CO₂ emissions in NG-fired CC are suppressed by ~90% in SC-CA whereas there are absolutely no CO₂ emissions from CLC plant and these reductions in CO₂ emissions come at the expense of increased electricity cost, highest being in CLC. The analysis assumes that conventional NG-fired CC power plant has no restrictions on CO₂ emissions while calculating the cost of electricity. However if the currently followed regulations on CO₂ emissions are considered the conventional power plant must account for its CO₂ emissions which will significantly increase the electricity cost.

In conclusion, although the available technologies for CO₂ capture are technically mature enough to be implemented at large-scale they are highly energy intensive and as a result quite costly. Thus, CLC offers great opportunity to eliminate the energy intensive CO₂ removal steps minimizing sequestration cost. However, at its present status this technology is probably not mature enough to be implemented in a commercial scale. Therefore in the last several years,

numerous research and development efforts have been addressed towards the establishment of this promising process.

Table 1. NG-fired CC v/s SC-CA v/s CLC (400MW capacity) [9]

Parameter	NG-fired CC	SC-CA	CLC
Net plant capacity (MW)	373	332	403
CO ₂ emission rate (g/kWh)	356	36	~0
Cost of electricity (€/MWh)	40	51	59
Net capital cost (M€)	151	185	256

1.1.3 Literature review

In 1987, Ishida and coworkers first reported a CLC-based power generation for inherent CO₂ separation [5]. According to Ishida and coworkers, approximately 50–60% electrical efficiency can be obtained by employing a CLC integrated power generation system. In such process, the calculated CO₂ emission rate was 0.33 kg/kWh of produced electricity, which is significantly lower than the one of a conventional fossil fuel power plant.

In 1998, Anheden and Svedberg performed a detailed energy analysis for two different CLC gas turbine systems [7]. In the first system, methane was used as a fuel and NiO as oxygen carrier, while in the second system; the fuel employed was gasified coal (CO and H₂) and Fe₂O₃ as oxygen carrier. The power efficiency in both cases was 48%, which is comparable to the one of a conventional power generation station. However, taking into account the gains of inherent CO₂ separation, a CLC-based process offers higher overall energy efficiencies.

In 2005, Wolf et al. [10] and Wolf and Yan [11] developed a comparative analysis between a CLC and a MEA process for CO₂ capture in a conventional power generation station. According to this study, the energy losses in CLC are smaller than those experienced in conventional combustion, although the electrical efficiency of CLC is slightly lower. However, once the CO₂ separation is included in the calculation and given that CLC does not require additional energy for CO₂ capture, the CLC process provides a higher efficiency than the one for conventional combustion.

According to these studies CLC offers overall higher efficiencies compared to conventional fuel combustion with CO₂ capture by solvents. However, one should also realize that assessment of these efficiencies is normally based on the assumption of instantaneous reaction in air and fuel reactor and no deactivation of the oxygen carrier. Neither of these assumptions is true in practice and it may significantly affect the overall efficiencies. Both of these assumptions heavily rely on the choice of a proper oxygen carrier material which is one of the most essential parts of CLC.

It is well known that large scale application of CLC is contingent to the availability of suitable oxygen carriers. In fact the amount of the bed material in each reactor and the solid circulation rates between reactors mainly depends on the oxygen carrying capacity of the carriers. Therefore, a most important characteristic of a successful oxygen carrier is its reactivity in both reduction and oxidation cycles. In addition, its ability to completely combust a fuel is another important characteristic in order to achieve maximum fuel combustion efficiency. Furthermore, oxygen carrier particles should be thermally stable in repeated redox cycles at high temperatures, be fluidizable, be resistant to attrition and crushing, should not be hazardous to environment and should be economical.

Most of the technical literature on CLC is focused on developing the oxygen carrier material for CLC. Transition metal oxides such as copper, nickel, cobalt, iron and manganese are good candidates due to their favorable redox properties. Mattisson et al.[12-15] and Jernald et al. [16] reported a detailed thermodynamic analysis for a choice of an oxygen carrier. Both of these studies use a technique of Gibb's free minimization to calculate carrier reducibility and fuel conversion.

Apart from thermodynamics, Adanez et al. [17], Cho et al. [8] and Mattisson et al. [18] studied some other important physical properties such as density, active surface area, pore volume, particle size and crushing strength. The density and particle size not only determine the fluidizability of the oxygen carrier but also may affect the overall reaction rate, given their influence on mass and heat transfer inside the particles. The crushing strength of the particle is also an important property due to the physical stresses associated with fluidization.

Majority of the published work considers Fe, Cu and Ni as the candidates of choice. Fe and Cu are preferred due to their abundant availability, favorable thermodynamics and low cost, whereas Ni is chosen due to its superior redox kinetics and thermal stability. In order to increase the thermal stability and reactivity of these oxygen carriers they are supported on high temperature stable ceramics like SiO_2 , TiO_2 , Al_2O_3 , ZrO_2 and bentonite [2,8,13-14,16-26].

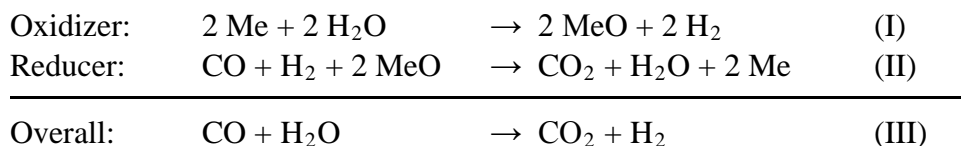
All these studies are based on sulfur-free fuel. However, in practice natural gas, syngas and coal, which are considered as fuel for CLC, contain significant amount of sulfur contamination which may interact with the oxygen carrier and can further impact the overall efficiency of CLC. Neither of these studies deals with the experimental investigation of effect of sulfur contamination in fuel on the performance of oxygen carriers. The major goal of our work

was to investigate the impact of sulfur contamination in fuel on the thermal stability and redox kinetics of the oxygen carriers in CLC. The results will be discussed in detail in chapter 3 and 4.

1.2 HYDROGEN PRODUCTION BY CHEMICAL LOOPING STEAM REFORMING (CLSR)

In principle, chemical looping combustion can process any combination of fuel and oxidizing gas as long as the oxygen carrier shows sufficient reactivity towards both reactants. The replacement of air with steam as oxidant is of particular interest, since in this case ultra-pure hydrogen is produced as effluent of the oxidizer after condensation of unreacted steam (figure 2) [27-29]. This process has a long history, dating back to the early decades of the 20th century, i.e. preceding recent development in chemical looping by many decades, and is historically often referred to as "steam-iron process" [30-31].

Utilizing steam as oxidant in a chemical looping process results in “chemical-looping steam reforming” (CLSR) as net reaction, which is illustrated here with synthesis gas ("syngas") as fuel:



where 'Me' represents the (typically metal-based) oxygen carrier, and MeO the corresponding metal oxide. Since chemical looping is a highly fuel-flexible process, syngas can be replaced with other fuels, such as methane (natural gas) or even coal, resulting in net reactions of methane steam reforming and coal gasification, respectively, albeit with the advantage over the respective

conventional processes of yielding “perfect” selectivity for hydrogen and inherently separating the hydrogen effluent from the carbon species.

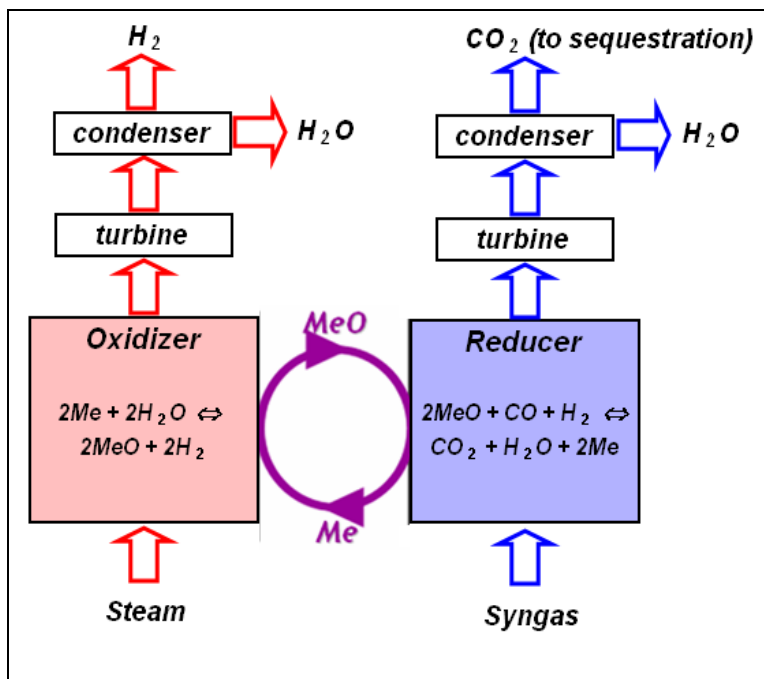


Figure 2. Schematic of chemical-looping steam reforming (CLSR) using syngas as fuel

If CLSR is operated with syngas the net reaction yields water-gas-shift (WGS), as seen in the sum reaction (III) above. However, conventional WGS is thermodynamically limited at high-temperature conditions and kinetically limited at low-temperature conditions, which requires a two-stage process in industrial practice [32]. In contrast, the chemical looping based WGS process can be run at high temperature without thermodynamic constraints, i.e. it allows to overcome the inherent thermodynamic limitations of WGS. By breaking the reaction down into two half-reactions via chemical looping the process can hence take full advantage of the fast reaction kinetics at high-temperature conditions. Since the steam/hydrogen stream is never contacted with the fuel, the typical problems with CO contamination of the hydrogen effluent in steam reforming and WGS processes are avoided, making additional clean-up of the hydrogen

stream via preferential oxidation (PROX), methanation, and/or other reaction or separation stages unnecessary. Overall, CLSR is hence an attractive, strongly intensified, fuel-flexible technology for PEM fuel cell-ready H₂ production from fossil or renewable fuels.

1.2.1 Literature review

Chemical looping steam reforming has a very long history dating back to the early decades of 20th century and it was referred as steam-iron process. In 1904, Howard Lane (an engineer in Birmingham, England) devised an apparatus to produce hydrogen by steam-iron process [33]. Hydrogen produced by this technique was used in inflating military balloons. The plant was awarded a silver medal for its scientific achievement. Later on in 1911, Messerschmitt filed a patent on steam-iron process for hydrogen production [30]. The concept was to pass steam over iron at proper temperature which converts iron into iron oxide, and in the process hydrogen is liberated. This reaction is carried out until iron can not take up any more oxygen. The iron is then regenerated by reducing the oxide to metallic iron by passing synthesis gas over the iron oxide. The major setback to this process was deactivation of iron particles after few oxidation-reduction cycles. This problem was never properly analyzed and meanwhile other process for hydrogen production like methane steam reforming, which was more efficient than steam-iron process, took over and steam-iron process lost attention.

Recently industry is looking at hydrogen as an alternative fuel and at the same time the focus is on minimizing the carbon foot-print. Steam-iron process has the potential to satisfy both of these needs i.e. hydrogen with low carbon foot-print, therefore this process is recently being developed. The focus of all current studies is to stabilize the iron particles in repeated high temperature redox cycles. Gupta et al. studied a syngas redox process to produce hydrogen from

coal derived syngas [29]. Ni, Cu, Cd, Co, Mn and Fe were evaluated based on the thermodynamic equilibrium limitations and Fe was found to be the best candidate for the redox process. Based on a thermo gravimetric analyzer (TGA) study they reported that composite particles with Fe_2O_3 as the key ingredient undergo multiple redox cycles without loss of the activity. A detailed process simulation showed that the process is capable of converting 74% of coal energy into hydrogen energy while inherently capturing the CO_2 produced during reduction of the carrier.

Galvita et al. studied a similar process, cyclic water gas shift (CWGS) reaction which involved use of Fe supported on $\text{CeO}_2\text{-ZrO}_2$ [27]. Syngas was used to reduce the oxidized carrier and steam was used to oxidize the reduced carrier and thereby producing hydrogen. Hydrogen produced by this method was used for a PEM fuel cell without any further purification steps. Some coke was formed due to Boudouard reaction which was oxidized by steam to carbon monoxide in re-oxidation step. The extent of coke formation was controlled by controlling the extent of reduction of the oxidized carrier. The feasibility of this process was demonstrated by combining CWGS reactor with a 5 cell PEMFC stack.

Ryden and Lyngfelt reported a similar approach to produce hydrogen by methane steam reforming in chemical looping combustion [34]. They reported co-feeding of natural gas and steam to the fuel reactor where it reacts with the iron oxide to produce reformer gas. This reformer gas is then fed to the water gas shift reactor to increase its hydrogen content which is then separated by pressure swing absorption. Upon reduction of iron oxide metallic iron is produced in the fuel reactor which is then oxidized back to the iron oxide in the air reactor. It is found that this process gives better selectivity towards hydrogen than conventional methane steam reforming due to lower reactor temperatures and favourable heat transfer conditions.

All these studies focus on the preparation of thermally stable and highly active material for hydrogen production via chemical looping carried out in a fluidized bed reactor configuration. We focus on the hydrogen production by CLSR in a fixed bed reactor where hot spots and heat accumulations can be more pronounced than in fluidized bed reactors. Thermal stability and reactivity of the material, effect of particle size on the hydrogen production, and a brief model describing the feasibility of fixed bed operation for CLSR will be discussed in chapter 5.

2.0 THERMODYNAMIC EVALUATION OF OXYGEN CARRIERS

The large-scale application of CLC depends on the availability of suitable oxygen carriers. They should have favorable oxidation and reduction thermodynamics, high oxidation and reduction capacity, mechanical stability under repeated oxidation/reduction cycles and thermal stability at operating temperature. Other important factors would be cost and environmental impact. This section focuses on comparative thermodynamic analysis of a wide range of metals and metal sulfides for CLC of syngas and natural gas. Thus, the analysis provides a guideline for selection of an oxygen carrier for more thorough kinetic studies required for actual implementation on commercial scale.

In order to evaluate the feasibility of different metals / metal sulfides for CLC an equilibrium analysis was carried out using the commercial software package 'Factsage 5.5'. Two types of fuel were considered for the analysis, syngas and natural gas. Composition of syngas used in the analysis was the same as the one obtained from EASTMAN gassifier at NETL, Morgantown and the composition of natural gas was same as the one obtained at Salt Lake, USA [35]. Equilibrium in the fuel reactor was studied for a stoichiometric mixture of fuel and oxidized oxygen carrier over a wide temperature range applicable to CLC and at a pressure varying from 1 to 30bar. In some instances analysis was repeated with excess amount of carrier required for complete fuel conversion. Fuel conversion, selectivity, resistance to coking, resistance to sulfide formation and thermal stability were the major criteria for comparison. Performance of a broad

range of metals and corresponding metal sulfides was evaluated. Only selected metals and metal sulfides are presented here for the discussion.

2.1 CLC OF SYNTHESIS GAS USING METALS AS OXYGEN CARRIERS

Table 2 shows the composition of the syngas used for the thermodynamic calculations. It can be seen that the syngas contains a significant amount of sulfur contamination (~10000ppm: H₂S, COS combined) and thus it is a good choice to analyze thermodynamic feasibility of oxygen carriers in a very harsh reducing atmosphere. The results are discussed in subsequent section.

A wide range of metals were analyzed and only those selected few which looked promising for CLC, based on the comparison criteria explained above, are shown here. Thermodynamic analysis was performed at pressures of 1 to 30bar but no significant effect of pressure was observed on the equilibrium conversion of syngas. This makes sense since the total number of moles of gaseous species remains same in the fuel reactor and hence pressure will not have any effect on the equilibrium conversion. However, for this particular study 30bar pressure is used for analysis for the following reasons -

- 1) Efficiency of the cycle in the CLC loop will be increased at higher pressures [36]
- 2) Having CO₂ as a high pressure gas at the outlet of CLC requires very small amount of additional power for further compression of the CO₂ for the sequestration [37]

Table 2. Composition of syngas obtained from EASTMAN gasifier, Morgantown, WV

Constituent	Composition (Vol %)
CH ₄	0.035
H ₂	30.8
CO	38
CO ₂	13
H ₂ O	16.5
H ₂ S	0.961
COS	0.061
N ₂	0.523
Ar	0.1218

2.1.1 Equilibrium syngas conversion

Figure 3 (left) shows the equilibrium conversion of syngas at different temperatures. It can be seen from the figure 3 (left) that for all oxygen carriers the equilibrium syngas conversion drops down with increasing temperature because for all of them syngas combustion is an exothermic process. The dashed black line represents the equilibrium for the homogeneous gas phase reaction in absence of any metal oxide. It can be seen from the plot that introducing metal oxides

significantly improves the fuel conversion and hence they may be used as oxygen carriers. Ni, Cu and Co show high equilibrium conversions and therefore they are the most suitable candidates for CLC.

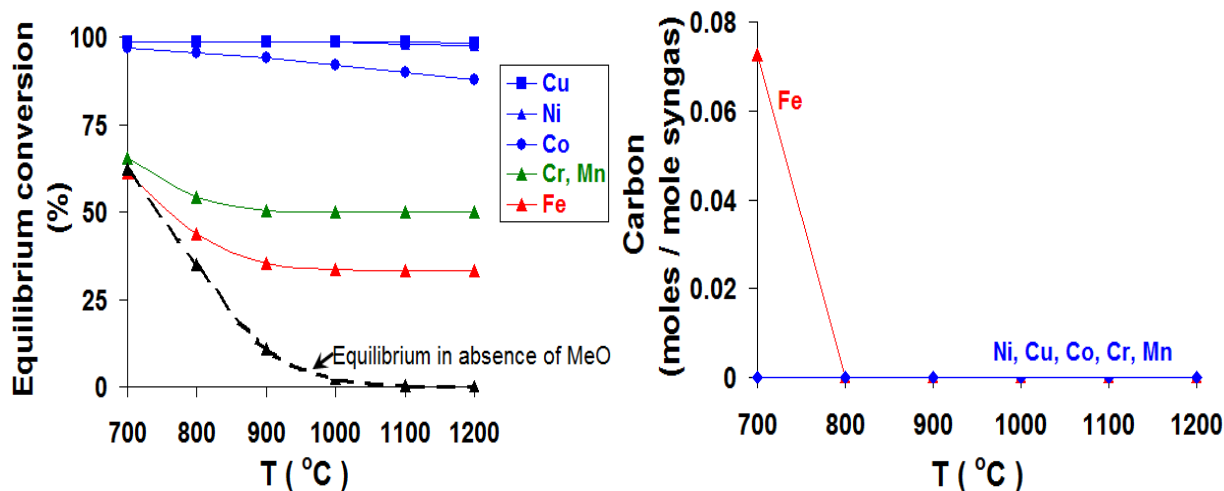


Figure 3. Equilibrium conversion of syngas using metals (left), resistance of metals to coking (right)

2.1.2 Coking

Hydrocarbon combustion over a solid material often results in coking at lower temperatures. At lower temperatures incomplete combustion is favored over complete combustion [38-40] and results in carbon residue deposition on the solid material used in the combustion. This carbon deposition on an oxygen carrier may block its availability for the reaction and hence might deactivate the carrier entirely. Hence it is worthwhile to look at the resistance of these oxygen carriers to coking in the CLC operating temperature regime. Figure 3 (right) shows resistance of different oxygen carriers to coking. Interestingly, all oxides show very high resistance to coking in the temperature range of 700 to 1200 °C except Fe_2O_3 which shows significant coking below 800°C. Hence if iron is used in CLC then one should operate CLC at a temperature above 800°C.

2.1.3 Effect of sulfur contamination

In fuel combustion, sulfur poisoning of the catalyst is a major concern. Sulfur shows very high affinity for metals. At low concentration it binds with the metal surface by physical adsorption while at high concentration it forms a chemical bond with the metal to form the corresponding metal sulfide [41]. Metallic oxygen carriers are no exception and they can easily get poisoned by sulfur under the CLC operating conditions. Once poisoned the activity of the metals for fuel combustion might drop down significantly and this may have direct impact on the attainable conversions. Also from the mechanical stability point of view, formation of metals sulfides may severely affect the structural stability of the carrier. Hence here we looked at the resistance of oxygen carriers to sulfur present in the synthesis gas. Figure 4 shows the extent of sulfidation of different oxygen carriers at different temperatures which is defined as:

Extent of sulfidation = Metal atoms in metal sulfide at equilibrium / total number of metal atoms

It can be seen that all oxygen carriers are prone to sulfide formation except Cr and for all of them the extent of sulfidation decreases with increase in temperature. Cu, Ni and Co turned out very efficient oxygen carriers in terms of fuel conversion but also are highly prone to sulfidation. Hence a detailed kinetic analysis for the sulfidation of these carriers is required before accepting or rejecting them for CLC. Cr is the only oxygen carrier which is highly robust to sulfidation at all temperatures but thermodynamically poor in terms of syngas conversion.

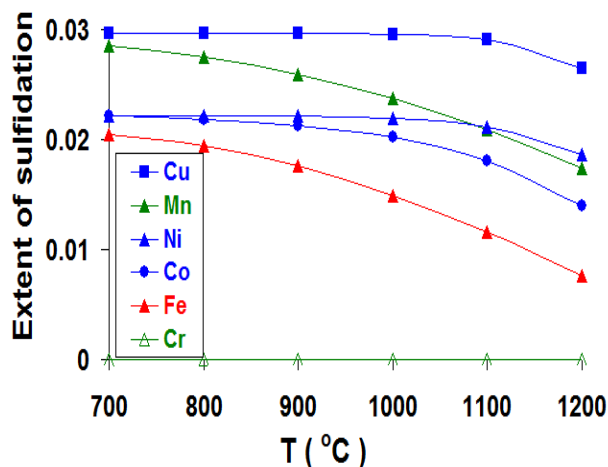


Figure 4. Resistance of metals to sulfide formation during syngas combustion

2.1.4 Thermal stability

CLC deals with metallic compounds at very high temperatures. Sintering is a major issue at such a high temperatures. Sintering of any of the metallic compounds present in the CLC loop will lead to pore plugging, agglomeration which eventually will lead to reduction in surface area of the carrier and hence the lowered throughputs. Therefore it is important to keep an eye on the thermal stability of the metallic compounds at the operating temperature of CLC. Figure 5 shows the melting points of metals, metal oxides and metal sulfides. All metals have melting point higher than 1200°C except Cu, which melts around 1080°C. 1200°C can be taken as an upper limit on the operating temperature of CLC. All metal oxides have melting point greater than 1200°C and hence they are thermally stable for CLC operation. Among the sulfides, Cu-sulfide, Ni-sulfide and Fe-sulfide have melting points lower than 1200°C and hence they are not thermally stable for CLC operating up to 1200°C. In particular Ni-sulfide has very low melting

point (around 750°C) which might completely eliminate Ni as oxygen carrier for sulfur contaminated syngas.

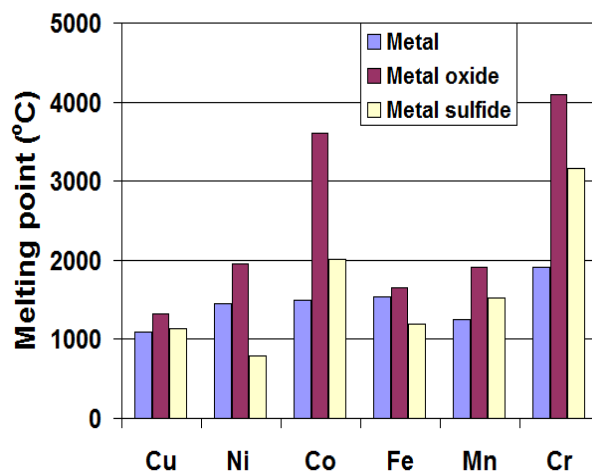


Figure 5. Thermal stability of solids in CLC

2.1.5 Excess over stoichiometry

Complete conversion of fuel into CO_2 and H_2O is very important in CLC. Any unreacted fuel will show up in the exhaust gases from the fuel reactor and must be separated from CO_2 before it goes to sequestration unit. In order to avoid this downstream separation complete conversion of fuel is necessary. From the above mentioned analysis it can be seen that only Ni and Cu give complete conversion at all temperatures. For all other carriers excess amount of carriers could be used in order to achieve complete syngas conversion. Among all the metals discussed above iron showed lowest conversion but least reactivity towards sulfur contamination in syngas and essentially no coke formation above 800°C. The major advantage iron has is its low cost and low toxicity compared to all other metals. Considering the fact that CLC involves a heavy solid transport, attrition of the carrier is a major hurdle in technical realization of the CLC. However,

if the carrier is as cheap as iron, one can tolerate high attrition rates by simply replacing the deteriorated carrier by fresh carrier. Hence there have been many studies focusing on the use of iron as oxygen carrier [10,13-14,26,42]. Thermodynamic calculations showed that equilibrium syngas conversion is not linearly dependent on excess amount of iron oxide used. In fact the results showed a very complex dependence of syngas conversion to excess amount of iron oxide used. Figure 6 (left) shows the effect of excess Fe_2O_3 on equilibrium syngas conversion. Clearly equilibrium syngas conversion has no linear relationship with the excess amount of Fe_2O_3 . In fact at all temperatures between 700°C and 1200°C four distinct zones exist. Figure 6 (right) shows such a plot at 1200°C .

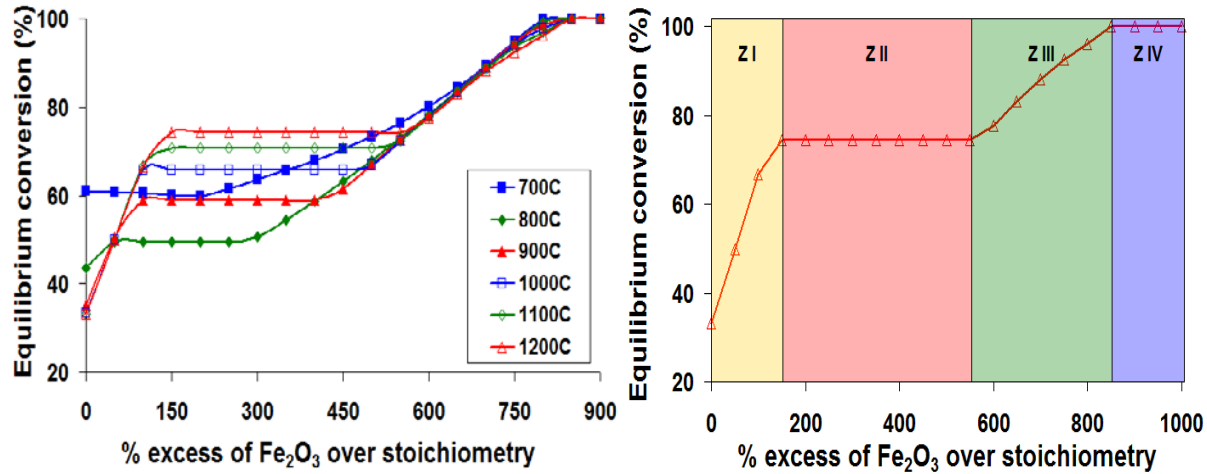


Figure 6. Equilibrium syngas conversion v/s excess Fe_2O_3 (left), equilibrium syngas conversion v/s excess Fe_2O_3 at 1200°C (right)

Figure 7 shows different iron oxide phases at equilibrium at 1200°C (left) and gas phase distribution at equilibrium when varying excess of Fe_2O_3 used for syngas combustion at 1200°C (right). It is evident from figure 7 that solid phase transformation is competing with syngas combustion. In zone I (0-150%) excess Fe_2O_3 reacts with syngas. In the process Fe_2O_3 is

reduced to FeO and the corresponding oxygen consumption can be seen in figure 7 (right) in the form of decreasing CO, H₂ and increasing CO₂ and H₂O.

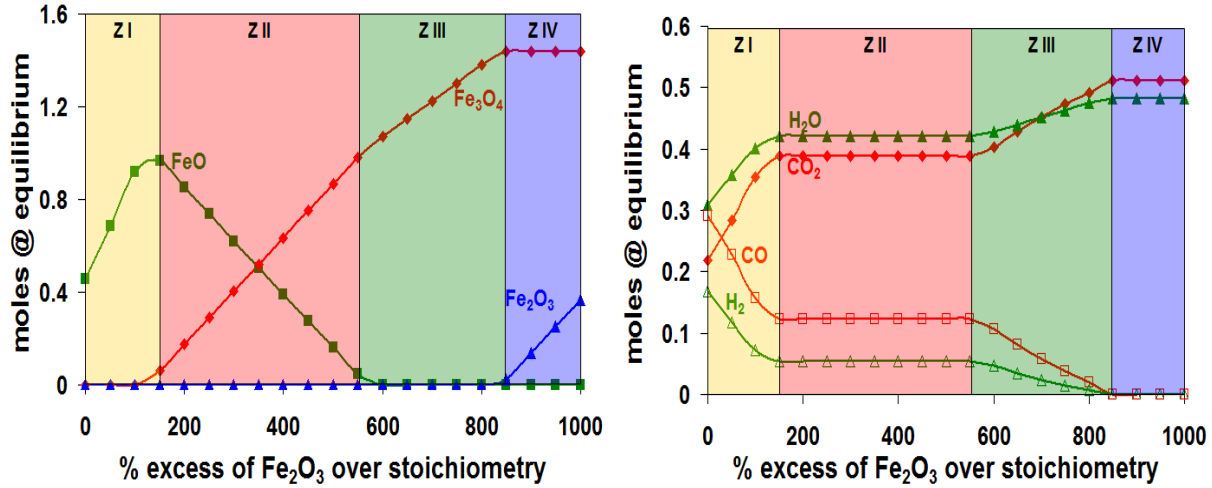


Figure 7. Different iron oxide phases at equilibrium at 1200°C (left), gas phase distribution at equilibrium at 1200°C (right)

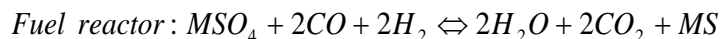
In zone II (150-550%) solid phase transformation is thermodynamically favored over the syngas combustion and hence despite the increase in excess amount of Fe₂O₃ there is no drop in equilibrium amounts of CO and H₂. The solid transformation results in consumption of FeO and formation of Fe₃O₄ phase as shown in figure 7 (left). In zone III (550-850%) Fe₂O₃ amount is so high that FeO is completely consumed in solid transformation reaction and then the surplus Fe₂O₃ reacts with the syngas. As a result syngas conversion increases. The equilibrium conversion finally attains maxima i.e. complete combustion of syngas around 850% excess. In zone IV (above 850%) no further change in equilibrium conversion occurs. Thus the range between ~180 to ~580% excess is a dead zone in terms of improvement in equilibrium syngas conversion. In reality it might not be feasible to use an excess beyond 600% as it may increase material cost, reactor cost, solid handling cost etc. Instead it may be more feasible to recycle the unreacted fuel. However it should be kept in mind that this is a thermodynamic evaluation and

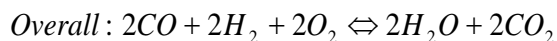
suggests only the feasibility or infeasibility of the process. Detailed kinetic studies must be carried out to correlate the thermodynamic results.

2.2 CLC OF SYNTHESIS GAS USING METAL SULFIDES AS OXYGEN CARRIERS

Metal sulfides can also act as oxygen carriers and are being considered an alternative to metals as oxygen carriers [43-44]. Metals have major disadvantage of getting poisoned in sulfur atmosphere. Metal sulfides inherently have sulfur present in their structure and are hence inherently sulfur resistant. Another major advantage metal sulfides have over metals is their higher oxygen carrying capacity. Metal sulfide (MS) can carry four oxygen atoms per mole of metal sulfate (MSO_4) whereas the oxygen carrying capacity of metals depend on the type of metal and metal oxide and it usually varies between one to three oxygen atoms per mole of metal oxide. This very high oxygen carrying capacity of metal sulfides can provide higher throughputs. A detailed thermodynamic analysis was carried out for a wide range of metal sulfides in order to see their feasibility in CLC. Only selected metal sulfides are shown here.

The reactions in air and fuel reactor when metal sulfide is used as oxygen carrier are as shown below,





2.2.1 Equilibrium conversion and coking

Pressures of 1 to 30bar were tested for their effect on the syngas conversion. Since very little effect of pressure on syngas conversion was observed a pressure of 30bar was selected for the further analysis. Figure 8 shows the equilibrium conversion of syngas (left) when CaS, MnS, Co₉S₈ and FeS were used as oxygen carriers. It can be seen that all of them give very high fuel conversion. Figure 8 (right) shows resistance to coking, which indicates that all of the metal sulfides are highly resistant to coking.

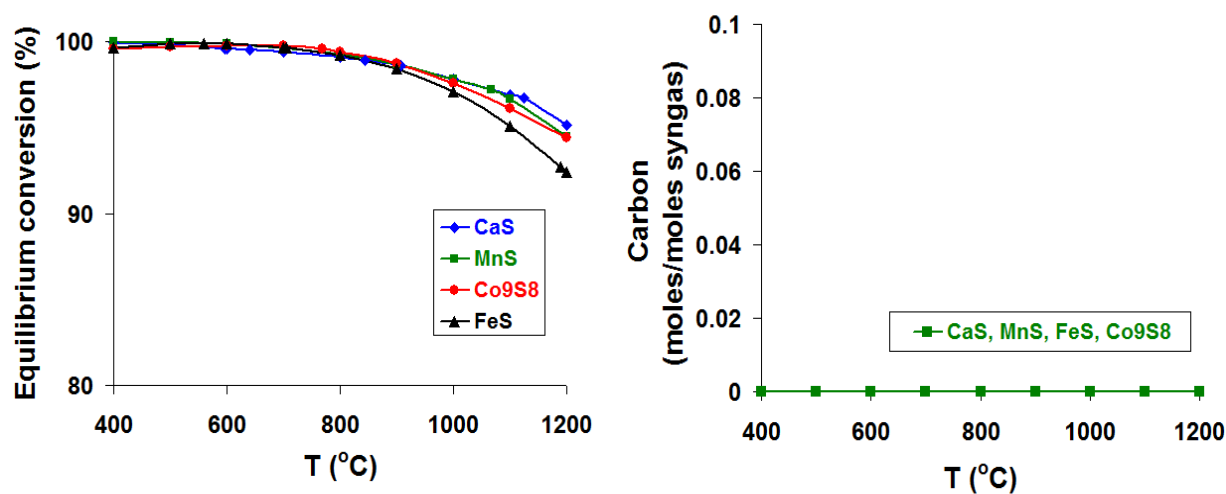


Figure 8. Equilibrium conversion of syngas (left), coke formation when different metal sulfides were used as oxygen carrier (right)

2.2.2 Sulfur loss from metal sulfide

While performing the calculations it was observed that gas phase at equilibrium had sulfur gases – H₂S, SO₂ and SO₃ along with CO, H₂, CO₂ and H₂O. This is important since this suggested that part of the sulfur associated with metal sulfide was lost in the fuel reactor in the first reduction cycle. Naturally this loss of sulfur will be extended to subsequent reduction cycles and

ultimately all the sulfur associated with metal sulfide will be gone and the CLC will come to a shut down. A careful analysis showed that depending on the temperature there exist two processes which were responsible for the sulfur loss from metal sulfates, thermal decomposition of sulfates at high temperature and carbonate formation at low temperature. Figure 9 (left) shows the permanent sulfur loss for different sulfates in one reduction cycle. It can be seen that all metal sulfides show permanent sulfur loss except Co-sulfide shows sulfur loss only above 1200°C because of thermal decomposition.

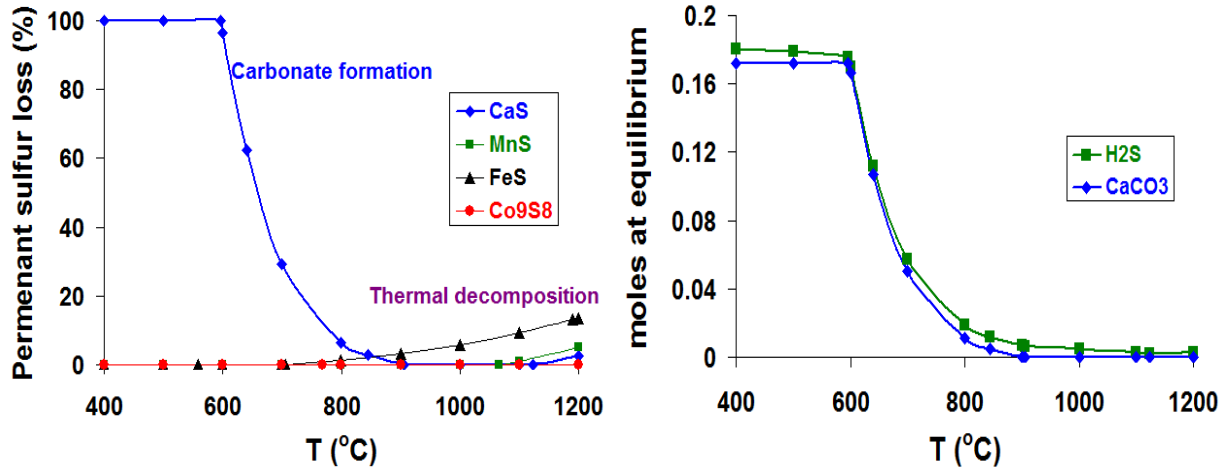
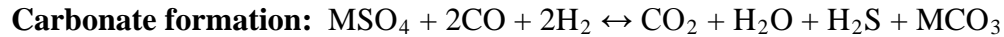


Figure 9. Permanent sulfur loss from metal sulfate in fuel reactor, in one reduction cycle (left), equilibrium composition of CaCO_3 and H_2S in fuel reactor after first reduction cycle (right)

Carbonate formation and thermal decomposition reactions are as shown below,



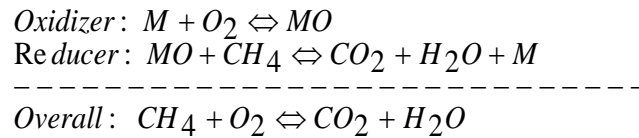
In carbonate formation, sulfur is lost via H_2S formation while in case of sulfate decomposition it is lost via sulfur dioxide and sulfur trioxide formation. Metal carbonates are generally not stable at high temperature and hence loss of sulfur via carbonate formation occurs at low temperatures. CaCO_3 is very stable in between 400°C and 600°C and hence CaSO_4 loses

all sulfur associated with it by forming CaCO_3 when reacted with syngas. As temperature increases thermal stability of CaCO_3 decreases and hence sulfur loss via carbonate formation decreases. Figure 9 (right) shows equilibrium moles of CaCO_3 and H_2S after the reduction. It shows that CaCO_3 and H_2S are formed in approximately equimolar amounts at equilibrium and hence supports the carbonate formation hypothesis. Thus, if one wants to utilize the potential of metal sulfides as oxygen carrier one must alter the kinetics in such a way that thermal decomposition of sulfates and the carbonate formation is minimized.

2.3 CLC OF NATURAL GAS USING METALS AS OXYGEN CARRIERS

Table 3 shows the composition of the natural gas used for the thermodynamic calculations which is same as the composition of sulfur-free natural gas obtained at Salt Lake, USA. Carrier performance was first analyzed using sulfur-free natural gas and then the effect of 1% H_2S contamination (with adjusted N_2 content) in the same natural gas was observed on the carrier performance. Along with the attainable equilibrium conversion, resistance to coking, resistance to sulfide formation and thermal stability, selectivity towards complete combustion was another important criterion. The results are discussed in subsequent sections.

The reaction scheme for natural gas combustion is as follows,



Again, the overall reaction is oxy-fuel combustion of natural gas.

Table 3. Composition of natural gas[35]

Constituent	Composition (Vol %)
CH ₄	95
C ₂ H ₆	0.8
C ₃ H ₈	0.2
CO ₂	3.6
N ₂	0.4

2.3.1 Equilibrium conversion and selectivity

Figure 10 (left) shows equilibrium natural gas conversion at different temperatures for selected metals. As observed in case of syngas combustion Cu, Ni and Co are highly efficient oxygen carriers for natural gas combustion as well. Mn, Cr and Fe are also good choices at temperatures above 1000°C. Equilibrium conversion dependence on temperature in case of Fe is not regular exponential but rather it shows a sharp increase followed by a slow increase and then the usual exponential increase to maximum equilibrium conversion. This shall be explained later in detail in sec. 2.3.3. Figure 10 (right) shows the selectivity towards complete combustion. Selectivity towards complete combustion decreases with increase in temperature for all carriers simply because partial combustion takes over at higher temperatures [38-40]. Again Fe shows a complex behavior of increase in selectivity below 720°C and this will be explained later in sec. 2.3.3.

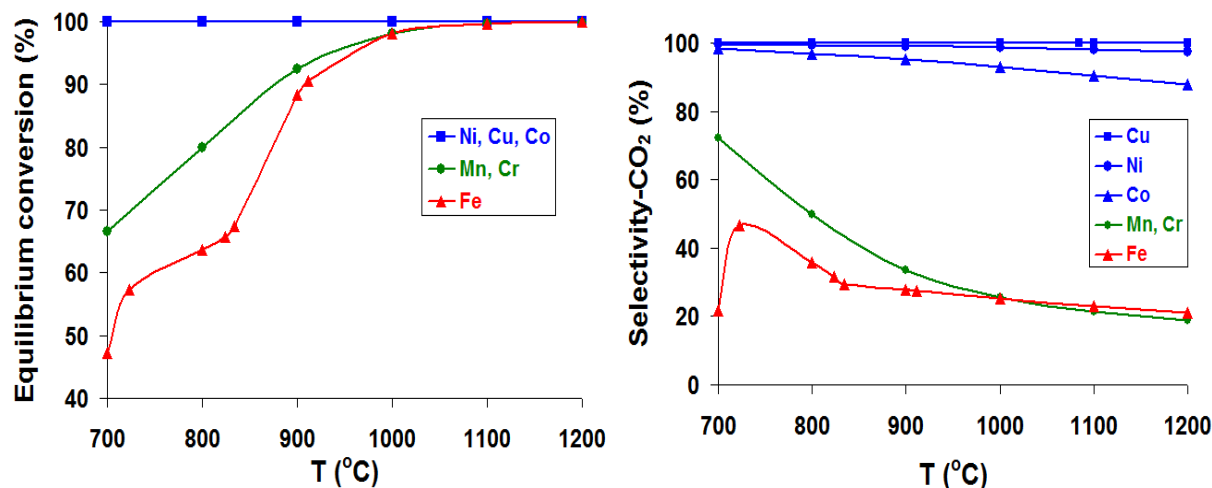


Figure 10. Equilibrium natural gas conversion v/s temperature (left), selectivity of metal oxides towards complete combustion (right)

2.3.2 Selectivity towards hydrogen production and coking

Fe, Mn and Cr give very high fuel conversion above 1000°C but very low selectivity towards complete combustion (see figure 10). Hence, it is interesting to see if these carriers are good for partial oxidation of methane and hence for the hydrogen production. Catalytic partial oxidation of methane is a well studied reaction in the literature [45-51] which motivates this analysis of using chemical looping combustion for simultaneous hydrogen production. Figure 11 (left) shows the selectivity of Mn, Cr and Fe towards hydrogen production. It can be seen that all of them show selectivity towards hydrogen production greater than 50% above 800°C. This might not be as high as obtained by catalytic partial oxidation of methane [51] but since these carriers are used in CLC process CLC can be tuned to produce hydrogen while maintaining its main purpose of combustion. This is just a hypothesis and should be evaluated with thorough kinetic studies.

Figure 11 (right) shows coke formation. Again, Ni, Cu and Co being highly efficient carriers are very robust to coking above 500°C. Cr and Mn show coking below 600°C. Fe once again shows complex behavior of increasing coke formation with increasing temperatures below 675°C. Above 675°C this coke formation decreases and above 830°C it is essentially zero.

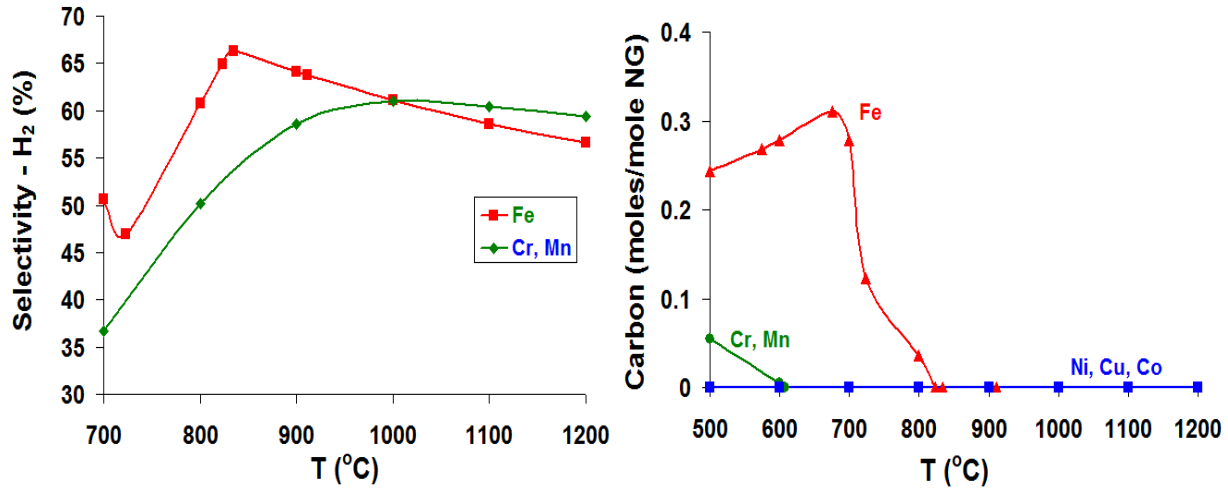


Figure 11. Selectivity towards hydrogen production (left), coke formation (right)

2.3.3 Anomalous behavior of iron

The complex behavior of Fe can be explained with the help of figure 12 which shows the iron oxide phases depending on the temperature. It also shows the net oxygen availability for the combustion based on temperature and the corresponding CO₂ production. Clearly the plot has four distinct zones of reduction. In zone I (500 to 675°C) Fe₂O₃ is completely reduced to Fe₃O₄ giving constant oxygen availability for the combustion. In zone II (675 to 720°C) reduction of Fe₂O₃ is stronger than that in zone I. Here Fe₂O₃ further reduced to FeO, therefore net oxygen availability for combustion strongly increases in this zone. As a result there is sharp increase in equilibrium conversion (see figure 10 (left)), selectivity towards complete combustion (see figure

10 (right)) and a sharp decrease in selectivity towards H_2 production (see figure 11 (left)) and coke formation (see figure 11 (right)). In zone III (720 to 830°C) Fe_2O_3 is completely reduced to FeO giving constant oxygen availability. At higher temperatures partial combustion takes over complete combustion hence in zone III, above 720°C, selectivity towards complete combustion decreases. Increase in equilibrium conversion in this zone is not as sharp as in zone II simply because the oxygen availability for combustion is constant. In zone IV (830 to 1200°C) FeO is reduced to Fe releasing more oxygen. With increase in temperature extent of reduction increases and finally above 1100°C equilibrium limit on reduction is reached as can be seen from flattening of FeO and Fe curves. Oxygen availability exponentially increases and hence equilibrium conversion sees one more sharp increase around 830°C finally attaining the complete conversion above 1100°C. Due to exponential increase in oxygen availability decrease in the selectivity towards complete combustion is not as sharp as in zone III (see figure 10 (right)) and the selectivity towards H_2 production decreases (see figure 11 (left)).

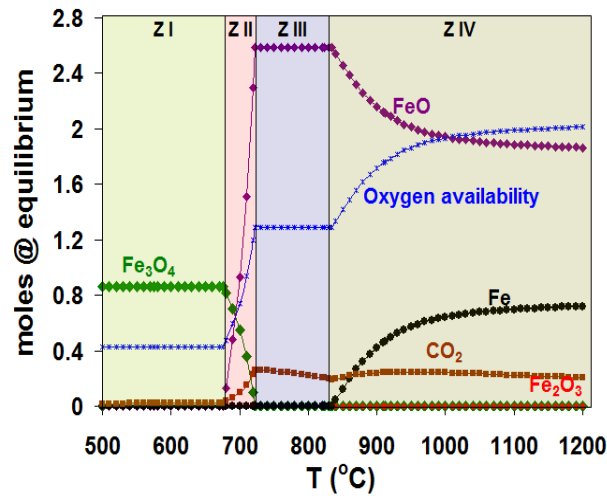


Figure 12. Temperature dependent reduction of Fe_2O_3

It would be interesting to take advantage of this temperature dependent reduction of Fe_2O_3 to tune the partial and complete combustion depending on the process requirement. For this purpose iron should be studied in more detail in kinetic studies.

2.3.4 Effect of sulfur contamination

Effect of 1% H_2S in the natural gas on the carrier performance was analyzed as it was done for syngas. It was found that the equilibrium conversion, selectivity towards complete combustion, selectivity towards hydrogen production and resistance to coking were virtually unaffected by 1% H_2S contamination. However significant sulfide formation was observed for all carriers except Cr as shown in figure 13. The trend is very similar to that observed in case of syngas combustion. One interesting point is that Fe shows no sulfide formation above 1000°C and hence could be a good alternative for efficient but expensive carriers like Cu, Ni and Co when natural gas is used as fuel.

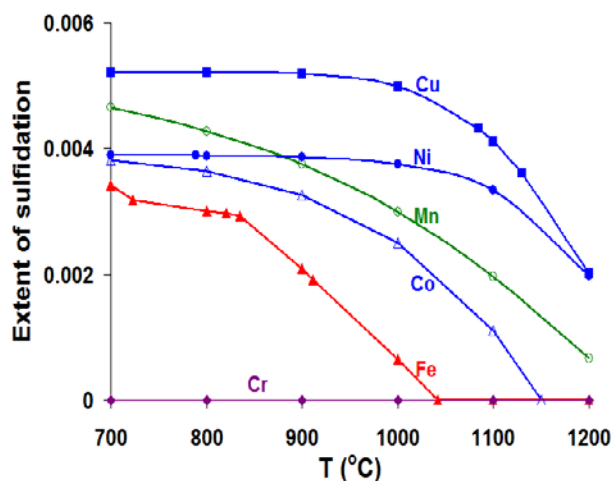


Figure 13. Resistance of Oxygen carriers to sulfide formation during natural gas combustion

2.4 SUMMARY

Thermodynamic analysis discussed in this chapter clearly suggests that there is no “perfect” oxygen carrier for CLC. This analysis only serves as a guideline for choosing an appropriate oxygen carrier depending on the fuel type and the operating temperature. However in real process the reactor configuration, size of the carrier, contact time, heat and mass transfer and other kinetic parameters play very important role and they affect the suitability of a particular carrier for that process. Nevertheless, the thermodynamics gives a rough estimate of what carrier could be feasible and can be taken as a good starting point for thorough kinetic studies.

3.0 NANOCOMPOSITE OXYGEN CARRIERS FOR CHEMICAL LOOPING COMBUSTION OF SULFUR CONTAMINATED SYNTHESIS GAS

Based on the results of thermodynamic evaluation it is evident that no single carrier is perfect and all have their own pros and cons. Hence choice of an oxygen carrier totally depends on the fuel type, operating conditions and process requirements. If the fuel conversion, resistance to coking and selectivity are taken as major comparison criteria then for a sulfur-free fuel Ni and Cu are the obvious choices among the metals. Both give 100% fuel conversion, are highly robust to coking and are highly selective towards complete combustion in the operating temperature range of 700-1200°C. However when exposed to the redox environment of CLC both Ni and Cu (and all other oxygen carriers) suffer from insufficient thermal stability and slow redox kinetics. Cu-, Ni-, Fe-, Mn- and Co-based oxygen carriers have been tested with regard to their thermal stability and redox kinetics [13,16,42]. Typically, these metals are rendered thermally stable by supporting them on appropriate high-temperature supports such as Al₂O₃, SiO₂, or similar oxides [25,52-53]. All these studies have been carried out for a sulfur-free fuel and much less attention has been given to-date to the interaction of sulfur contaminants with oxygen carriers. All fossil - and most renewable - fuels contain significant amounts of sulfur contaminants (mainly in the form of H₂S), which, as seen in thermodynamic analysis (section 2.1.3), can react with metal and metal oxides to form corresponding metal sulfides and can thus impact the performance of carrier materials [16,52,54]. Metal sulfides also often have lower melting points

(refer section 2.1.4) than the corresponding metals or metal oxides, and thus put an additional constraint on the operating temperature of a combustion process. As decreasing fossil fuel reserves are leading to a shift towards increasingly “dirty” fuels, the performance of fossil fuel-based processes and materials in such environments is hence becoming ever more important.

We have previously demonstrated that the embedding of metal nanoparticles into a ceramic matrix (BHA = Barium Hexaaluminate) can result in unusually active and sinter-resistant nanocomposite materials which combine the high reactivity of metals with the high-temperature stability of ceramics [55]. The resulting materials show very fast oxidation and reduction kinetics, and were stable in multiple redox cycles in the temperature range of interest for chemical looping ($\sim 700 - 1000^\circ\text{C}$).

Here, we investigate the effect of H_2S (as the typical main S-contaminant) in a typical coal-derived syngas on the redox kinetics of these nanostructured oxygen carriers. Thermodynamic analysis in previous section shows that Ni and Cu are highly efficient oxygen carriers for syngas combustion. Hence nanocomposite Ni- and Cu-BHA carriers were chosen for the kinetic studies. They were synthesized, characterized before and after exposure to H_2S , and evaluated with regard to their performance in cyclic redox operation, as characteristic for CLC.

3.1 EXPERIMENTAL

3.1.1 Synthesis and characterization

The synthesis of the nanocomposite oxygen carriers is schematically shown in figure 14. It is a sol-gel synthesis approach which is template by a reverse microemulsion template. In this

synthesis, metal nanoparticles are synthesized simultaneously with the high temperature stable ceramic matrix in one pot synthesis. A reverse microemulsion is prepared by mixing aqueous metal salt solution ($\text{Ni}(\text{NO}_3)_3 \cdot 6 \text{H}_2\text{O}$ (99.999%) and $\text{Cu}(\text{NO}_3)_2 \cdot 2.5 \text{H}_2\text{O}$ (99.99%), respectively, for Ni- and Cu-based carriers) with iso-octane (2,2,4-trimethylpentane, 99.7%) and a surfactant (poly(ethylene oxide)-*block*- poly(propylene oxide)-*block*-poly(ethylene oxide), Aldrich). 1-pentanol (99+%) is added as a co-surfactant. Aluminum isopropoxide and barium isopropoxide (both 99.9%) at a stoichiometric ratio of 1 to 12 are dissolved in dry isopropanol before addition to the reverse microemulsion. The isopropoxides diffuse through reverse micelles where they hydrolyse. Simultaneously, the metal salt is reduced to metal nanoparticles, which are embedded between the oxide nanoparticles. The microemulsion is then aged for 48 hours, before separating the water and oil phase by temperature induced phase separation. The product phase is washed several times with acetone and remaining volatile residues are removed by freeze drying. This procedure results in a powdered material which is then calcined in air for 5 hours at 600°C to get the final form of the material.

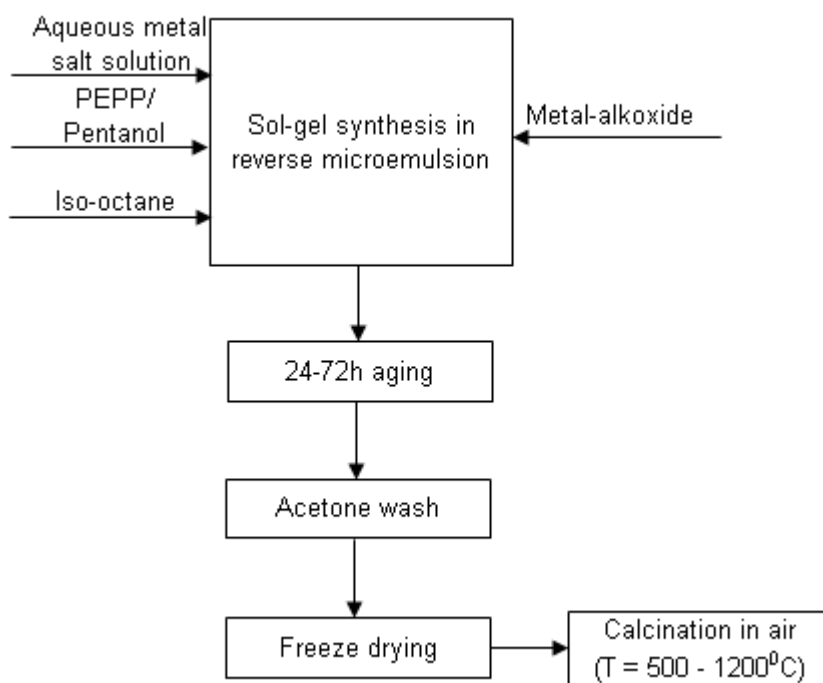


Figure 14. Schematic synthesis of nanocomposite oxygen carriers

The materials were characterized at various stages (after synthesis, exposure to H₂S, and after various reactive tests) via transmission electron microscopy (TEM, JEOL 200), X-ray diffraction (XRD, Phillips PW1830 with typical scans between 15° and 90° (2θ) in steps of 0.08° with a minimum counting time of 0.2 s at each step), and nitrogen porosimetry (Micromeritics ASAP 2020). A typical TEM image is shown in figure 15, where the highly homogeneous nanostructure of the material consisting of Ni nanoparticles (black) and the BHA matrix (grey background) can be observed.

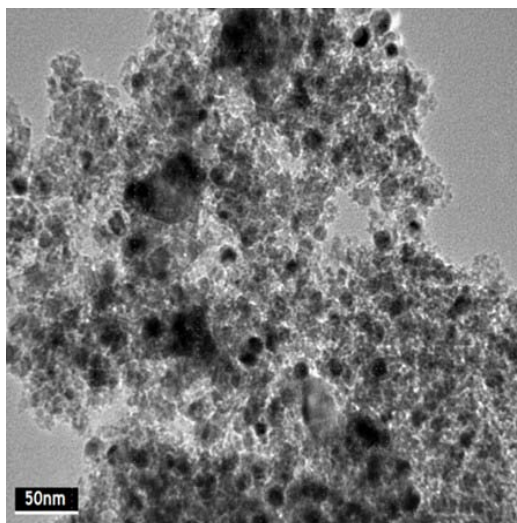


Figure 15. TEM image of a typical nanocomposite Ni-BHA (37wt% Ni).

3.1.2 Reactive tests

Kinetics and stability of the carriers were evaluated in cyclic thermogravimetric (TGA) experiments, using a Perkin Elmers TGA-7 thermogravimetric analyzer. In a typical run, between 20 and 40 mg of the nanocomposite carriers were heated inside the TGA cradle in an inert gas stream (N_2 , purity 4.0) to the desired reaction temperature. Then, a dry syngas mixture with or without H_2S contamination (see table 4 for detailed compositions of syngas) and air (purity: 0.1) were flown alternately at a flow rate of 60 sccm (standard cubic centimeters per minute) in order to simulate the periodic oxidation-reduction cycles of CLC. Between oxidation and reduction phases, the TGA was purged with nitrogen (flow rate 60 sccm) in order to avoid potentially flammable gas mixtures inside the instrument. The duration of the oxidation, reduction, and purge phases in a typical experiment were 10 - 15 min, 15 min, and 7 min, respectively. All experiments were conducted at ambient pressure conditions.

Table 4. Composition of syngas used for TGA tests

Syngas w/o sulfur		Syngas w/ sulfur	
Constituent	Moles (%)	Constituent	Moles (%)
H ₂	27	H ₂	27
CO	36	CO	36
CO ₂	12	CO ₂	12
He	25	He	24
H ₂ S	0	H ₂ S	1

3.2 RESULTS AND DISCUSSION

3.2.1 Structural stability

In order to test the structural stability of the above described nanocomposite carriers in a sulfur-containing atmosphere, Ni-BHA was first oxidized in air at 800⁰C for 30 minutes, and the oxidized powder sample was then exposed to 10,000 ppm H₂S in Argon in a calcinations over at various temperatures for 30 min. each. After this exposure, the sample composition was evaluated using X-ray diffraction. Figure 16 shows the results obtained after exposure at 300⁰C, 500⁰C, 700⁰C and 800⁰C.

After exposure at 300°C, the sample shows only weak reflexes representing NiO and the ceramic matrix (consisting of a largely amorphous and hence poorly resolved mix of BaO and Al₂O₃ as precursor of the high-temperature BHA phase). This temperature is too low to result in significant reaction between H₂S and NiO. Only after exposure at 500°C first weak reflexes for nickel sulfide indicate the onset of sulfidation. As expected, the degree of sulfidation then increases with increasing temperature, and the sample appears fully sulfidized at 800 °C. Interestingly, strong BaSO₄ reflexes at temperatures above 700°C indicate that at sufficiently high temperature the Ba-content of the support is becoming sulfidized as well. Most importantly, we do not find evidence for the formation of Ni₃S₂ under any conditions. This sulfide has a very low melting point ($T_m \sim 789^\circ\text{C}$) and could hence lead to unstable operation of the carrier due to plugging of pores and agglomeration of particles.

The NiO-BHA sample sulfidized at 800°C (i.e. the sample with the highest degree of sulfidation) was then re-oxidized in air at 800°C for 30 minutes. XRD analysis of the resulting sample shows complete conversion of NiS to NiO, while retaining unchanged BaSO₄ reflexes (figure 17). Overall, this indicates that the nanocomposite Ni-BHA carriers are fully sulfidized during exposure to H₂S at sufficiently high temperature, but that this sulfidation is completely reversible upon re-oxidation.

However, the irreversible formation of BaSO₄ raised concerns about the structural stability. Therefore, the morphology of the carriers before and after exposure to H₂S, as well as after re-oxidation, was evaluated via nitrogen sorption. Figure 18 shows a BET pore analysis of a sample before sulfidation, after sulfidation, and after re-oxidation at 800°C. One can see that upon sulfidation the pore volume drops slightly but the pore size distribution remains essentially

unchanged. Once the sample is re-oxidized, it quantitatively recovers the pore volume within experimental error.

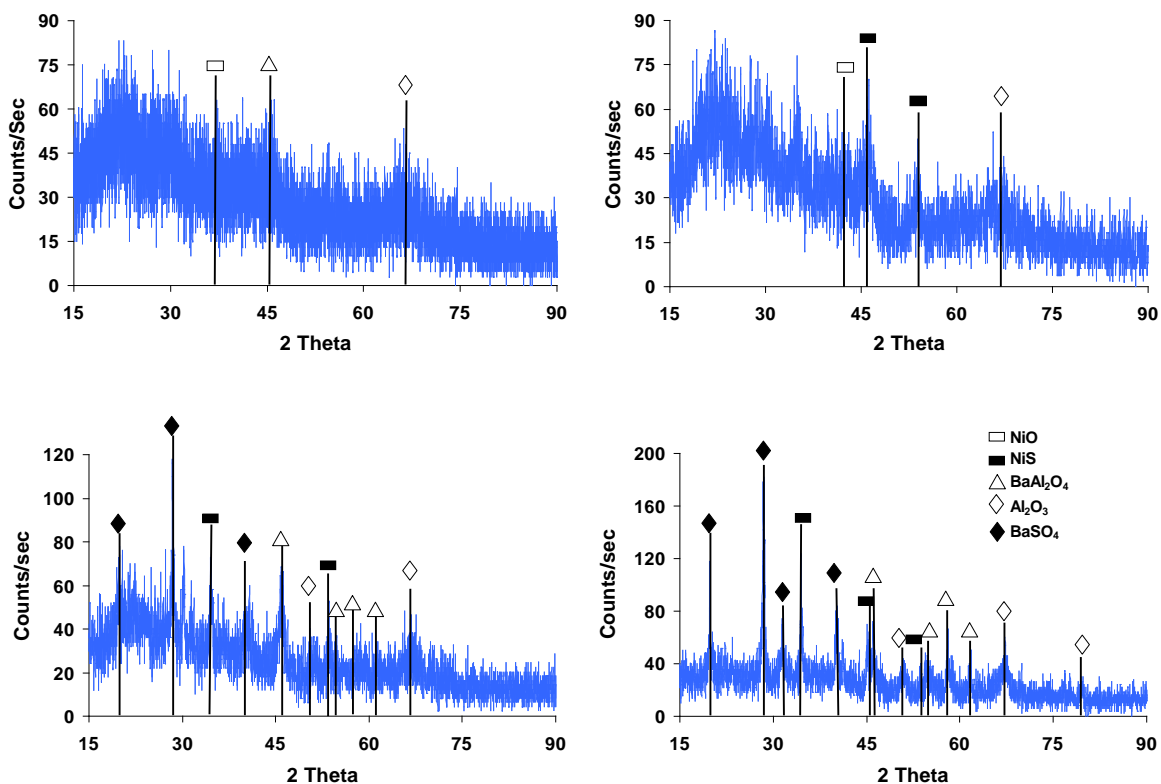


Figure 16. XRD patterns of NiO-BHA after 30 min. exposure to 10,000 ppm H₂S in Ar at 300⁰C (top left), 500⁰C (top right), 700⁰C (bottom left) and 800⁰C (bottom right)

The drop in pore volume can hence be attributed to the larger volume of NiS (i.e. fully sulfidized NiO particles) embedded in the ceramic pore structure. Since the NiS particles are fully re-oxidized to NiO, this effect is completely reversible. Sulfidation of the Ba content in the sample, on the other hand, has apparently a negligible effect on the pore size distribution, presumably due to the low total Ba content of the samples. Most importantly, it does not affect any irreversible changes in pore morphology and hence has no measurable impact on carrier stability.

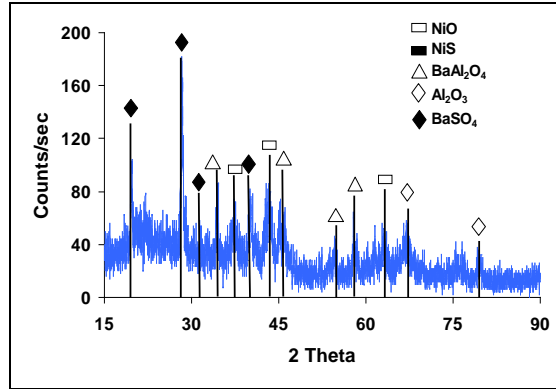


Figure 17. XRD pattern of NiO-BHA after exposure to 10,000 ppm H₂S in argon for 30 min (see also figure 16, bottom right graph) and re-oxidization in air at 800°C

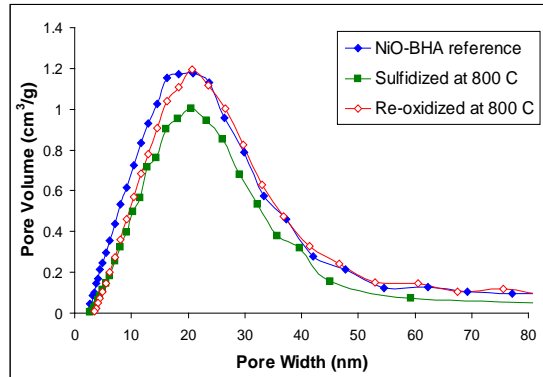


Figure 18. BET pore analysis of NiO-BHA before, after sulfidation and after re-oxidation at 800°C.

3.2.2 Ni-BHA

Once the structural stability of Ni-BHA upon exposure to H₂S was verified, the nanostructured carrier were subjected to cyclic-TGA (thermogravimetric analysis) tests with H₂S-contaminated syngas in order to evaluate the effect of H₂S on redox kinetics. During the experiments, Ni-BHA carriers were oxidized in air for 10 min, and then reduced in a sulfur-free and a sulfur-containing dry syngas for 15 min. The composition of both syngas streams is identical except for the H₂S content and the adjusted He balance (see table 4 above). Both oxidation and reduction were

conducted at 900°C and 1 bar. The H₂S concentration (1% = 10,000 ppm) represents the upper limit of sulfur concentrations typically found in coal-fuel derived syngas and is used as a stringent test for the performance of the carriers in an H₂S-containing atmosphere.

In order to establish a base line for the carrier performance, the cyclic TGA experiments were first run with sulfur-free syngas, followed with multiple cycles in H₂S containing syngas. After that, the fuel stream was switched back to sulfur-free syngas to test for any irreversible changes in the kinetic behavior during exposure to the sulfur-containing syngas. Results are shown in figure 19.

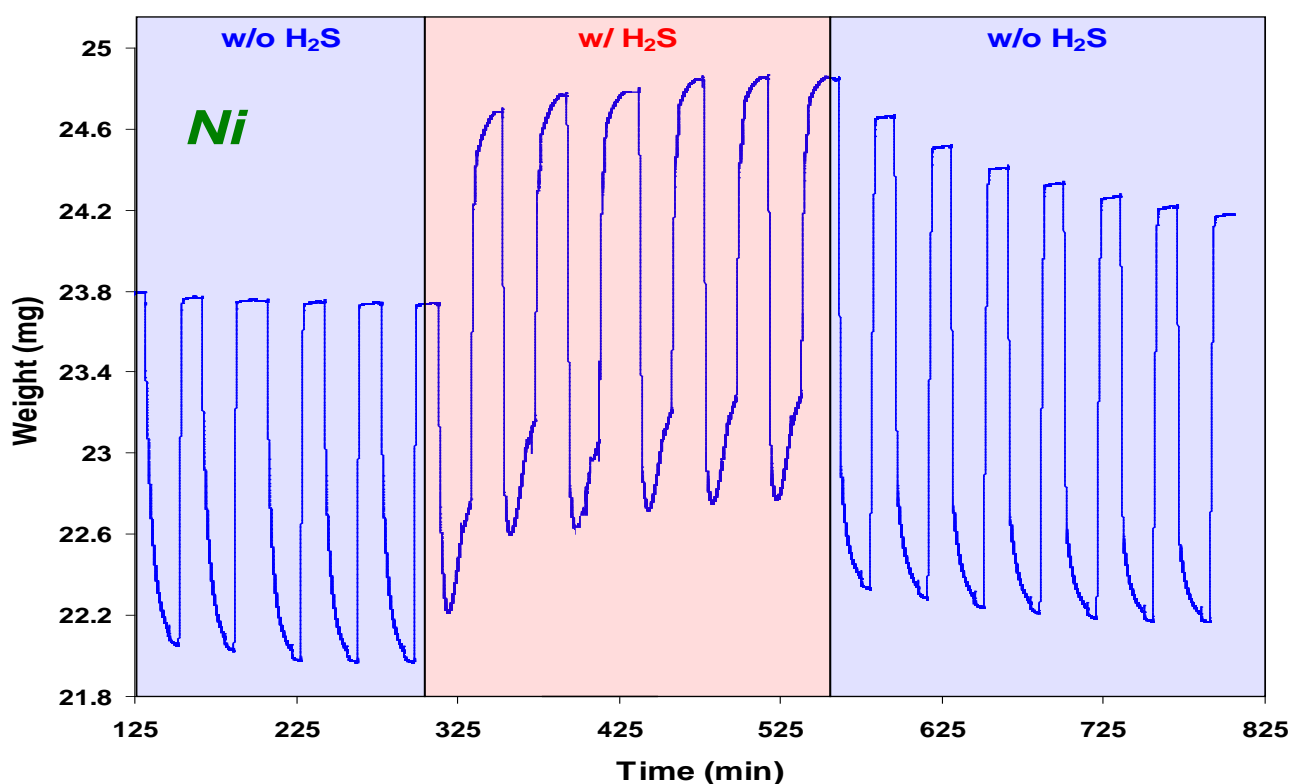


Figure 19. Sample weight versus time for Ni-BHA during cyclic TGA redox experiments at 900°C with sulfur-free syngas (t=125-300 min), followed by sulfur-contaminated syngas (t=300 – 500min), and again by sulfur-free syngas (t>550 min, as indicated by the shadings)

One can see the periodic oxidation and reduction of the sample as reflected in the weight changes: The upper limit of the weight curve represents the fully oxidized sample, while the

lower limit represents the fully reduced sample. Clearly, oxidation of the sample during the first, sulfur-free, phase is very fast with almost instantaneous weight changes, while reduction is slightly slower. This agrees well with our previous studies of these carriers. Upon switching to S-contaminated syngas streams, the total weight curve is shifted towards higher values reflecting the increased sample weight due to sulfidation, as discussed above. This weight shift stabilizes already after only ~2 cycles. The cycle seems otherwise largely unaffected by the sulfur exposure, although reduction appears somewhat accelerated and oxidation slightly slowed down. When the reducing gas is switched back to sulfur-free syngas, the sample loses the added weight again and slowly falls back to the initial weight levels by sulfur oxidation. This process reflects the loss of sulfur from the sample, including the loss of sulfur from BaSO_4 , once the sample is exposed to a sulfur-free atmosphere. Since the sulfate cannot be removed during the oxidation phase, as shown above, this indicates sulfate decomposition during the reduction phase with sulfur-free syngas. Due to the low conversions in the TGA experiment, it was not possible to detect product gases with sufficient sensitivity, but it seems likely that the decomposition proceeds via two consecutive steps: First, the sulfate is reduced to the sulfide through oxidation of CO and H_2 in the syngas, and then the sulfide is further reduced via formation of H_2S . This explanation is confirmed by thermodynamic calculations as explained in previous section 2.2.2. In contrast to the sulfur uptake upon exposure to sulfur-containing syngas, the sulfur loss during re-exposure to sulfur-free syngas is relatively slow. Nevertheless, the fact that the initial weight levels are eventually recovered further supports the above observation that the carrier morphology and hence also its redox kinetics are stable during sulfur exposure.

In order to allow for a more direct comparison of the redox kinetics before, during, and after H_2S exposure, figure 20 shows single redox cycles from the three phases of the above

discussed cyclic TGA experiment (in each case the final cycle from the respective phase is shown). The y-axis has been normalized by plotting conversion versus time, where conversion is defined as the fractional conversion of the oxidized carrier as derived from the observed sample weight, i.e.: $X_w = (W - W_{\min}) / (W_{\max} - W_{\min})$, where X_w denotes the (fractional) carrier conversion, W is the (momentary) sample weight, W_{\min} the minimum (i.e. fully reduced) sample weight, and W_{\max} the maximum (fully oxidized) sample weight. $X_w = 1$ hence represents a completely oxidized carrier, while $X_w = 0$ corresponds to a fully reduced sample.

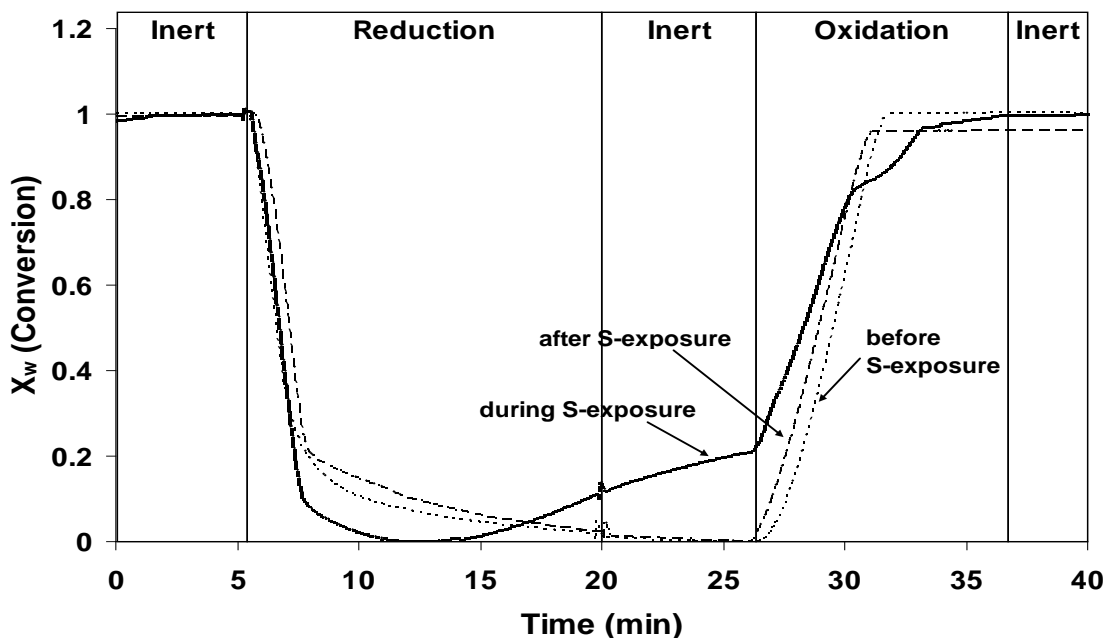


Figure 20. Effect of H_2S on redox kinetics of Ni-BHA: Conversion during a single redox cycle before (dotted line), during (solid line), and after sulfur exposure (dashed line; $T = 900^\circ C$)

One can see that very high initial rate of reaction during the reduction phase is unaffected by the sulfur exposure, i.e. the slope of the weight trace is identical between the three curves. Interestingly, however, the sulfur-containing syngas results in a deeper reduction of the sample, suggesting that H_2S is undergoing fast oxidation (via formation of water and SO_2), and hence accelerating reduction. Furthermore, the sample conversion goes through a minimum for the

sample exposed to the H_2S -containing atmosphere, suggesting that the sample is starting to take up sulfur in the later stages of the reduction cycle, i.e. once the sample is sufficiently oxygen-depleted, the mechanism appears to change from the full oxidation of H_2S to water and SO_2 to the reduction of H_2S to hydrogen and metal sulfide.

The (apparent) increase in conversion due to sulfur uptake continues well into the purge phase. This is a result of the build-up of sulfur residues on the (cold) outer walls of the TGA flow tube, which leads to a low, but continued, exposure of the sample to sulfur during the purge phase. It was unfortunately not possible to suppress this sulfur formation entirely in our experimental set-up. However, since the residue burnt off quickly during the oxidation phase and further accumulation was hence avoided, the experimental results are not significantly affected by this background exposure.

Finally, in the oxidation phase, one observes no significant difference in the oxidation kinetics before and after exposure to H_2S . However, the oxidation during the cyclic experiments with H_2S -containing syngas shows two distinct oxidation stages, a fast initial phase with a rate comparable to the oxidation rate before and after sulfur exposure, followed by a significantly slower oxidation phase (at $t \sim 30$ min) which then appears to accelerate again.

Comparison with the oxidation traces during the cyclic TGA experiments with S-free syngas, allows identification of the process responsible for the slow second oxidation process. Generally, three different oxidation reactions occur during oxidation of the sulfidized sample: Oxidation of the metallic Ni nanoparticles to NiO, conversion of NiS to NiO, and oxidation of BaS to BaSO_4 . Since the slow-down in the oxidation phase is absent in the sample before sulfur-exposure, it cannot result from the oxidation of the metallic Ni nanoparticles. Similarly, the S-free experiment after exposure to H_2S , does not show the slow-down despite the fact that a

significant amount of BaS is still present during the first few cycles after switching back to sulfur-free syngas. Hence, the oxidation of BaS also cannot be responsible for the slow oxidation step. Therefore, the oxidation of NiS to NiO must be responsible for the apparent slow-down of the oxidation. Since the conversion of NiS to NiO results in a weight *loss*, i.e. it counters the general weight increase during sample oxidation, this results in the observed flattening of the weight curve. Hence, the oxidation trace indicates that the conversion of NiS is delayed in comparison to the other oxidation reactions, but the increase in the slope towards the very end of the oxidation phase also shows that NiS conversion is complete before the other components have been fully oxidized.

The latter observation is significant for CLC operation. Conventional (i.e. not nanostructured) carriers typically show significant slow-down of the oxidation rate with increasing degree of oxidation due to increasing diffusion resistance through the growing oxide layer on the metal particle. It has been suggested that this slow-down can be circumvented by utilizing only the redox potential of the outer layers of the carriers, i.e. the initial oxidation/reduction phase, and hence minimizing diffusion limitations at the expense of reduced oxygen carrying capacity. As the present results indicate, this could lead to incomplete recovery of sulfides in sulfur-contaminated fuel streams, resulting in accumulation of sulfides and ultimately in shut-down of the CLC process.

3.2.3 Cu-BHA

In addition to Ni-BHA, nanocomposite Cu-BHA samples were subjected to the same analysis as described above. Cu is frequently discussed as an alternate metal for oxygen carrying in chemical looping, and we had previously already studied the redox kinetics of nanocomposite

Cu-carriers in comparison to conventionally prepared carriers during CLC of clean (i.e. sulfur free) syngas [56].

The Cu-based carriers showed qualitatively the same phenomena as discussed above for Ni-BHA, and we will hence only briefly discuss some main results. Figure 21 shows again the results of TGA experiments during cyclic reduction and oxidation in sulfur-free syngas ($t < 190$ min), syngas with 1% H_2S ($190 \text{ min} < t < 490 \text{ min}$), and again with sulfur-free syngas. All experimental conditions were identical to the respective Ni-BHA experiments.

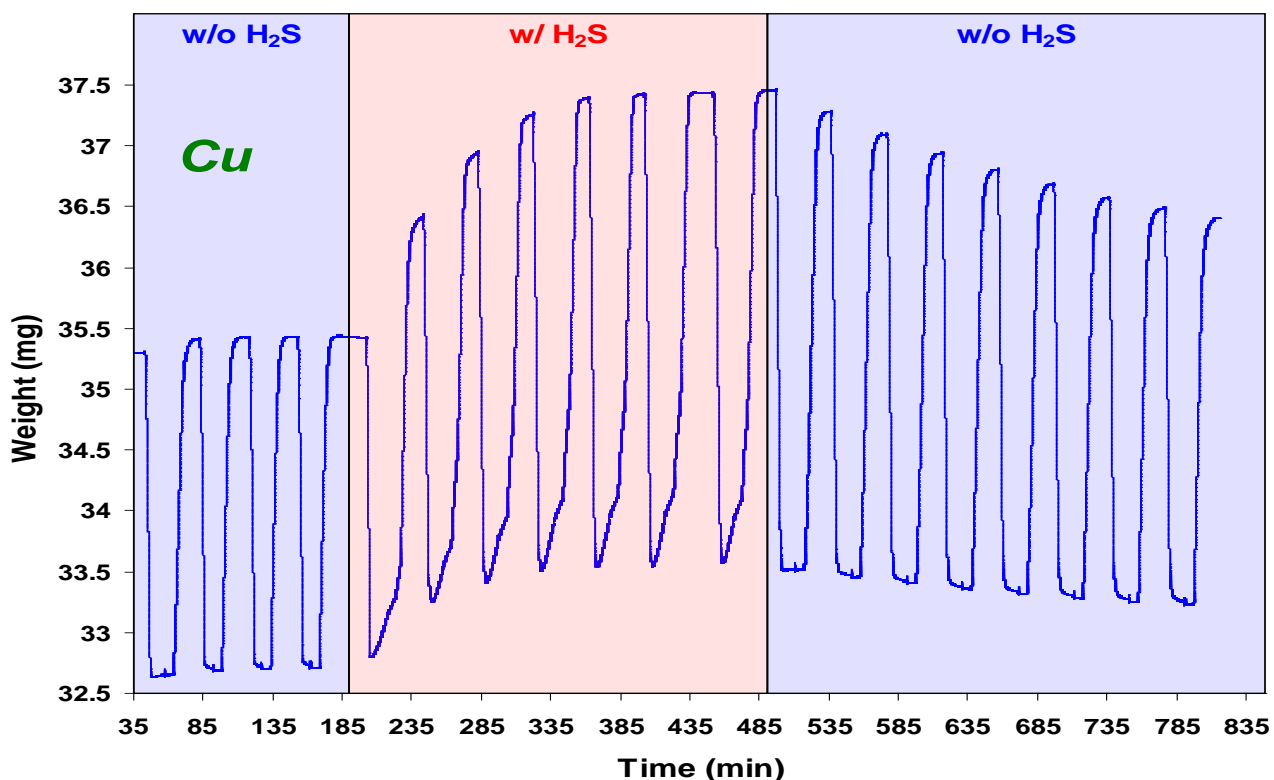


Figure 21. Sample weight versus time for Cu-BHA during cyclic TGA redox experiments at 900oC with sulfur-free syngas ($t=35$ -190 min), followed by sulfur-contaminated syngas ($t=190 - 490$ min), and again by sulfur-free syngas ($t > 490$ min, as indicated by the shadings)

Overall, one observes the same trends as above described for Ni-BHA: Very fast oxidation-reduction kinetics during the initial, sulfur-free cycles, a strong increase in sample weight during sulfur exposure, and a slow drop of the sample weight after switching back to

sulfur-free syngas. The only significant difference between the Cu- and the Ni-experiments is the rate of sample weight increase during exposure to H₂S-contaminated syngas. While the Ni-sample weight had stabilized after about 3 cycles (compare figure 19), the Cu-sample shows a stable sample weight only after ~5 cycles, suggesting a slower or more extensive sulfur uptake. Comparing the increase between the weight maxima before and during S-exposure for Cu and Ni samples, we find an increase of ~ 4% for Ni samples vs ~6% for Cu samples, i.e. sulfur uptake is increased for Cu-based samples. This is in qualitative agreement with our thermodynamic evaluation of oxygen carrier materials, which shows that Cu is significantly more prone to sulfide formation (see section 4.1)

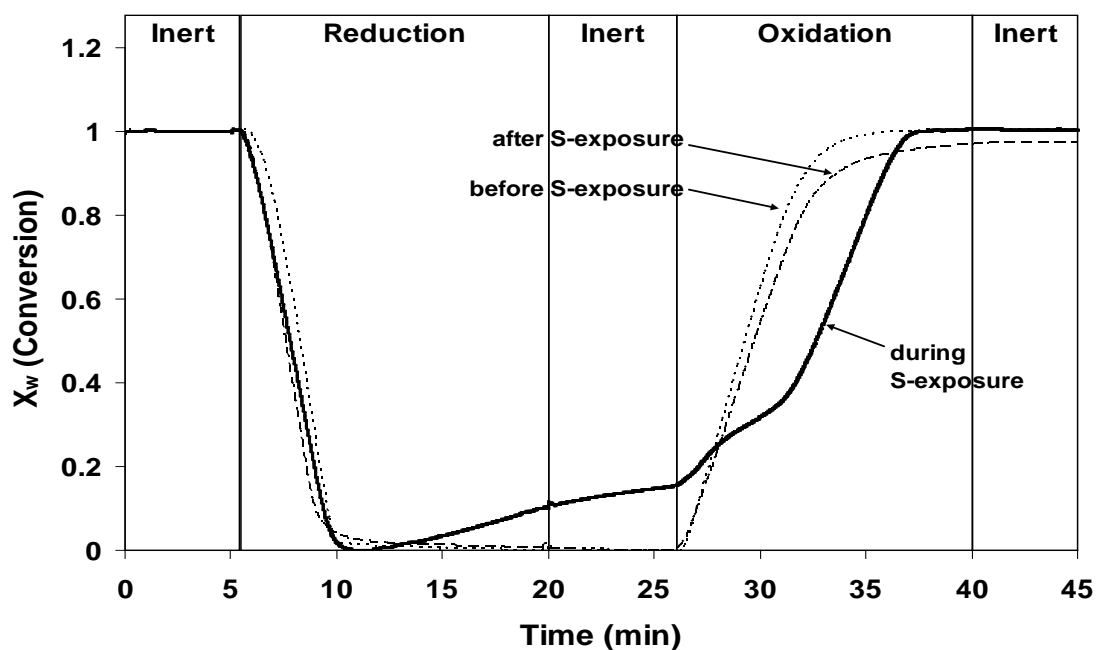


Figure 22. Effect of H₂S on redox kinetics of Cu-BHA: Conversion during a single redox cycle before (dotted line), during (solid line), and after sulfur exposure (dashed line; T= 900°C)

In order to facilitate a direct comparison of the redox kinetics before, during, and after sulfur exposure, we calculated again conversion versus time. Figure 22 shows again single redox cycles in direct comparison between pre-sulfur exposure, during sulfur exposure, and post-sulfur

exposure cycles. As for Ni, we find that the reduction kinetics is essentially unaffected by the exposure to sulfur, with the exception of the strong sulfur uptake evidenced by the even more pronounced sample weight increase in the later stage of the reduction (resulting in an apparent increase in conversion). Furthermore, the fast, deep reduction observed for Ni-BHA is absent. This could be caused by the more pronounced, faster sulfur uptake which would mask the reduction by counter-acting the weight loss associated with the reduction.

During the oxidation, the time traces before and after exposure to sulfur are again virtually indistinguishable (the slightly lower degree of oxidation after sulfur exposure indicates that the sulfur loss is not complete yet), and the oxidation trace during sulfur exposure once again shows two distinct oxidation regimes. However, in comparison to Ni-BHA, the Cu samples show the above discussed slow-down in the oxidation kinetics due to the conversion of the sulfide to the oxide at a much early point in the re-oxidation ($X \sim 0.3-0.4$, versus $X \sim 0.8-0.9$ for Ni). In fact, the oxidation rate is clearly slowed down in comparison to the experiments with S-free syngas even before the pronounced plateau, indicating that Cu sulfide conversion sets on immediately upon starting the oxidation phase. After the plateau, the rate of oxidation (i.e. the slope of the line) becomes virtually identical to the rate of oxidation during the sulfur-free redox cycles indicating unchanged re-oxidation kinetics of the remaining Cu-BHA sample.

This observation suggests that CuS is preferentially reacting with oxygen, unlike Ni, where the sulfide appeared delayed in the oxidation kinetics. Hence, the above discussed problems with incomplete redox cycles should be of lesser concern for Cu-based carriers.

3.2.4 Material balance calculations

The sequence of the experiments discussed above allows for a straight-forward evaluation of the extent of sulfidation of the metal and the Ba in the carrier matrix. The basis for the calculations is shown schematically in figure 23.

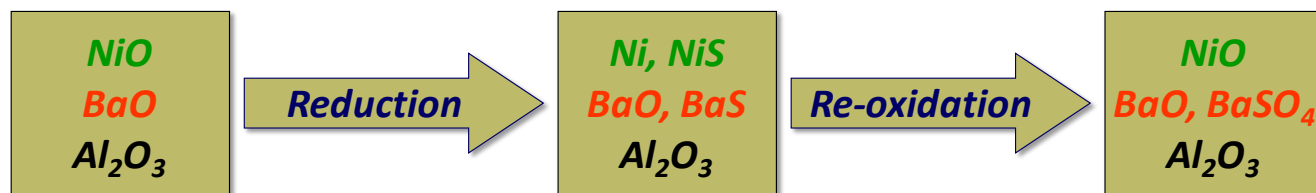


Figure 23. Schematic for material balance calculations

The weight change during the initial, sulfur-free redox cycles allows for precise determination of the metal weight loading of the sample. Upon reduction with S-contaminated syngas, NiO is completely converted to Ni and NiS, whereas BaO is sulfidized to BaS. BaO can not be reduced to metallic barium under the given reducing atmosphere and alumina remains unaffected throughout the oxidation-reduction cycles. Upon re-oxidation Ni and NiS are quantitatively converted to NiO, and BaS is completely oxidized to BaSO₄. All these considerations are supported by the XRD analysis shown in figures 16 and 17.

Based on these considerations and the known total weight after reduction and after re-oxidation, the material balances for the reduction and oxidation processes yield two equations with two unknowns, namely the extent of sulfidation of Ni and Barium, respectively, which can hence easily be calculated. Results of this analysis are shown in figure 24, where the extent of sulfidation (defined as the fractional conversion of metal to metal sulfide) is shown versus cycle number for Ni-BHA (left) and Cu-BHA carriers (right).

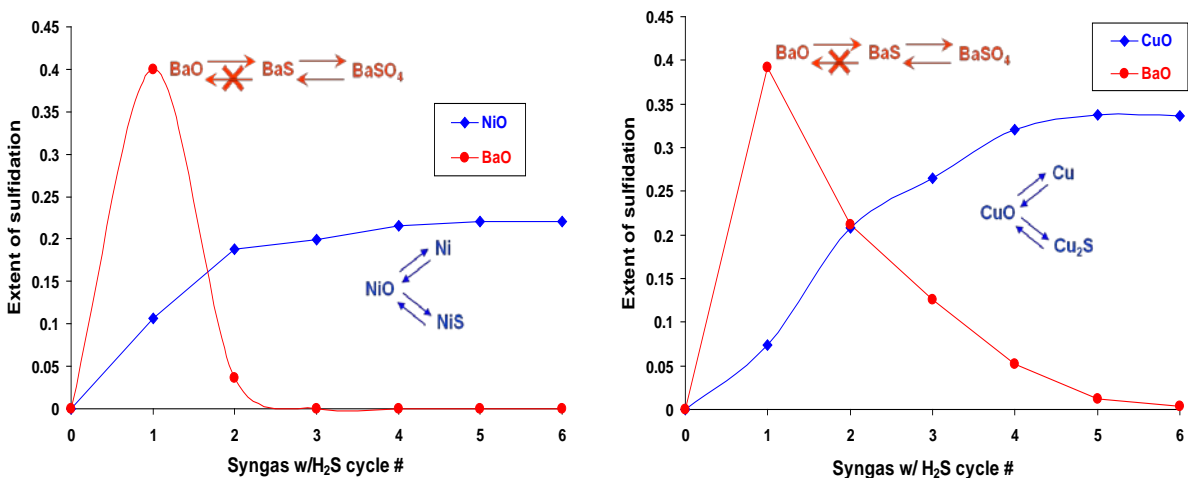


Figure 24. Extent of sulfidation per cycle: Ni-BHA (left) and Cu-BHA (right)

For both carriers, BaO is preferentially oxidized in the first cycle, resulting in a partial initial “shielding” of the metal particles. This effect is much more pronounced for Cu, where it extends over the first three cycles. Clearly, BaO is more prone to sulfidation than either metal. The irreversibility of the BaS formation is reflected in the fact that the extent of sulfidation drops to zero after the first two cycles for Ni, and after 6 cycles for Cu. In contrast to that, NiS and Cu₂S can be recovered as the respective oxides in subsequent re-oxidation cycle and the extent of sulfidation per cycle reaches a constant level as soon as the BaO is saturated.

3.2.5 Effect of BaSO₄ on oxygen carrying capacity

The significant degree of sulfidation of BaO in both samples, and the irreversibility of this conversion during cyclic redox operation with S-contaminated syngas, suggest that the BaS formed in this process actually participates in the oxidation-reduction cycles and hence should contribute to the oxygen carrying capacity of the carriers. We hence calculated the oxygen carrying capacity for Ni-BHA and Cu-BHA as a function of redox cycle after switching to S-

contaminated syngas. Results are shown in figure 25, where the oxygen carrying capacity is defined as the mass of oxygen in the fully oxidized sample divided by the mass of the initial, fully reduced sample.

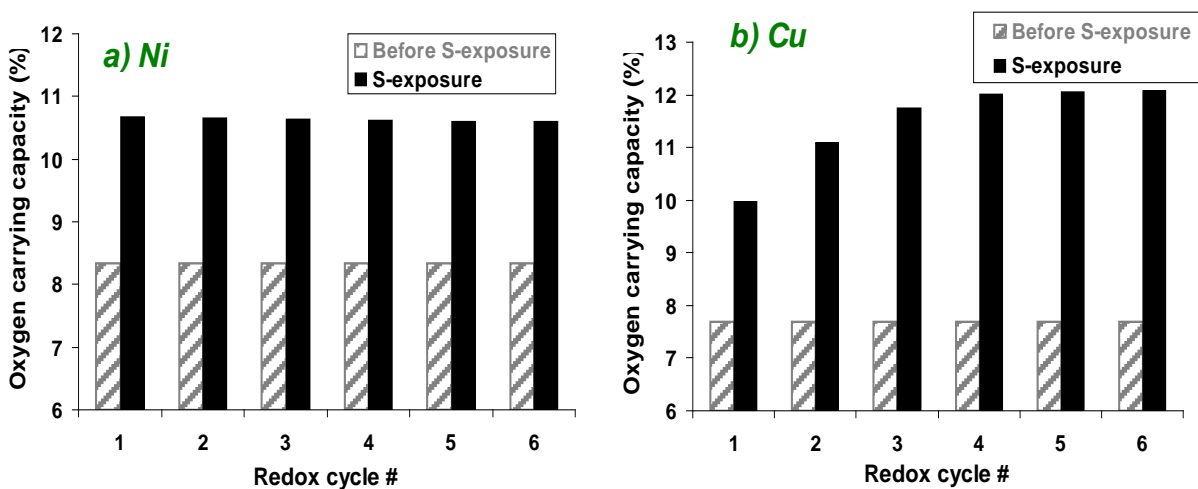


Figure 25. Effect of H₂S on oxygen carrying capacity (as percentage of total reduced carrier weight) in subsequent redox cycles with S-contaminated syngas for Ni-BHA (left) and Cu-BHA (right)

One can see that in both cases the oxygen carrying capacity increases significantly upon exposure to H₂S. While this increase is instantaneous for Ni-BHA – in agreement with the virtually complete BaS formation in the first cycle (see figure 24) - the increase for Cu-BHA reaches its final value only after ~5 cycles. Also, while the increase in oxygen carrying capacity for Ni-BHA is significant with about a 27% increase, the increase is even more drastic for Cu-BHA with a ~57% increase in oxygen carrying capacity!

Overall, the exposure to S-contaminated syngas hence resulted in only minor changes in the redox kinetics, but surprisingly strong increases in oxygen carrying capacity. The metal sulfide-sulfate cycle has been proposed previously as a potentially quite efficient alternative to the basic metal/metal oxide cycle for chemical looping[43-44]. In the present work, exposure to S-contaminated syngas resulted in the formation of sulfide/metal hybrid carriers, where the

support matrix does not only avoid sintering of the metal component, but also contributes significantly to the oxygen carrying capacity. It seems interesting to consider the targeted synthesis of such hybrid carriers as highly stable, high capacity carrier configurations.

3.3 SUMMARY

Chemical looping combustion is a promising technology for the clean combustion of fossil and renewable fuels with inherent air separation and CO₂ capture. We have previously shown that nanocomposites have a great potential for this application due to fast redox kinetics and very good thermal stability compared to conventional carriers. In this chapter, we demonstrated that the stability of nanostructured Ni-BHA and Cu-BHA is not affected by the presence of H₂S even in concentrations as high as 10,000 ppm over a broad range of temperatures.

The redox kinetics is only mildly affected by the presence of H₂S in synthesis gas, although care must be taken to assure complete re-oxidation of the carriers in order to avoid accumulation of sulfides which could result in shut-down of the reactor operation.

The formation of metal sulfides is completely reversible for Cu and Ni upon re-oxidation. In contrast to that, we find irreversible sulfidation of a fraction of the BaO in the support matrix. However, this does not appear to affect the carrier stability, and even results in the emergence of BaS \rightleftharpoons BaSO₄ cycles with a correspondingly strong increase in oxygen carrying capacity by as much as 57%. Overall, the present study hence confirmed the stability and robustness of nanocomposite oxygen carriers and their potential for use in chemical looping combustion of high-sulfur fuels.

4.0 INTEGRATING DESULFURIZATION WITH CO₂ CAPTURE IN CHEMICAL LOOPING COMBUSTION

Motivated by the stable and robust operation observed before, the aim of this study was investigation of the sulfur-capturing capability of these carriers in a CLC process in order to evaluate the potential of utilizing these highly robust nanocomposite oxygen carriers for simultaneous in-situ desulfurization and CO₂ capture.

Figure 26 schematically illustrates the concept of sulfur-capture in CLC process: In the reducer, sulfur present in the fuel (here: synthesis gas with S-contaminants in the form of H₂S and COS) is captured by the metal in the oxygen carrier as metal sulfide. In oxidizer, this metal sulfide is then recovered as metal oxide via oxidation with air, while the sulfur captured from the fuel stream in the reducer is released as SO₂. Overall, such a scheme would hence allow simultaneous capture of CO₂ and SO₂ in separate effluent streams and thus eliminate the need for desulfurization of the fuel, or, for sulfur-containing fuels, avoid formation of corrosive acids downstream of the fuel reactor and eliminate the need for downstream separation of sulfur species from CO₂ before sequestration.

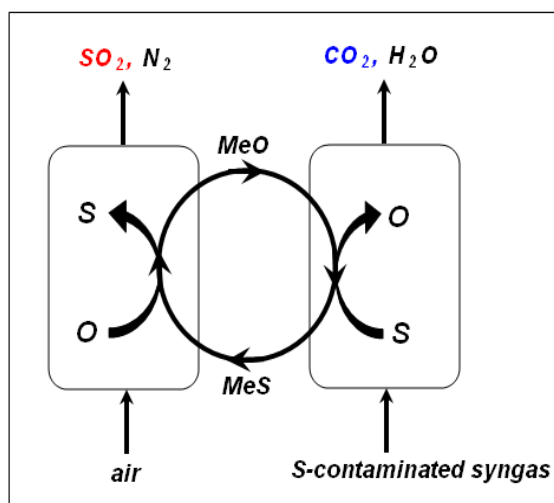


Figure 26. Schematic representation of a CLC process scheme with integrated sulfur capture

Conceptually, simultaneous desulfurization and CO₂-capture is a simple process in CLC. The main challenge, however, is maintaining thermal stability and fast redox kinetics of the oxygen carrier while achieving deep desulfurization of the fuel reactor effluent. We have previously demonstrated that the embedding of metal nanoparticles into a ceramic matrix (here: BHA = Barium-Hexaaluminate) can result in unusually active and sinter-resistant nanocomposite materials which combine the high reactivity of metals with the high-temperature stability of ceramics [55,57-58]. Ni- and Cu-BHA carriers showed very fast oxidation and reduction kinetics, and, most significantly in the present context, showed stable operation in CLC of sulfur-free as well as sulfur-laden syngas [59]. Interestingly, both carriers showed a strong increase in oxygen-carrying capacity when contacted with sulfur-laden syngas, which could be traced back to partial sulfidation of the support.

4.1 CHOICE OF THE CARRIER

In order to select a suitable oxygen carrier for the proposed desulfurization scheme, a thermodynamic analysis of a wide range of metals was carried out using a commercial software package FACTSAGE 5.0, which is based on Gibb's free energy minimization to calculate the equilibrium composition of the gas-solid mixtures. Stoichiometric amounts of different metal oxides and syngas were used in the calculation. The composition of sulfur contaminated syngas is as shown in table 4. As initial reference point, operating conditions of 900°C and 30 atm were used. The equilibrium amount of sulfur species in the reducer exhaust is shown in figure 27(left) for a select range of carriers (most carriers were discarded due to poor redox properties, lack of sulfur capturing ability, cost, or toxicity considerations). The graph shows that Ni and Cu stand out with regard to their sulfur capturing capabilities: both carriers are capable of significantly reducing the sulfur content in the gas phase at equilibrium approximately by three orders of magnitude (note the logarithmic scale on the y-axis!). Among Cu and Ni, Cu is capable of reducing the sulfur contamination from ~10000ppm to <10ppm, and hence Cu is selected as the most promising candidate for the desulfurization scheme.

Since temperature is expected to have a significant impact on sulfur capturing, the effect of operating temperature on the residual sulfur concentration at equilibrium for stoichiometric Cu/syngas mixture was investigated as well. Results are shown in figure 27 (right graph). As expected, the amount of sulfur species present in gas phase increases with increasing temperature, particularly at $T > 900^{\circ}\text{C}$, i.e. the capacity of Cu for sulfur capturing decreases. However, this does not impose a severe limitation, since metallic Cu has a melting point of 1,085°C, and operation of Cu carriers at temperatures in excess of 900°C would likely result in stability issues at extended operation anyway. Combining this upper temperature limit with the

typical operating temperature ranges discussed for CLC processes of $\sim 600\text{--}1200^\circ\text{C}$, a temperature window of $600\text{--}900^\circ\text{C}$ was used for the experimental kinetic evaluation of Cu-based oxygen carriers.

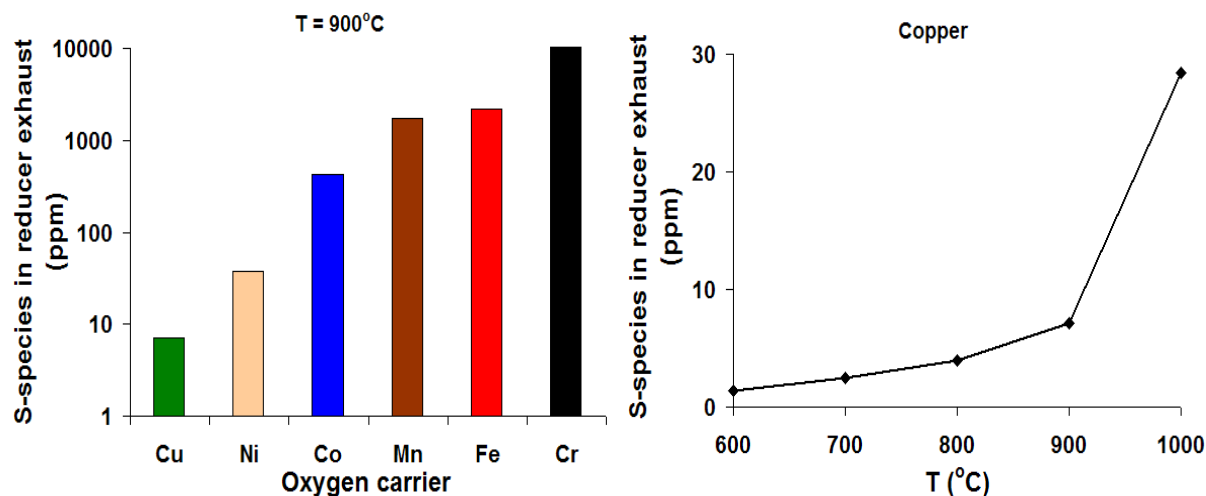


Figure 27. Equilibrium amount of sulfur species in the reducer exhaust at 900°C , 30 atm for select oxygen carriers (left); and the equilibrium amount of sulfur species for Cu as function of temperature ($T = 600\text{--}1000^\circ\text{C}$, $P = 30$ atm; right graph)

4.2 EXPERIMENTAL

4.2.1 Synthesis and characterization

Cu-BHA was synthesized by the same technique as described in section 3.1.1. It was characterized after synthesis and after several reactive tests via transmission electron microscopy (TEM, JEOL 200), X-ray diffraction (XRD, Phillips PW1830 with typical scans between 15° and 90° (2θ) in steps of 0.08° with a minimum counting time of 0.2 s at each step), and nitrogen porosimetry (Micromeritics ASAP 2020).

A typical TEM image is shown in figure 28, which shows the homogeneous nanostructure of the material consisting of Cu nanoparticles (black) and the BHA matrix (grey background).

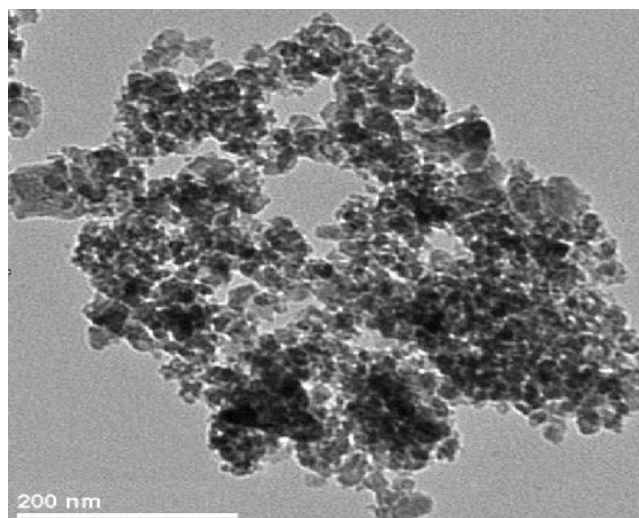


Figure 28. TEM image of a typical nanocomposite Cu-BHA (40wt% Cu)

Compositional analysis with energy-dispersive X-ray (EDX) after synthesis and calcination gave a typical composition of about 30 wt % (15 mol %) Cu, 29 wt % (32 mol %) Al, 14 wt % (3 mol %) Ba, and 27 wt % (50 mol %) O. In these materials, Ba fulfills an important role as stabilizer for the alumina matrix [60-61]. Due to the low Ba content of only 3 mol %, the cost of Ba should not affect the overall cost of the materials significantly. However, while no data on the toxicity of BHA appears to be available at this point, the known toxicity of barium aluminate ($3\text{BaO} \cdot \text{Al}_2\text{O}_3$) suggests that appropriate care should be taken in handling this material on an industrial scale.

Figure 29 (left) shows nitrogen adsorption isotherm for a typical 40wt% Cu-BHA sample. The nanocomposite shows a typical hysteresis of a type-IV adsorption isotherm characteristic for mesoporous materials. The pore size distribution calculated via BJH-analysis of the desorption branch of the isotherm (figure 29, right) shows that the nanocomposite has a very

broad pore size distribution with an average pore diameter around 20nm, which assures good accessibility of the Cu nanoparticles for reaction at the high-temperature conditions of CLC.

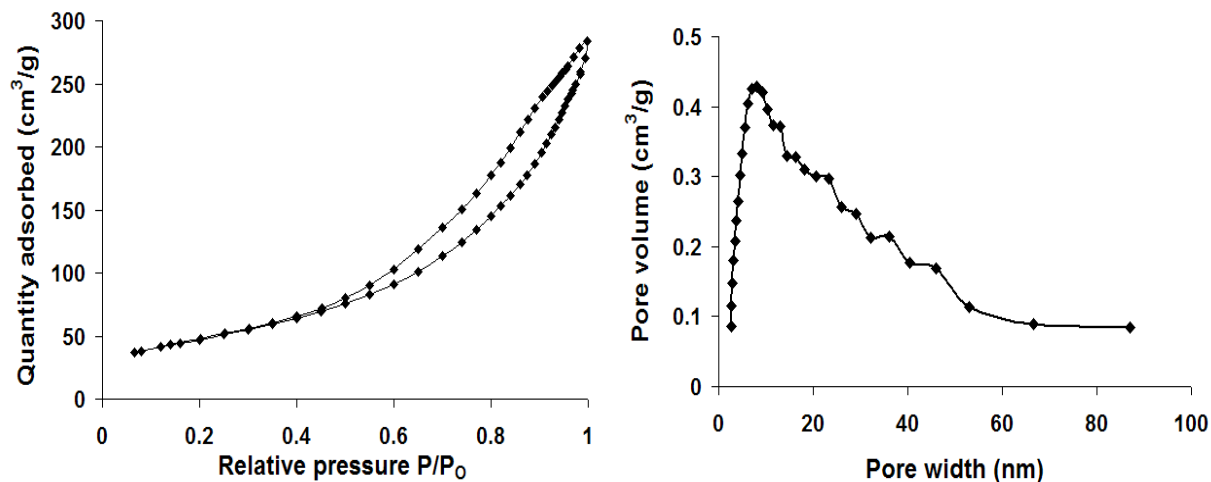


Figure 29. Nitrogen adsorption isotherm (left) and pore size distribution (right) of 40wt% Cu-BHA

4.2.2 Reactive tests

Kinetics of the desulfurization was studied in a fixed bed reactor. A quartz glass tube of 1/4" diameter was used as a reactor. 130mg of Cu-BHA was placed inside the reactor which was placed in an electric oven (Thermo Electron Corporation – Lindberg / Blue M). The oven was heated to the desired temperature and a dry syngas with or without sulfur contamination (see table 4) and air (0.1 grade) were flown alternating at a flow rate of 5 sccm to simulate the periodic oxidation and reduction in CLC. In between oxidation and reduction of the carrier the reactor was purged with Argon (5.0 grade) to avoid formation of explosive mixture of air and syngas inside the reactor. The duration of oxidation, reduction and purge phase in a typical experiment were 10-25 min., 6-10 min., and 20-30 min., respectively. Exit gases from the reactor were recorded using a mass spectrometer (Omnistar QMS 200).

4.3 RESULTS AND DISCUSSION

4.3.1 Reactivity of Cu-BHA

In order to characterize the Cu-BHA nanocomposite carriers in their oxidized and reduced state, Cu-BHA was first oxidized and reduced in air and sulfur-free syngas, respectively, in a fixed bed reactor at 900°C, and then characterized via XRD. Figure 30 shows the respective diffractograms of the reduced and oxidized samples. The presence of Cu reflexes and absence of Cu-oxide reflexes in the diffractogram of the reduced sample demonstrates complete reduction of the carrier, while the presence of CuO reflexes and absence of Cu reflexes in the diffractogram of the oxidized sample verifies complete re-oxidation of the carrier, confirming easy accessibility and high reactivity of the Cu nanoparticles in the Cu-BHA carriers.

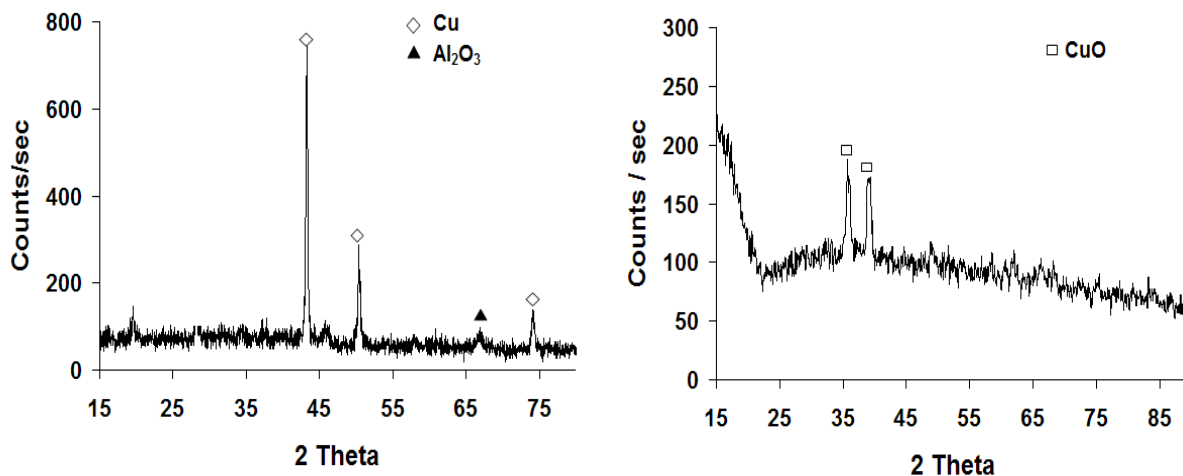


Figure 30. XRD diffractogram of Cu-BHA reduced in sulfur-free syngas (left) and re-oxidized in air (right) at 900°C

4.3.2 Cyclic operation with sulfur free synthesis gas

Once the reactivity of Cu-BHA for oxidation and reduction was confirmed, the carriers were subjected to cyclic redox tests with H₂S-free syngas in a fixed-bed reactor at 900°C in order to establish a reference point for further tests with S-contaminated syngas. The exit gases from the reactor were recorded using mass spectrometer. Figure 31 (top) shows six representative redox cycles. Shown are CO and CO₂ concentrations during the reduction half-cycle, and N₂ and O₂ concentrations during the oxidation half-cycle. As expected from our previous investigations [57,59], stable operation was observed even at 900°C, i.e. at the high-temperature limit of the temperature range for our investigations.

Figure 31 (bottom - left) shows a closer look into a single reduction cycle. At t=0 min., syngas is introduced to the reactor, which contains the carrier in oxidized state (from the previous oxidation cycle). The onset of CO₂ and H₂O as soon as syngas is fed to the reactor indicates the reduction of CuO. Complete breakthrough of CO and H₂ is observed after approximately 4 minutes, indicating complete reduction of CuO to Cu, i.e. exhaustion of the oxidation capacity of the carrier. Quantitative analysis shows that, before the breakthrough, essentially complete conversion of H₂ is achieved ($X_{H_2} > 99.96\%$), whereas CO conversion is limited to ~94%. Since H₂ is more reactive than CO it is not surprising to see a higher conversion for hydrogen than CO, in agreement with previous reports for chemical looping combustion of synthesis gas over Cu- and Fe-based carrier materials [62-63].

Figure 31 (bottom - right) shows a single oxidation cycle, where a complete breakthrough of O₂ after approximately 9 minutes indicates complete oxidation of Cu to CuO. No detectable amount of CO₂ or CO was observed over the entire re-oxidation half-cycle, indicating that no significant coke formation occurred during the reduction with syngas.

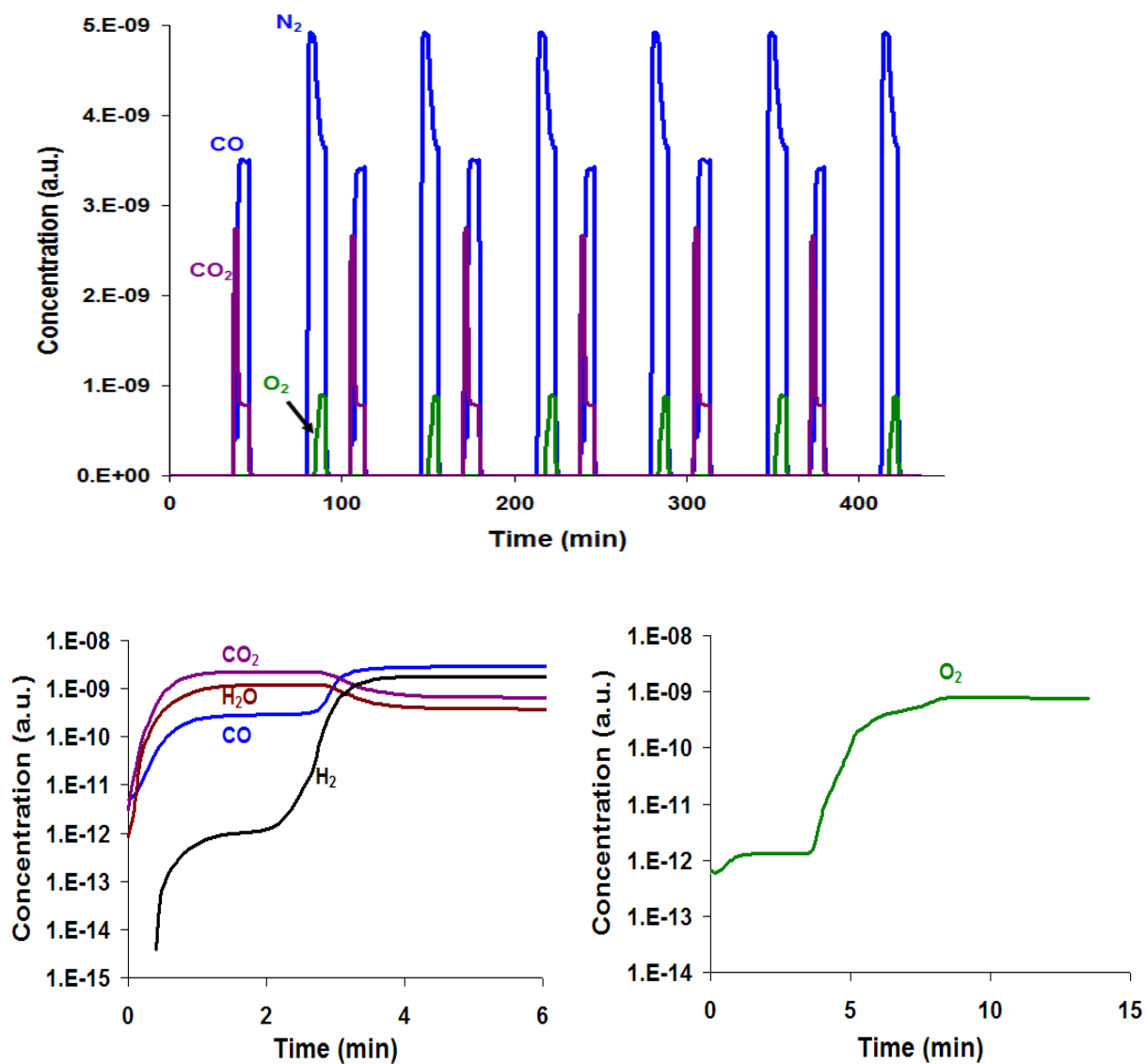


Figure 31. Top: Select representative redox cycles for Cu-BHA oxidized and reduced in air and sulfur-free syngas, respectively (flow rates of syngas and air= 5 sccm, $T= 900^{\circ}C$, $P= 1atm$). Bottom: Blow-up of a single reduction half-cycle (left) and oxidation half-cycle (right)

4.3.3 Impact of sulfur contaminants

In order to identify the impact of exposure to sulfur contamination on the carriers, Cu-BHA was first oxidized and reduced in a fixed-bed reactor at $900^{\circ}C$ in air and a syngas with 1vol% H_2S ,

respectively. Figure 32 shows again the results from an XRD analysis of the reduced and oxidized sample in order to identify the solid phase changes during reduction and oxidation. For the reduced sample, the presence of Cu_2S reflections indicates the (partial) sulfidation of CuO (see figure 32, left). In agreement with our previous investigations [59], the presence of BaSO_4 reflections indicates that the Ba content of the support is also getting partially sulfidized. (The presence of BaSO_4 rather than BaS , which is expected to form during sulfidation in the reducing atmosphere, is due to sample oxidation during transfer to XRD instrument). We had previously seen that this sulfidation of the Ba content of the carrier results in an increase in oxygen carrying capacity of the carriers, since Ba now also starts to act as oxygen carrier based on an additional $\text{BaS} \leftrightarrow \text{BaSO}_4$ cycle [59]. Thus, exposure to sulfur contamination gives rise to a "hybrid carrier" where both the metal Cu content and BaS act as oxygen carrying component of the carrier.

Upon re-oxidation of the carrier, BaS is oxidized to BaSO_4 , i.e. once Ba is sulfidized this sulfur remains stable in the carrier structure, while both Cu_2S and metallic Cu are quantitatively oxidized to CuO (see figure 32, right graph), i.e. Cu is completely regenerated and the sulfur captured by the Cu content of the sample is released during the oxidation process.

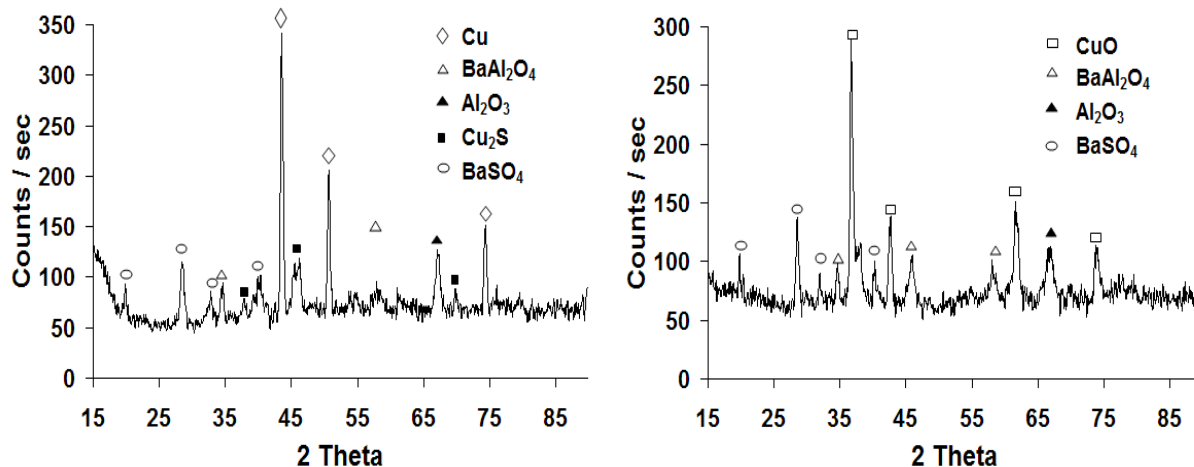


Figure 32. X-ray diffractogram of CuO-BHA reduced in syngas with 1% H₂S (left) and re-oxidized in air at 900°C (right)

4.3.4 Cyclic operation with sulfur containing synthesis gas

In order to study the impact of the above described phase changes due to H₂S exposure on the operation of Cu-BHA in the cyclic redox reactions characteristic for CLC, Cu-BHA was subjected to cyclic oxidization and reduction with air and syngas with 1% H₂S, respectively. The experiment was carried out in a fixed-bed reactor and at three different temperatures of 600, 700 and 900°C. Exit gases from the reactor were again recorded using mass spectrometry. As reported previously, stable operation was observed over the entire temperature range. Figure 33 (left) shows again a single reduction cycle at the highest operating temperature of 900°C. There are four striking differences compared to the reduction in absence of H₂S (see figure 31, bottom left). First, it can be seen that complete breakthrough of CO and H₂ are observed only after 6 minutes (i.e. delayed by ~2 min.), indicating that complete reduction of the carrier in presence of H₂S takes longer than complete reduction in absence of H₂S. This can be explained by the added oxygen carrying capacity of the sulfidized carrier, i.e. the above described formation of an

additional $\text{BaS} \leftrightarrow \text{BaSO}_4$ cycle. Second, no H_2S is detected over the first ~ 7 min. of the half-cycle, i.e. including the entire duration of the reduction, indicating that H_2S concentrations are reduced from the 10,000 ppm at the inlet to below the detection limit of our mass spectrometer of ~ 25 ppm. Clearly, Cu-BHA acts as expected as a very efficient S-capturing component in these experiments. Third, COS is detected as soon as the sample has been completely reduced (at $t \sim 6$ min.). This indicates that once the oxygen capacity of the carrier is exhausted, CO in the syngas apparently reacts with the sulfur in the carrier to form COS (a direct, non-catalytic gas phase reaction between H_2S and CO in the syngas is unlikely since no COS is detected before the fixed bed). This is significant since it indicates that undesirable COS formation can be avoided in this process, but that a precise timing of the flow switching between oxidation and reducing half-cycles is critical in order to achieve this. Finally, and surprisingly, formation of a small amount of SO_2 is also observed. This SO_2 formation starts about half-way through the reduction phase and stops once the carrier is fully reduced. Formation of SO_2 hence appears to be the result of reaction of H_2S with a partially reduced carrier, which will be further discussed below.

Figure 33 (right) shows a single re-oxidation cycle at 900°C . SO_2 is detected right from the beginning of the oxidation half-cycle, goes through a maximum after about 2 min., and then tails off, disappearing entirely once the carrier is completely oxidized as indicated by a complete breakthrough of O_2 . This suggests that sulfur is preferentially oxidized during the initial stage of the carrier re-oxidation, presumably due to a high sulfur concentration on the Cu particle surface since diffusion of the large S is expected to be hindered in comparison to oxygen bulk diffusion. The observations further confirm that sulfur captured during the reduction of the carrier can be efficiently recovered as SO_2 during the re-oxidation of the carrier.

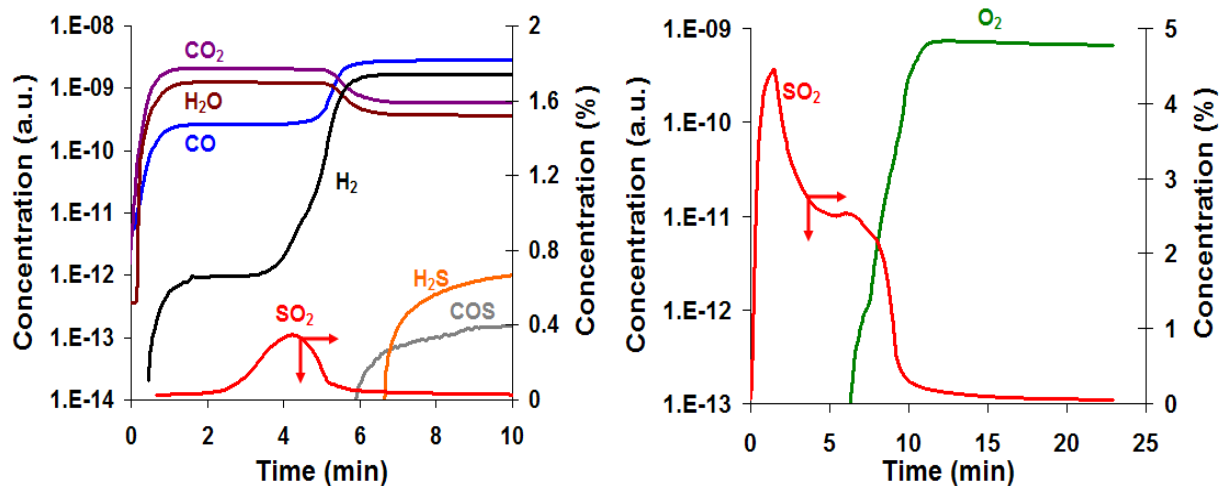
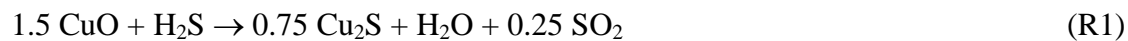


Figure 33. Reduction of CuO-BHA in syngas with 1% H₂S (left) and oxidation in air (right) at 900°C

4.3.5 Mechanism of sulfidation

The above observations essentially confirm that an efficient S-capturing based on the Cu-content of the oxygen carrier should be possible. However, the results also showed some undesirable SO₂ formation during the reduction cycle, which limits the efficacy of the S-capture. In order to understand the occurrence of this "reduction SO₂", we will briefly discuss the possible reaction pathways during Cu sulfidation and their importance for the present system.

Generally, sulfidation of CuO by H₂S can occur via two different pathways, as shown below. In the first case, if no reducing gas is present, H₂S has been shown to react directly with CuO to produce Cu₂S and SO₂ [64]:



However, if strongly reducing gases - such as CO or H₂ - are present along with H₂S, CuO is preferentially reduced first rather than reacting with H₂S via reaction R1. Reduction of

CuO nanoparticles follows a two step process [65]. CuO is first reduced to Cu₂O and then to metallic Cu:



In this case, H₂S reacts with Cu₂O and metallic Cu to produce Cu₂S [64]. However, note that in these reactions no SO₂ is produced:



Thus, sulfidation of CuO can follow three different reaction routes, R1, R6 and R7, depending on the availability of reducing gases versus H₂S. Figure 34 shows the thermodynamic feasibility of these three sulfidation reactions between 600 and 900°C. It can be seen that all three reaction have very large equilibrium constants, i.e. are thermodynamically feasible between 600 and 900°C, with R7 least favored and R1 most favored.

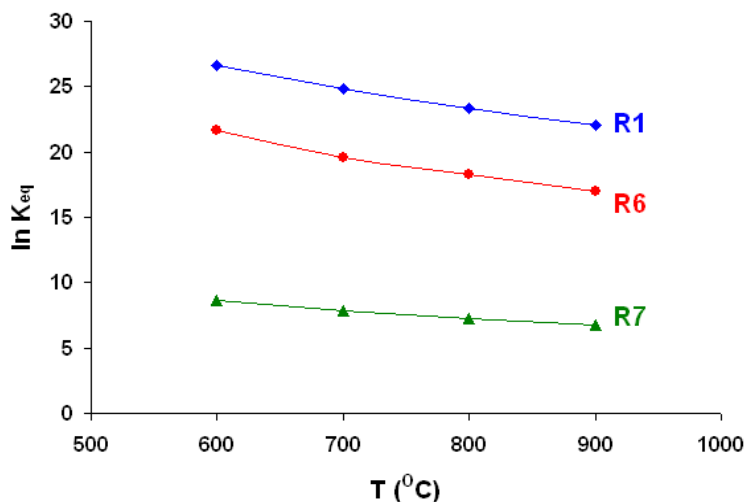


Figure 34. Equilibrium constants for Cu, Cu₂O, and CuO sulfidation reactions between 600°C and 900°C

4.3.6 Effect of BaSO₄ on sulfidation of CuO

Based on this sulfidation mechanism, SO₂ can only be produced by reaction R1, which proceeds only in the absence of a reducing gas [64]. However, in our experiments, SO₂ formation is observed even in the presence of CO and H₂ (see figure 33, left). This suggests that during the course of the reduction, the availability of the reducing gases for CuO reduction is decreased and hence reaction R1 can occur. We propose that this is explained by the presence of the BaS \leftrightarrow BaSO₄ cycle in the Cu-BHA samples. XRD analysis of the oxidized carrier (see figure 32, right) show the presence of BaSO₄, which is also reduced by CO and H₂ in the reduction cycles [59]. Hence, the availability of CO and H₂ for the reduction of CuO decreases, CuO becomes available for reaction R1, and SO₂ is hence produced. Thus, presence of BaSO₄ is responsible for the production of SO₂ during the reduction of the carrier. This explanation for SO₂ production during the reduction of Cu-BHA is consistent with experimental results obtained by Yasyerli et al. who studied sulfidation of CuO and mixed oxides of Cu-V and Cu-Mo with H₂S [64]. They

demonstrate that no SO_2 is produced when CuO is contacted with a stream of 1% H_2S and 10% H_2 in He . However, SO_2 production was observed when mixed oxides of Cu-V and Cu-Mo were contacted with the same gas mixture, which was attributed to the reduced availability of H_2 for reduction of CuO .

Hence, while the formation of the BaS phase as an additional oxygen carrier was a surprising and welcome observation in our previous studies, where increases in oxygen carrying capacity of up to ~60% were observed due to the added $\text{CuS} \leftrightarrow \text{CuSO}_4$ cycle, this additional oxygen reservoir limits the efficiency of S -capture under the conditions of the present experiments [59].

4.3.7 Effect of temperature

Due to the expected strong impact of temperature on the kinetics of the redox process as well as the S -capturing capability of the carriers, further fixed-bed experiments with H_2S -contaminated syngas were carried out at 700 and 600°C. At each temperature, multiple oxidation and reduction cycles were carried out and gas phase concentrations were recorded via mass spectrometry. Figure 35 and figure 36 show single reduction and oxidation cycles at 700 and 600°C, respectively.

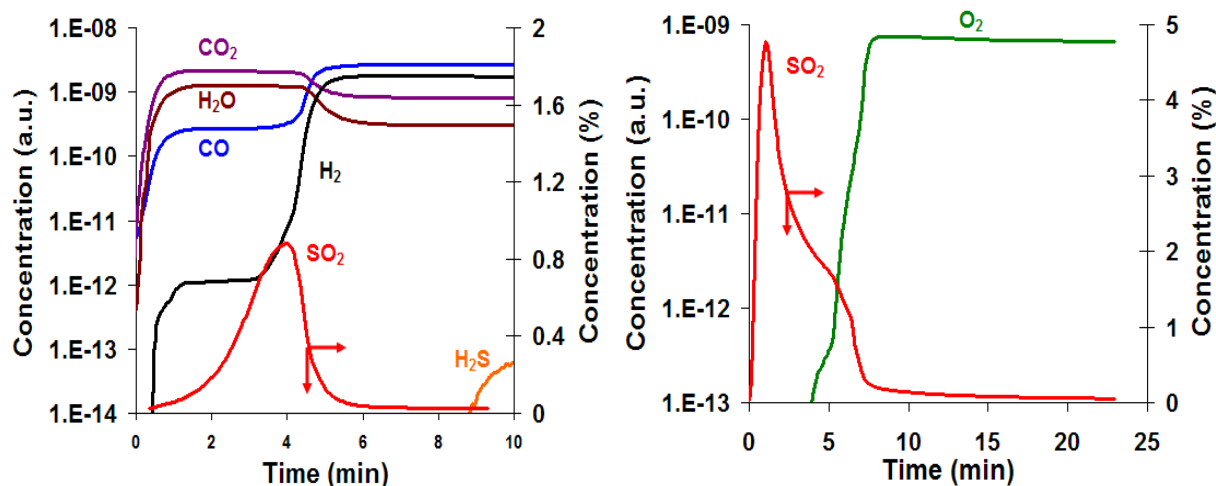


Figure 35. Reduction of CuO-BHA in syngas with 1% H₂S (left) and oxidation in air (right) at 700°C

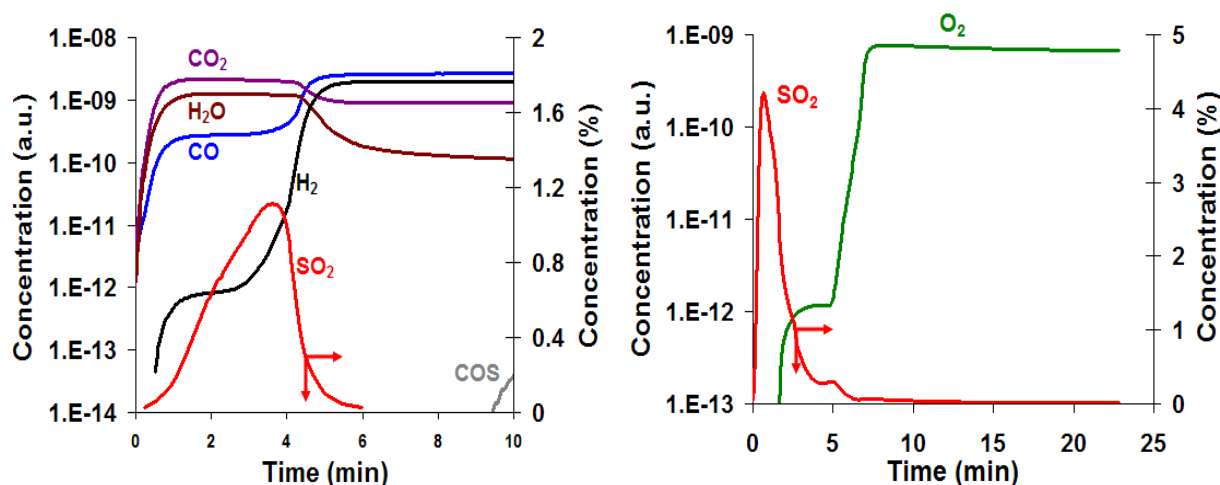


Figure 36. Reduction of CuO-BHA in syngas with 1% H₂S (left) and oxidation in air (right) at 600°C

Figure 35 (left) and figure 36 (left) show that there is no significant change in time required for complete reduction of the carrier when compared with results at 900°C (see figure 33, left). Apparently, the redox kinetics for the highly active Cu nanoparticles is so fast at all temperatures studied here that the conversion is mass-transfer limited, in agreement with our earlier findings [56]. With decreasing temperature, H₂S and COS formation is delayed and reduced, with no H₂S and no COS detectable over the first 8 min. at 600 and 700°C, respectively. At both lower temperatures the formation or break-through of these undesirable species hence

becomes sufficiently separated in time from the reduction process that they do not pose a concern at practical operation any more.

The re-oxidation of the samples at 700°C and 600°C is shown in the right-hand graphs in figure 35 and figure 36, respectively. Unexpectedly, one can see that the time required for complete re-oxidation becomes shorter with decreasing temperature. This is surprising at first, since a decrease in temperature should result in slower kinetics and hence a longer duration for full re-oxidation. However, the reason for the acceleration can be found in the different degrees of sulfidation of the samples: A clear trend towards significantly compressed SO₂ signals in the re-oxidation cycles with decreasing temperature indicates that the samples are less deeply sulfidized and hence re-oxidation is accelerated due to the reduced amount of oxygen (and hence time) required to remove the sulfur in the form of SO₂.

The trend in sample sulfidation with temperature are summarized in figure 37, where the effect of temperature on SO₂ production during the reduction (left) and re-oxidation (right) of the carrier is shown in direct comparison between the three experimental temperatures.

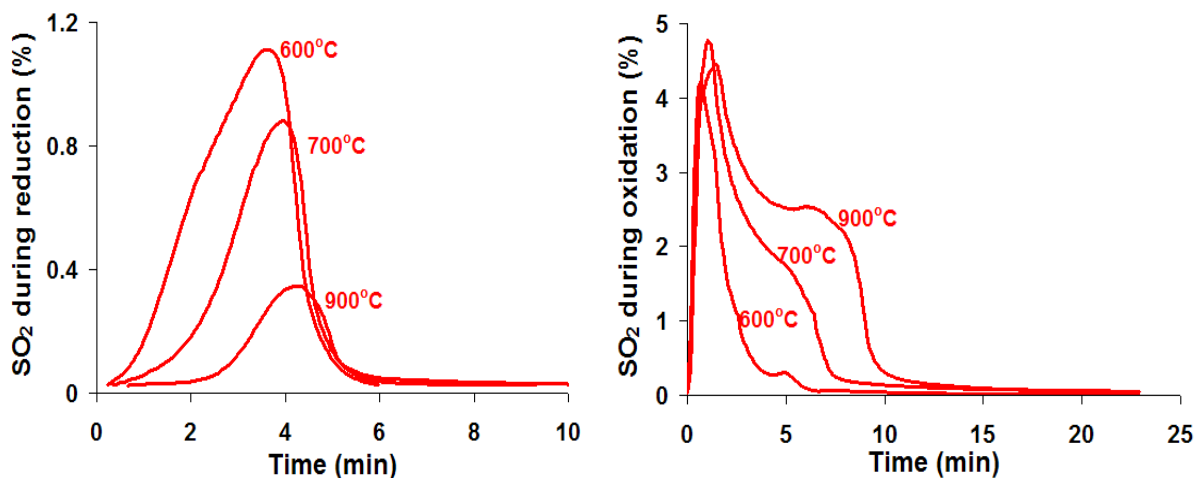


Figure 37. SO₂ production during reduction (left) and oxidation (right) at three different temperatures (T= 600°C, 700°C, 900°C)

The SO_2 trace during the reduction of the carrier (figure 37, left graph) shows two pronounced trends: SO_2 production decreases and the onset of SO_2 formation is delayed with increasing temperature. Similarly, the SO_2 trace during re-oxidation shows two distinct features: A sharp initial peak, which is temperature-invariant, followed by a broad shoulder, which is almost absent at 600°C and becomes very pronounced with increasing temperature.

The trends during the reduction cycle can again be explained by the mechanism detailed above: SO_2 formation occurs along (R1), i.e. only in the presence of unreduced CuO . While CO and H_2 quickly reduce CuO to Cu_2O and Cu , and hence largely suppress SO_2 formation, the presence of the (reducible) BaSO_4 phase results in reduced syngas partial pressures and hence leaves some CuO available for reaction (R1). With decreasing temperature, however, both the reaction of BaSO_4 with syngas as well as the reduction of CuO to Cu_2O and Cu by syngas are slowing down, leaving more CuO available for reaction with H_2S , and hence result in an increasing amount of SO_2 formation.

The two stages in the SO_2 formation during re-oxidation, on the other hand, can be attributed to surface and bulk sulfidation of the carriers: At lower temperature (600°C) bulk diffusion processes are very slow and hence the process is almost entirely dominated by surface sulfidation, which is removed very fast during re-oxidation. In agreement with this, this surface sulfidation peak is virtually unaffected by temperature, since the surface sulfur layer is present at all temperatures. However, with increasing temperature, deeper bulk sulfidation of the Cu particles becomes possible, giving rise to a much slower, secondary process during re-oxidation, which shows up as the pronounced shoulder in the re-oxidation trace.

Obviously, an ideal carrier should capture all sulfur present in the syngas feed without any production of SO_2 or other sulfurous gases during the reduction phase, and should allow

quantitative recovery of the captured sulfur during re-oxidation. Clearly, the present carriers fail to meet this specification, since some SO_2 is produced during the reduction of the carrier at all temperatures. If SO_2 production during the reduction of the carrier is significant, it may make the intended desulfurization scheme unpractical since it might necessitate additional separation of SO_2 from the fuel reactor effluent, defeating the purpose of the proposed process scheme.

Figure 38 quantifies the relative amounts of sulfur species during the complete reduction and re-oxidation of the carrier as a fraction of the S fed to the reactor as H_2S in the syngas during the reduction phase (“fuel H_2S ”). No significant amount of H_2S or COS (< 25 ppm) is detected during the time required for complete reduction of the carrier at any temperature. With increasing temperature, the amount of SO_2 produced during the reduction of the carrier decreases and the amount of SO_2 produced during the oxidation of the carrier increases, i.e. sulfur capture is more effective at higher temperatures. At 900°C about 90% of the H_2S fed into the reactor is captured as SO_2 in the air-reactor effluent. However, the remaining 10% remain (again as SO_2) in the fuel reactor effluent, significantly limiting the efficiency of the proposed scheme. While the trends in figure 38 suggest that operation at even higher temperature should result in further reduction of the S-breakthrough on the fuel reactor side, the relatively low melting point of Cu ($\sim 1,065^\circ\text{C}$) makes higher operating temperatures questionable.

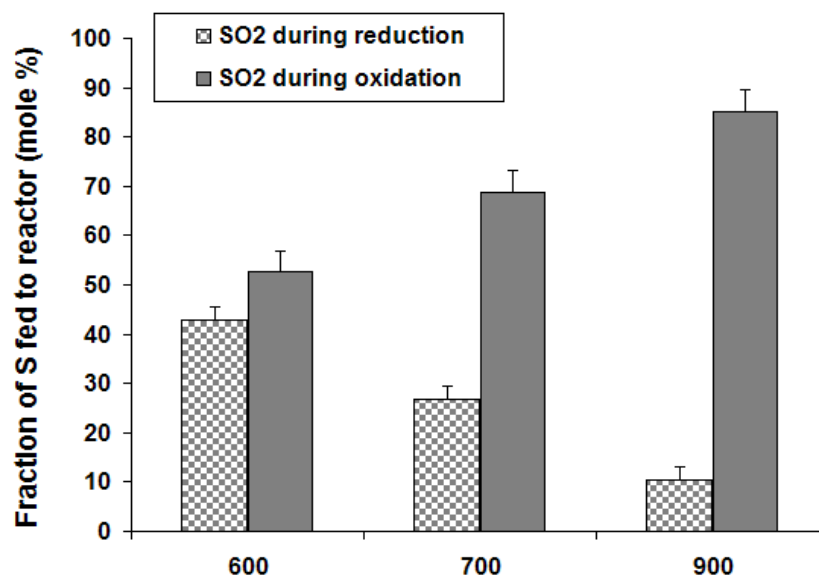


Figure 38. Sulfur species during the reduction (shaded) and oxidation (solid) at the three different temperatures

However, based on the presented results, at least two strategies can be proposed which should allow efficient deep desulfurization of the fuel reactor effluent with essentially complete recovery of the sulfur in the air reactor effluent: On one hand, our results suggest that utilization of a different support matrix, which is non-reducible and does not interact with the fuel sulfur (to form a reducible sulfate phase), should allow implementation of the proposed scheme for simultaneous desulfurization and CO₂-capture via chemical looping. On the other hand, even with the present carrier deep desulfurization would be attainable at 900°C, if the carrier reduction is stopped at an early time point (at $t \sim 3$ min. in our experiments; compare figure 33, left graph), i.e. before significant SO₂ formation occurs. While this would limit the reactor throughput (or space-time-yield) to about 60% of the attainable maximum based on the carrier reduction alone, it would allow almost entire elimination of SO₂ formation without requiring changes to the carrier, which might result in the loss of the exceptional activity and stability of the present Cu-BHA nanocomposite carrier materials.

4.4 SUMMARY

In this chapter, we proposed a novel scheme for chemical looping combustion with integrated deep desulfurization of the fuel reactor effluent, which would allow capturing CO₂ and SO₂ in two separate effluent streams. Again, realization of this scheme depends on the selection of an appropriate carrier. Based on thermodynamic screening calculations, Cu was chosen in the present study, and a nanostructured Cu-BHA carrier was synthesized and tested in fixed-bed reactor studies over a temperature range of 600-900°C. The carrier was able to reduce the S content in the effluent by up to 90% during cyclic reduction and oxidation with a syngas containing 1% H₂S and air, respectively. The sulfur captured by the carrier during the reduction half-cycle is quantitatively recovered during re-oxidation. The efficiency of the process is limited due to some SO₂ formation during the reduction phase, which was attributed to the presence of a reducible BaSO₄ phase in the oxidized carrier.

Nevertheless, the results suggest that the proposed process for simultaneous deep desulfurization and CO₂ capture is feasible if a proper support material is chosen (which should be non-reducible and resistant against sulfidation), or if the cycle time during the reduction of the present carrier is properly adjusted. Overall, the proposed integrated process would hence result in a novel, strongly intensified process for low-emission, high efficiency combustion of sulfur contaminated fuel streams.

5.0 HYDROGEN PRODUCTION VIA CHEMICAL LOOPING STEAM REFORMING (CLSR) IN A PERIODICALLY OPERATED FIXED BED REACTOR

In principle CLC can be carried out with any oxidizing gas as long as it is reactive towards oxygen carrier material. When air is replaced by steam as oxidizing agent ultra-pure hydrogen stream is produced at the exit of the oxidizer. This process is referred as chemical looping steam reforming (CLSR). Since CLSR is CLC derived technology most of the issues in CLC are also present in CLSR. Major challenges for CLSR are slow oxidation kinetics, since steam is a weaker oxidant than air, insufficient high temperature stability of many carrier materials, and particle attrition in the circulating fluidized-bed configuration of typical CLC process schemes.

In this chapter, we report results from a feasibility study of CLSR which aims to directly address the above issues: First, thermodynamic calculations were conducted to screen for suitable metal-based carriers for CLSR. Then, nanostructured oxygen carriers were synthesized as highly active and high-temperature stable materials and their activity and stability was evaluated in reactor studies. Finally, a brief reactor modeling study was conducted to evaluate the feasibility of CLSR in a periodically operated fixed-bed reactor in order to avoid carrier attrition associated with the use of fluidized beds.

5.1 CHOICE OF THE CARRIER

As a first step, a detailed thermodynamic screening study of a broad range of metals was conducted in order to identify promising candidates for CLSR. A commercial software package (FACTSAGE 5.0) was used to evaluate the equilibrium conversion for a stoichiometric mix of steam with the respective metals or partially reduced metal oxides. Figure 39 (left) shows results in terms of steam conversion vs temperature for select carriers, where steam conversion is defined as usual as $X_{\text{H}_2\text{O}} = 1 - N_{\text{H}_2\text{O},\text{equil}}/N_{\text{H}_2\text{O},\text{initial}}$. Only metals with any significant degree of conversion are shown in the graph.

While a range of metals show very high steam conversion over the entire temperature range, most had to be discarded either due to low melting points, toxicity of the metal, or the irreversibility of the oxidation process. Among all screened metals, Fe and its lowest-valent oxide FeO showed most promise as carrier for CLSR, combining good reactivity with low cost and low toxicity. This result agrees of course with the long history of iron as metal-of-choice in the "steam-iron process". (All thermodynamic results shown here are calculated for $P = 30$ bar. However, due to the nature of the net reaction, the equilibrium is essentially invariant to pressure changes, as verified over the range of $P = 1 - 30$ bar).

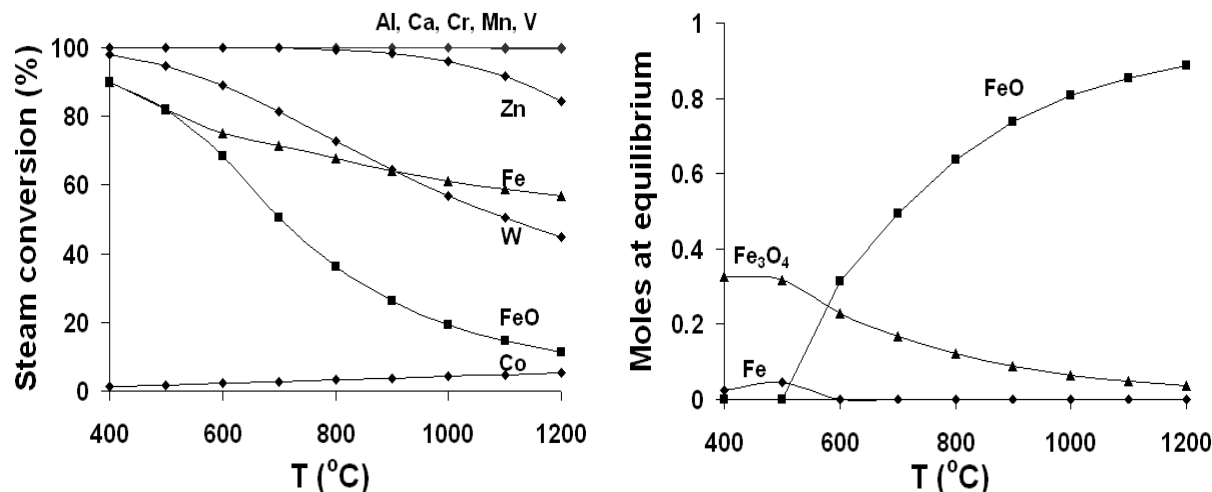


Figure 39. Equilibrium conversion of steam versus temperature for select metals and metal oxides (left), and Fe/oxide phases versus temperature for a stoichiometric FeO:steam ratio (right)

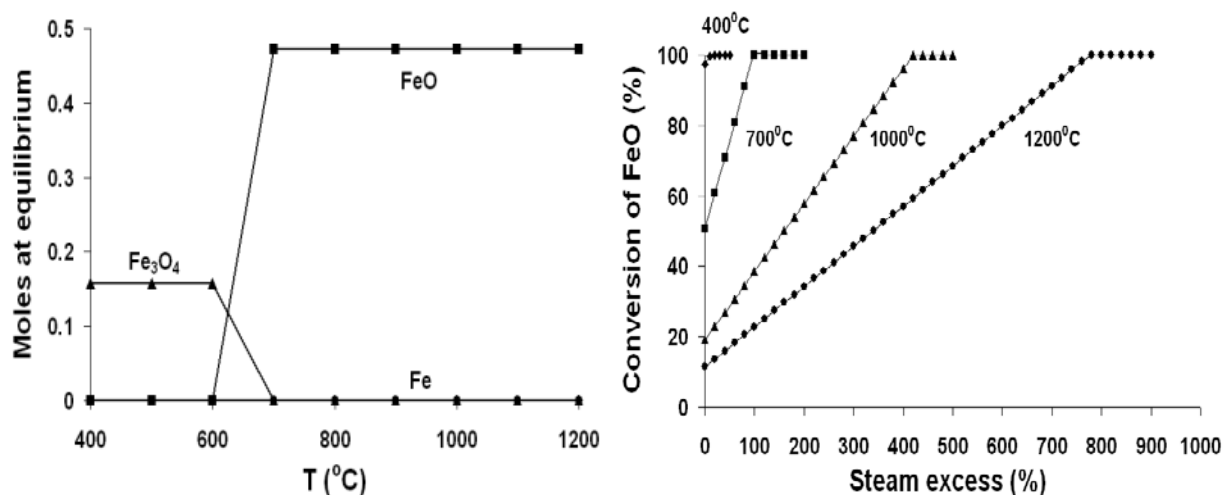


Figure 40. Fe/oxide phases v/s temperature for stoichiometric Fe₃O₄:syngas ratio (left), conversion of FeO to Fe₃O₄ v/s excess steam for four different temperatures (right). Steam "excess" is defined relative to stoichiometric feed for complete conversion to Fe₃O₄ (excess = 0). 100% excess thus refers to 2-fold stoichiometric supply

A more detailed look at the iron oxide phases present at equilibrium (figure 39, right graph) shows that the oxidation process is limited to the formation of Fe₃O₄, i.e. neither Fe nor FeO can be fully oxidized to Fe₂O₃ at the given conditions. In fact, at temperatures above 500°C, even Fe₃O₄ becomes unstable, explaining the limit on the attainable steam conversion seen in the

calculations (figure 39, left). The choice of FeO as the reduced (i.e. initial) state of the carrier in the calculations is based on thermodynamic calculations for the reduction for Fe_3O_4 with stoichiometric amounts of syngas (for composition see table 1), which show that the oxide can only be reduced to FeO (see figure 40, left graph). (No other Fe-compounds - beyond Fe, FeO, and Fe_3O_4 - were obtained at the conditions studied; in particular no formation of highly volatile and toxic carbonyls was observed during the reduction with syngas.)

The usable oxygen carrying capacity of Fe-based carriers for the present process is hence limited to Fe_3O_4 as upper and FeO as lower bound, reducing the maximum accessible oxygen carrying potential from 24g O/mol Fe for the full oxidation of $\text{Fe} \rightarrow \text{Fe}_2\text{O}_3$ to 5.3g O/mol Fe. In practice, this number will be further lowered by the use of support materials for the iron component.

In order to test whether this limitation can be overcome, i.e. whether the oxidation process can be pushed further to the oxide (Fe_3O_4), additional calculations were conducted with increasing amount of “excess” steam, i.e. with over-stoichiometric supply of H_2O . Results for select temperatures are shown in figure 40 (right graph). One can see that at relatively low temperatures ($T < 700^\circ\text{C}$), full oxidation to Fe_3O_4 can be achieved with a reasonable amount of steam excess ($< 100\%$), while for high temperatures this amount increases rapidly and quickly reaches unrealistically high numbers (up to 8-fold excess for 1200°C). Similar results were obtained for the reduction with over-stoichiometric supply of syngas (not shown here). However, it should be noted that the thermodynamic calculations assume a closed reactor system, i.e. they correspond to a transport reactor configuration in which solid and gas phase move co-currently at the same velocity. In a fixed-bed reactor configuration with a stationary solid phase, or in a transport reactor with a counter-current flow arrangement, the local reactant concentrations

through the reactor will correspond more closely to a large “excess”, and one can hence expect increased conversion and carrier utilization, as shown in figure 40 (right graph).

Overall, these thermodynamic calculations demonstrate that - at least among monometallic materials - iron-based carriers are the most efficient materials for hydrogen production in a CLSR process. However, the results also point out limitations regarding the accessibility of its highest and lowest oxidation states which may significantly reduce the oxygen carrying capacity, depending on the flow configuration in the reactor. Nevertheless, the overall favorable thermodynamic redox potential combined with low cost and low toxicity makes Fe the carrier of choice for CLSR.

5.2 EXPERIMENTAL

Based on the results from the thermodynamic screening, Fe was selected as active redox component for the development of suitable oxygen carrier materials. A key target for the development was fast oxidation kinetics, since the oxidation of a metal carrier with steam can be expected to be significantly slower than with air. Additionally, iron oxides are well known to form dense oxide overlayers which severely slow reaction kinetics and limit accessibility of bulk iron. Due to the high-temperature conditions of CLSR processes, high-temperature stability, i.e. strong resistance to sintering, was a second target. The approach chosen was based on our previous work in developing nanostructured, high-temperature stable catalysts and oxygen carriers [55-56,66] and is briefly described in the following

5.2.1 Synthesis and characterization

Fe-BHA was synthesized using the same technique as described in section 3.1.1. It was characterized using x-ray diffraction, nitrogen sorption (BET), and transmission electron microscopy (TEM, JEOL 200). A typical TEM image is shown in figure 41 (left). One can see the homogeneous nanostructure of the material consisting of Fe nanoparticles (black) and the BHA matrix (grey background). The Fe nanoparticles have diameters of 15-20 nm after calcination, in agreement with our previous observations with this type of nanostructured carrier [55], and are embedded into the porous network of the BHA. Figure 41 (right) shows a typical nitrogen adsorption isotherm of these Fe-BHA nanocomposites. The isotherm shows a typical hysteresis corresponding to a type-IV mesoporous material with a broad distribution of pore sizes. Typical BET surface areas after calcination at 600°C were 100-150 m²/g.

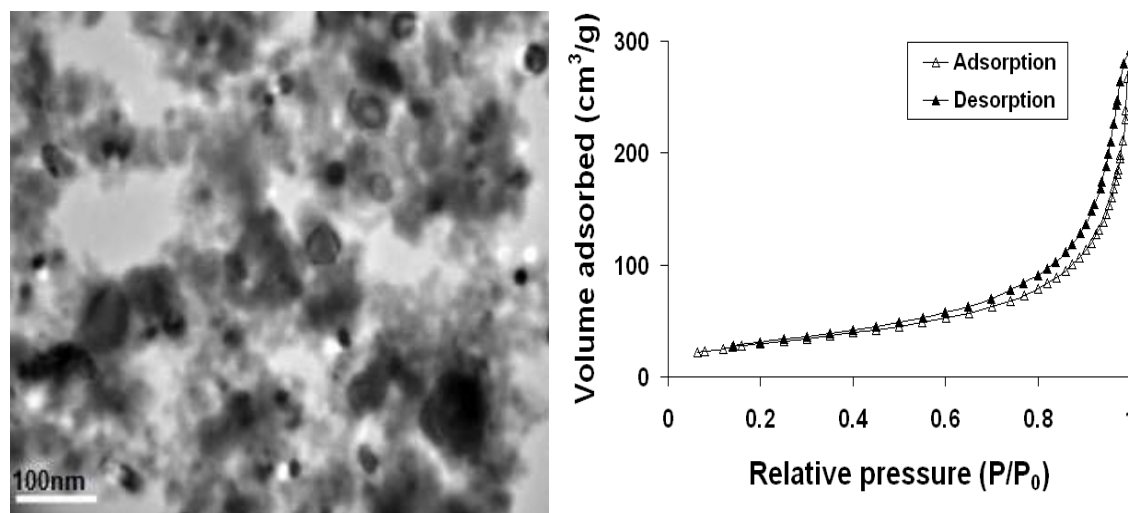


Figure 41. TEM image (left) and BET isotherm (right) of a typical nanostructured Fe-BHA (40wt% Fe) after calcination at 600°C

Figure 42 (left) shows XRD spectra of Fe-BHA which was completely reduced in Hydrogen at 800°C. Presence of strong reflexes of Fe and absence of reflexes of any higher oxides confirm

the complete reduction of the carrier. This completely reduced carrier was then subjected to oxidation in steam at 500°C. Figure 42 (right) shows the XRD spectra of sample after oxidation in steam. Presence of Fe_3O_4 reflexes confirms the oxidation of sample in steam. Reflexes of Fe are significantly reduced but not completely disappeared, which suggests incomplete oxidation of the sample (for details on incomplete oxidation refer section 5.3.2 and 5.3.3). Absence of Fe_2O_3 indicates that the oxidation process does not go beyond Fe_3O_4 which is consistent with thermodynamic results discussed in section 5.1. All carriers used in the experiments reported here had Fe weight-loading of ~40wt%.

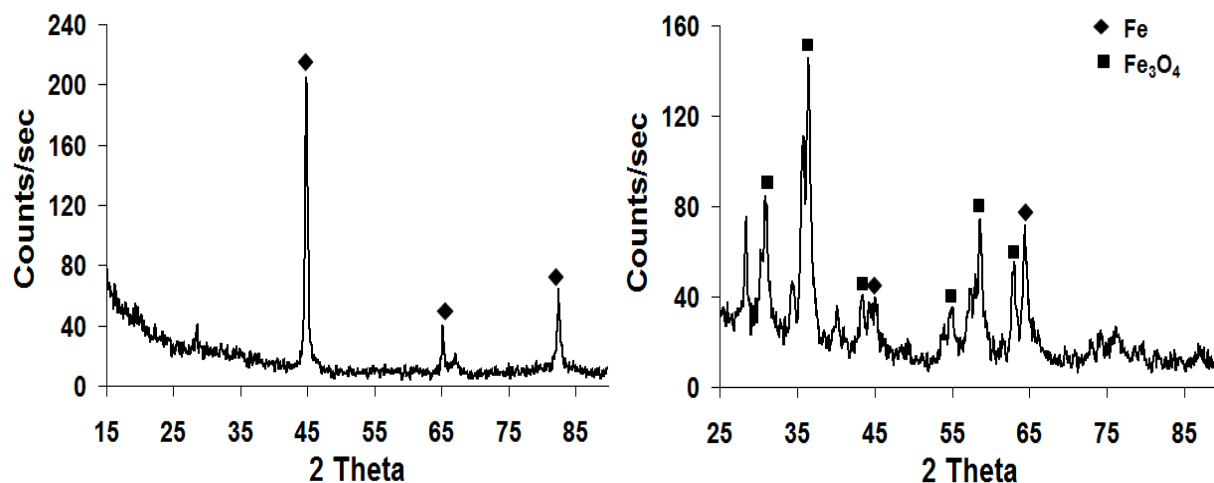


Figure 42. XRD spectra of Fe-BHA completely reduced in H_2 at 800°C (left) and corresponding sample oxidized in steam at 500°C (right)

5.2.2 Reactive tests

As a proof-of-concept study of CLSR of syngas (or “chemical looping WGS”), and in order to test the activity and stability of the nanostructured Fe-BHA carriers, fixed-bed reactor studies were conducted in a simple, externally heated tubular reactor. 200mg of Fe-BHA was placed inside a quartz-glass tube (1/4" I.D.) which was positioned in an electric oven. The assembly was

heated in an inert stream (Ar, 5.0 grade) to the desired reaction temperature, and then a dry syngas (composition see table 4— syngas w/o sulfur) and a mixture of 98.5vol% steam in Argon (5.0 grade) were flown alternating at a flow rate of 2 sccm and 230 sccm, respectively, to simulate the periodic reduction and oxidation in CLSR. The flow rates were chosen based on experimental limitations (minimum adjustable flow-rates) and to achieve good time resolution for the transient experiments. In between oxidation and reduction of the carrier the reactor was purged with argon, at a flow rate of 120 sccm, to avoid formation of poorly defined mixtures of reactive gases inside the reactor and to allow clear differentiation of products from the oxidation and reduction phase of the experiment. The duration of oxidation, reduction, and purge phases in a typical experiment were 25, 20 and 10-20 minutes respectively. Exit gases from the reactor were passed through a cold trap to condense unreacted steam before they were recorded using a mass spectrometer (Pfeiffer Omnistar QMS 200).

5.3 RESULTS AND DISCUSSION

5.3.1 Thermal stability

Figure 43 shows six representative redox cycles for the cyclic oxidation and reduction of Fe-BHA at 800°C with steam (98.5vol% in Ar) and syngas, respectively, (top graph) as well as the concentration traces for one reduction (bottom left) and oxidation half cycle (bottom right). In both cases, the concentration traces of CO, H₂ and CO₂ during the reduction of the carrier with syngas, and the concentration traces of H₂ and CO₂ produced during the oxidation of the sample with steam are shown vs time. One can see from the top graph that the carrier shows stable

operation with no changes in height or shape of the concentration traces with time within experimental error. This confirms the stability of the nanostructured carrier, at least over the duration of the experiment of several hours (it should be mentioned that the experiment was reproduced several times without changing the carrier, and no signs of deactivation due to this extended operation or the repeated shut-down and start-up were observed). While a long-term test (over 1000's of hours) is beyond the scope of the present studies, we hence expect that the material should withstand long-term continuous operation.

During the reduction phase, one can observe the break-through of CO and hydrogen after about one minute of flowing syngas. CO shows high (>90%), but incomplete conversion at all conditions, while hydrogen is consumed entirely before break-through. This is not unexpected due to the competition for carrier oxygen between these two syngas components and the known higher reactivity of hydrogen in comparison to CO.

During the carrier oxidation phase, one observes pronounced peaks in the hydrogen concentration, indicating the formation of hydrogen in the reaction between steam and the reduced carrier. Somewhat surprisingly, small CO and CO₂ peaks during this phase indicate that a small amount of carbon is being carried over from the reduction phase to the oxidation phase. This could be due either to the formation of small amounts of carbonaceous deposits on the carrier during reduction, or due to CO adsorbed on the high surface area of the nanostructured carrier during exposure to syngas, some of which then gets oxidized to CO₂ during the oxidation phase. The absolute amount of CO_x is minimal, however, remaining well in the sub-ppm range for the product gas averaged over the duration of the oxidation phase, and hence should have no impact even on the production of PEMFC-ready hydrogen streams, since CO₂ itself is not a PEMFC poison, and modern PEMFCs can tolerate CO contamination well into the 100 ppm

range[67]. Nevertheless, if the high-purity hydrogen product stream is intended for other applications with even more stringent requirements on contamination levels, including CO₂ levels, this carbon carry-over will require further consideration.

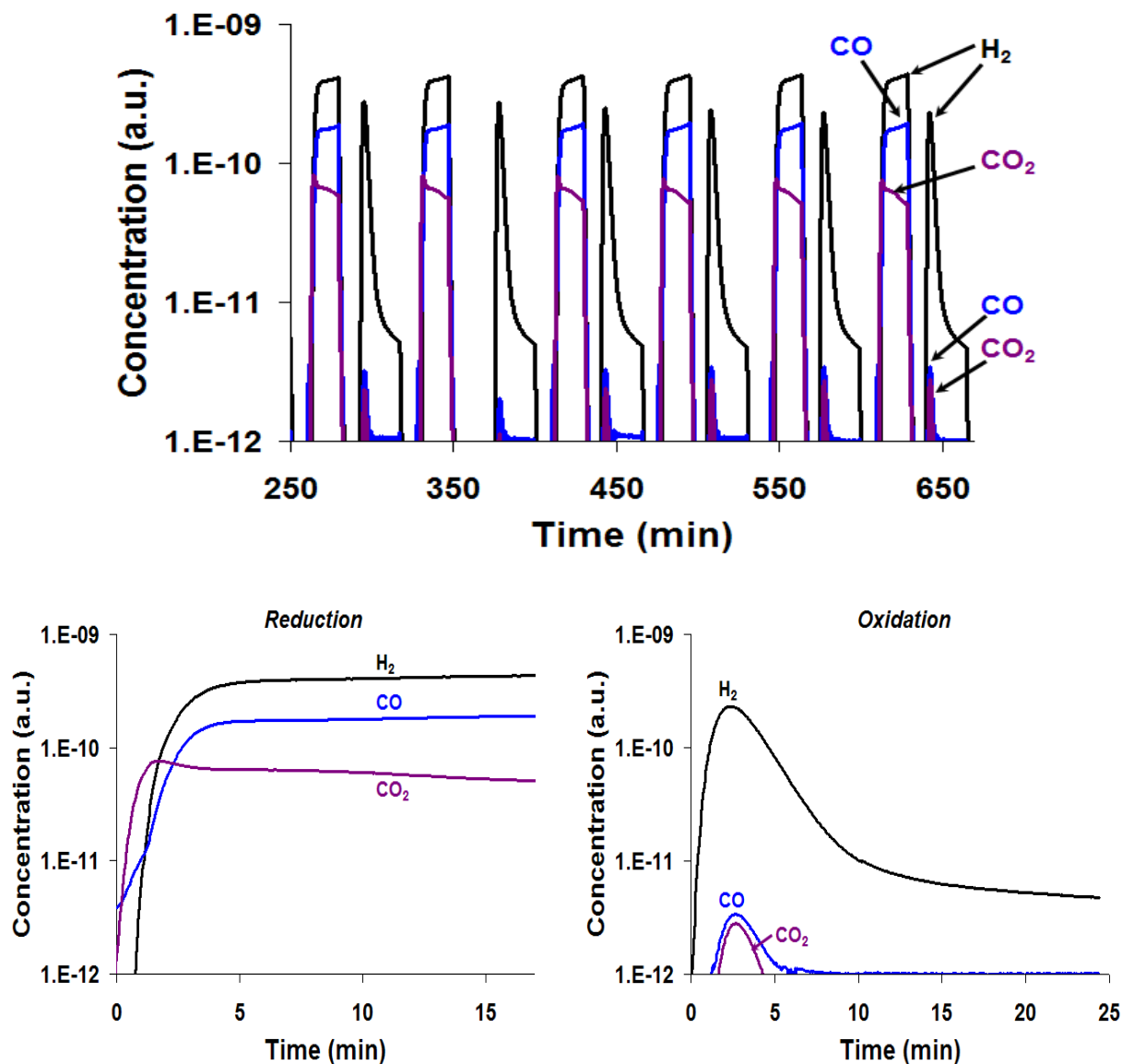


Figure 43. Six redox cycles for Fe-BHA oxidized and reduced in a mixture of steam (98.5%) in Argon and syngas, respectively (top) and a single, enlarged reduction and oxidation cycle showing the gas phase concentrations (bottom)

5.3.2 Effect of temperature

Figure 44 shows the molar flow rate of hydrogen produced during one oxidation cycle (left graph) along with the corresponding (fractional) conversion of the carrier (right graph) at four different temperatures between 500°C and 800°C. Carrier conversion is here defined as $X_{\text{carrier}} = N_{\text{H}_2} / (4 N_{\text{Fe}_3\text{O}_4} - N_{\text{FeO}})$, where N_{H_2} is the cumulative number of moles of hydrogen produced, $N_{\text{Fe}_3\text{O}_4}$ is the number of moles of Fe_3O_4 in the completely oxidized carrier and N_{FeO} the number of moles of FeO in the completely reduced carrier. Since our thermodynamic calculations indicate that FeO and Fe_3O_4 are the lowest and highest oxidation states of Fe attainable at these conditions, the denominator hence indicates the maximum possible oxygen uptake by the carrier during the oxidation phase, while the numerator represents the actual oxygen consumption from steam.

At the highest temperatures (650°C and 800°C) the oxidation kinetics is initially very fast, followed (after $t \sim 6\text{-}7$ min.) by a long trailing tail. We attribute this strong slow-down in the kinetics to a transition from a kinetically controlled process to a solid-state diffusion controlled process as the oxidation yields a Fe_3O_4 overlayer which hampers further oxidation of the FeO particle "cores". However, due to the controlled "nano-size" of the carriers, the transition to the slow diffusion controlled process occurs only after $\sim 90\%$ of the usable carrier capacity has been exhausted. Clearly, the small size of the embedded Fe nanoparticles helps to accelerate the kinetics and maximize the accessible oxygen carrying potential.

Below 600°C, the kinetics slow down very quickly with decreasing temperature, resulting in a strong drop in carrier conversion from $\sim 70\%$ at 650°C to $< 30\%$ at 500°C at the end of the oxidation phase. Interestingly, the fractional carrier conversion also drops from $\sim 70\%$ to $\sim 66\%$ upon increasing the reaction temperature from 650°C to 800°C. This suggest that the oxidation is

becoming thermodynamically limited, in qualitative agreement with our thermodynamic calculations which show a strong decrease in equilibrium conversion in this temperature range (i.e. between $\sim 600^{\circ}\text{C}$ - 900°C , see fig. 39, left graph). However, it should also be noted that the attained conversions are quantitatively well in excess of the $\sim 40\text{-}60\%$ conversion predicted for a stoichiometric mix of FeO and steam in this temperature range, which can be expected for the present fixed-bed configuration as discussed in section 5.1.

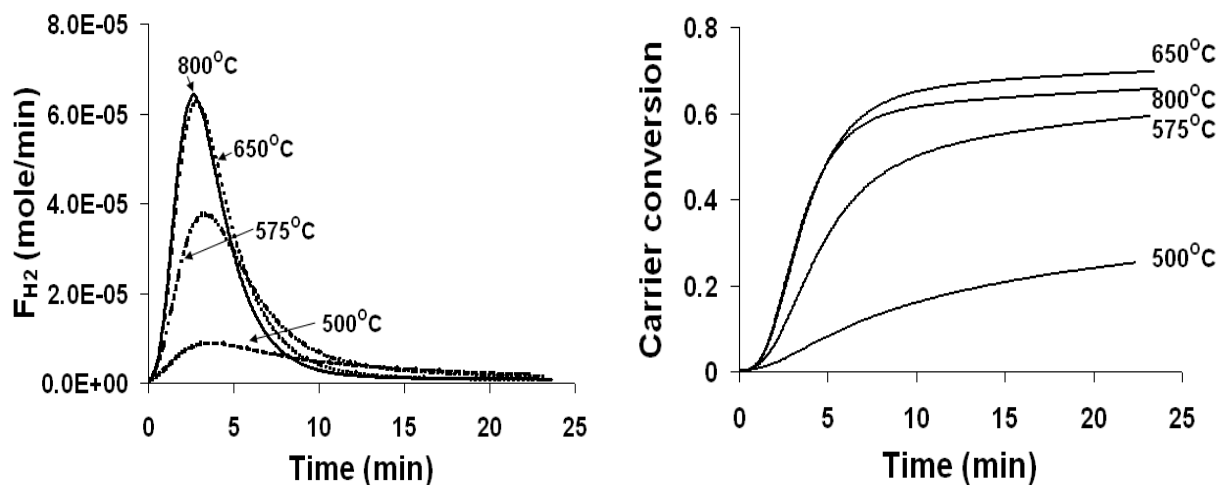


Figure 44. Hydrogen stream produced over one oxidation phase during steam oxidation of Fe-BHA at different temperatures (left), and corresponding carrier conversions (i.e. fractional oxidation) as function of time (right)

Overall, these initial results on chemical looping steam reforming of a syngas feed stream demonstrate the fundamental feasibility of CLSR processes. Hydrogen production rates as high as $4.15 \text{ mmole H}_2 / \text{g Fe}$ over a single oxidation cycle could be attained under the current, non-optimized conditions (at $T=650^{\circ}\text{C}$ for a cycle duration of 25min). As expected, iron functions as an efficient oxygen carrier between steam and the syngas mixture, and the utilization of a high-temperature stabilized nanostructured carrier allows fast and robust cycling between the oxidation and reduction phase in a fixed-bed configuration. Furthermore, the results demonstrate that by appropriate timing of the half cycles, it should be possible to attain complete conversion

of CO and H₂ in the reduction phase of the carrier combined with high yields of H₂ during the oxidation phase, hence entirely bypassing thermodynamic limitations for high-temperature WGS. More detailed investigations of the oxidation and reduction kinetics are currently under way.

5.3.3 Effect of particle size

Figure 45 shows the particle size distribution of Fe-BHA calcined at three different temperatures – 800°C, 900°C and 1000°C. Average particle diameter increases with increase in the calcinations temperature and it was 16nm, 22nm and 54nm at 800°C, 900°C and 1000°C respectively.

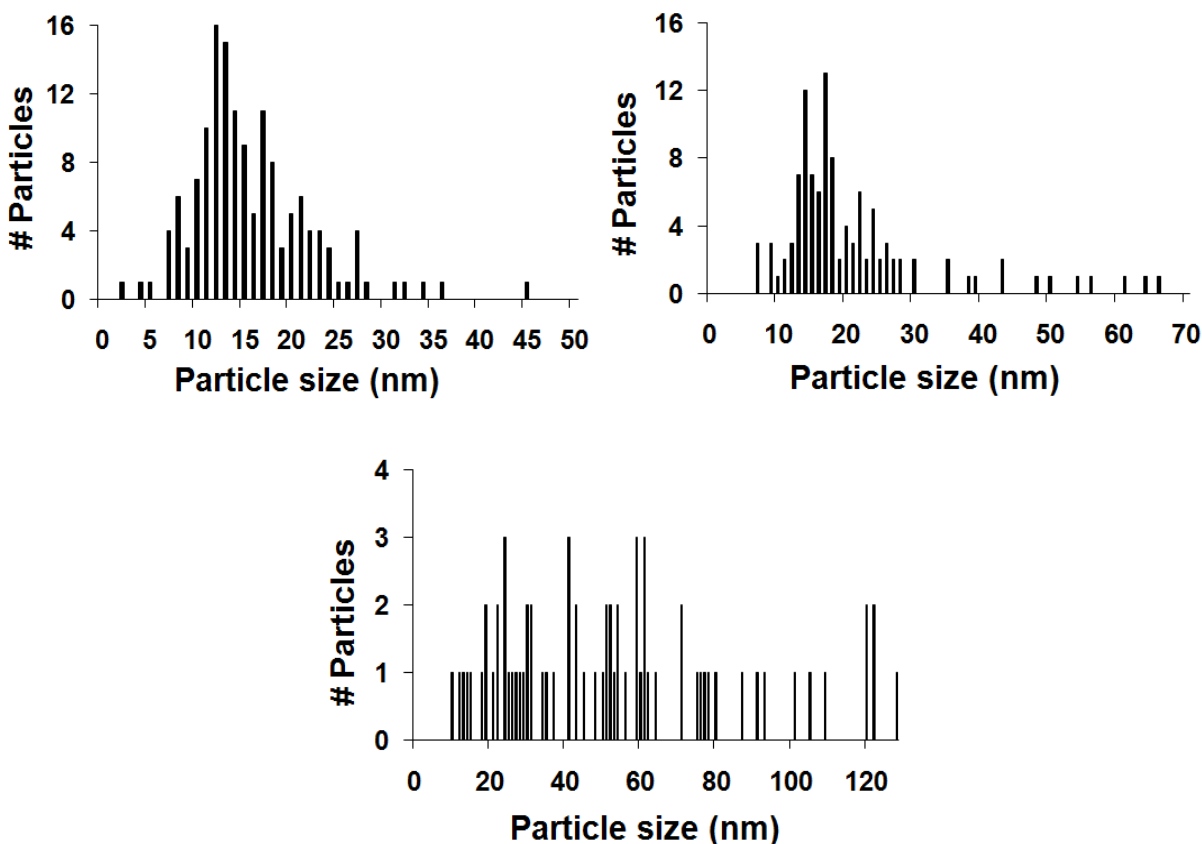


Figure 45. Particle size distribution of Fe-BHA calcined at 800°C (top left), 900°C (top right) and 1000°C (bottom)

It was expected that with decrease in particle size diffusion limitations can be minimized and final carrier conversion can be enhanced. In order to study this, Fe-BHA with average particle size of 16nm, 22nm and 54nm was subjected to conditions of CLSR as described in section 5.2.2. Figure 46 (left) shows the hydrogen production rate and figure 46 (right) shows the carrier conversion as a function of time for three different particle sizes. It can be observed that with decrease in particle size hydrogen production rate increases and consequently final carrier conversion increases. This is due to the fact that with decrease in particle size diffusion limitations are minimized.

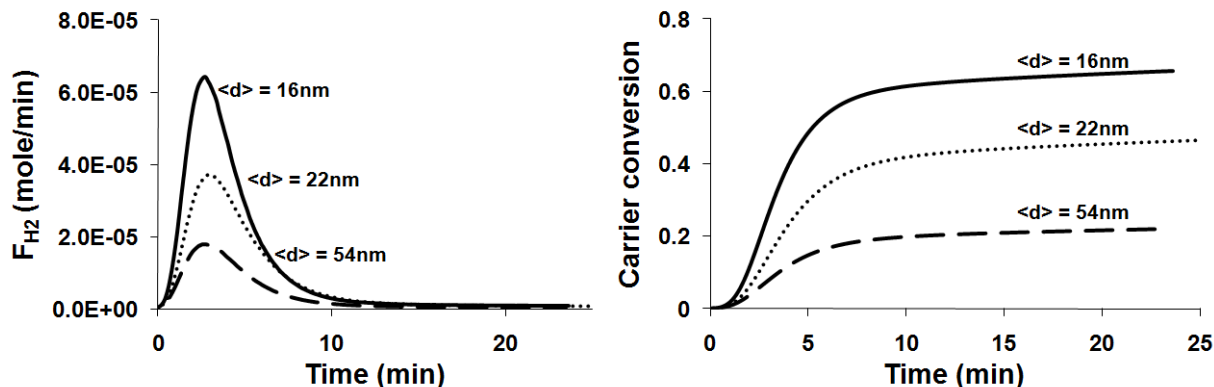


Figure 46. Effect of particle size of Fe on hydrogen production (left) and carrier conversion (right) at 800°C

These results underline the importance of nanosizing of the carrier for CLSR process and clearly indicate that in order to have > 65% carrier utilization the particle diameter should be less than 16nm. Achieving such a small particle size is not possible in the synthesis of BHA based carrier. However, it is well known that metals can have very small diameter (<10nm) when silica is used as support and thus silica based carrier can be a very good alternative to Fe-BHA, provided it is thermally stable at the operating conditions. Therefore, it is worthwhile to look at the performance of Fe supported on silica in CLSR which can be taken as a guideline for future research on CLSR.

5.3.4 Fixed bed reactor calculations

As a final step of the present proof-of-concept study, a fixed-bed reactor model was developed and analyzed in order to evaluate the feasibility of conducting CLSR in a periodically operated fixed-bed reactor. The analysis is built on a previously published model by Kuipers and coworkers who analyzed a similar periodic fixed-bed process for “conventional” chemical looping combustion of methane with air[68].

The choice of a fixed-bed reactor for CLSR processes is motivated on one hand by the intent to avoid carrier attrition issues, which pose a significant problem in circulating fluidized beds, as well as by the fact that the transition from the conventional air-blown chemical looping combustion process to a steam-fed chemical looping reforming process results in a strong reduction of the exothermicity of the overall reaction, and, depending on the fuel, can even result in endothermic net reactions. In contrast to the conventional CLC process, in which the strong heat release causes concerns due to excessive bed temperatures and the formation of hot spots[68], heat integration between the two half-reactions (i.e. oxidation of the fuel and reduction of H_2O) is therefore a beneficial, if not required, effect for efficient operation of CLSR. Cyclic operation of fixed-bed reactors has been shown to be a highly efficient and straight-forward way to achieve excellent heat-integration, even resulting in super-adiabatic temperatures at autothermal operation when using a reverse-flow configuration [69-72]. The current analysis, however, is limited to a periodically operated fixed bed configuration with co-current feed of syngas and steam, respectively.

The computations are based on a dynamical analysis of the pseudo-homogeneous energy balance for a fixed-bed process. Noorman et al. demonstrated that the energy balance can be solved analytically if a number of further simplifying assumptions are made, and we adapt the

solution for our steam reforming process discussed here[68]. Primary aim of the analysis is to identify the maximum temperature excursions in the bed, which can be directly derived from the energy balance using a number of simplifying assumptions: It is assumed that the carrier in the fixed bed is initially in its reduced form, and reacts with the steam instantaneously, i.e. with an infinitely fast reaction rate, until complete carrier conversion is attained. Similarly, instantaneous, complete reaction with syngas during the reduction phase is assumed. While neither assumption (infinite reaction rate and complete conversion) is strictly true in our case, as shown in the reactive tests in section 5.3.2, the analysis based on these assumptions will yield a conservative estimate for the maximum temperatures that can be expected in the process.

Due to the coupling between the gas-solid reaction and the convective gas flow, two spatially separated travelling fronts develop, which move through the reactor with different front velocities: The velocity of the heat front (v_h), where heat is transferred from the fixed bed to the gas phase, and the velocity of the reaction front (v_r), where the entire steam fed reacts with the oxygen carrier:

$$v_h = \frac{\rho_g v_g C_{p,g}}{\epsilon_s \rho_s C_{p,s}} \quad (1)$$

and

$$v_r = \frac{\rho_g v_g w_{g,H_2O}^{in} M_{act}}{\epsilon_s \rho_s w_{act} M_{H_2O} \xi} \quad (2)$$

(for the meaning of the variables please see section ‘Appendix B - Nomenclature’). It is assumed that the heat capacity of the gas and the solid ($C_{p,g}$ and $C_{p,s}$) and the solid density (ρ_s) are constant, and that the influence of pressure drop over the fixed bed and the variation of the mass flow rate can be neglected. Since the heat of reaction (ΔH_R) and specific heat capacity of the reactants ($C_{p,g}$) are only weakly dependent on temperature over the temperature range of interest,

average values for ΔH_R and $C_{P,g}$ were utilized and the calculations are not dependent on a specific reference temperature.

Assuming furthermore that the gas phase volumetric heat capacity is negligible, the heat produced by the oxidation of the oxygen carrier is taken up entirely by the solid carrier, and the energy balance can be written as

$$\frac{\rho_g v_g w_{g,H_2O}^{in}}{M_{H_2O}} (-\Delta H_R) = \varepsilon_s \rho_s C_{P,s} (v_r - v_h) (T_{\max} - T_0) \quad (3)$$

Substituting equations (1) and (2) in (3) and rearranging gives the maximum temperature rise in the bed:

$$\Delta T_{\max} = (T_{\max} - T_0) = \frac{-\Delta H_R}{\frac{C_{P,s} M_{act}}{w_{act} \xi} - \frac{C_{P,g} M_{H_2O}}{w_{g,H_2O}^{in}}} \quad (4)$$

As already pointed out by Noorman et al., this maximum temperature rise is independent of the gas flow rate (under the given assumptions)[68]. This is noteworthy, since it indicates that the fixed-bed reactor should be robust against changes in production capacity and hence offer a significant degree of flexibility with regard to hydrogen production rates. The key assumption which causes this decoupling of the maximum temperature rise from the gas flow is the negligible heat capacity of the gas phase in comparison to the solid phase, which results in negligible convective heat transport with the gas flow. Due to the large difference in volumetric heat capacities between gases and solids, this assumption can be expected to hold broadly.

Furthermore, equation (4) does not show any influence of the reaction rate. While this is simply a result of assuming an infinitely fast reaction in the derivation of the equation, Noorman et al. verified for their model of the chemical looping combustion of methane that the resulting analytical solution (eq. 4) shows little sensitivity to changes in the reaction rate coefficient (even

for changes by as much as a factor of 7) as long as the rate was sufficiently fast. This point further motivates the development of nanostructured Fe carriers for this process in order to achieve sufficiently fast kinetics and hence attain the flexibility and scalability suggested by these reactor modeling results.

Figure 47 (left) shows the maximum temperature change during the reduction of a FeO-based carrier (with syngas as fuel) along with the maximum temperature rise during oxidation of the carrier with steam and, for comparison, with air as a function of the weight fraction of FeO in the oxygen carrier. In agreement with results from our above discussed thermodynamic analysis of the carriers and our initial experimental results, we limit the redox process to $\text{FeO} \rightleftharpoons \text{Fe}_3\text{O}_4$ (i.e. the lowest and highest oxidation states, Fe and Fe_2O_3 , are not accessible).

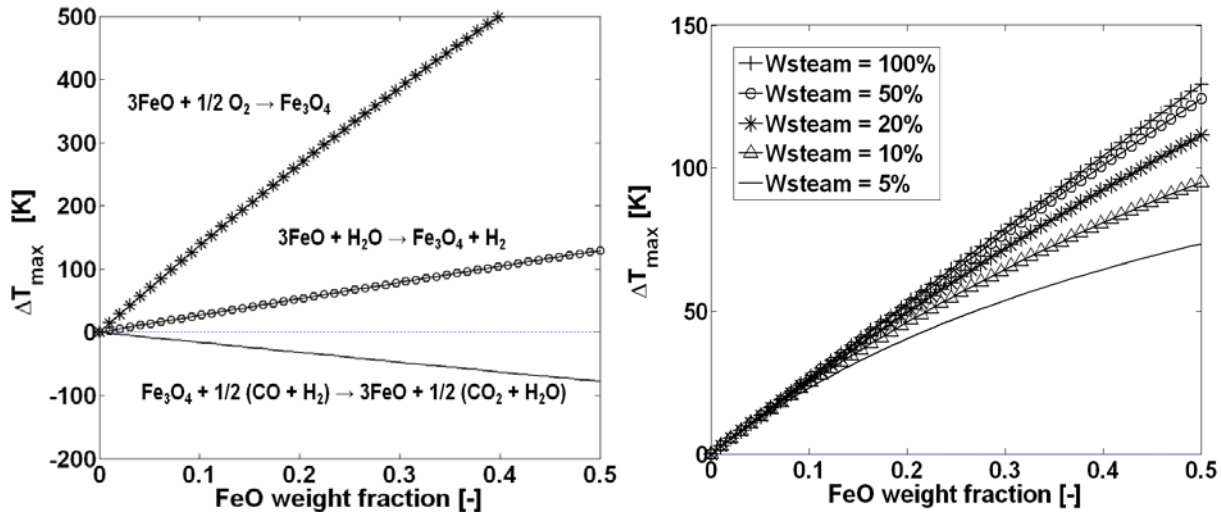


Figure 47. Maximum temperature difference during oxidation with air or steam, and during reduction with syngas as a function of FeO loading in the fixed bed (left graph); and maximum temperature rise during oxidation with different diluted steam streams (right graph; steam weight fraction increasing from 5% to 100% from bottom to top; the balance is inert gas)

As expected, replacing air with steam as oxidant results in a strong reduction in the maximum temperature rise during carrier oxidation. For FeO loadings below ~50% maximum temperature excursions remain below 150K, i.e. well below the >400K temperature rise observed

in the air-blown process, indicating that a fixed-bed reactor configuration should be possible without encountering problems due to heat accumulation or excessive hot spots during the oxidation phase. The results also show that the maximum temperature change during reduction of the carrier in contact with syngas is negative, i.e. the reduction of the carrier with syngas is endothermic, although the absolute value of the temperature change ($|\Delta T_{\max}| < 100$ K) is smaller than that of the temperature rise during the oxidation half-cycle, in agreement with the overall exothermal net reaction (WGS). This further supports the motivation to use a periodically operated fixed-bed for CLSR where the oxygen carrier acts a solid heat reservoir, allowing for efficient heat integration between the two half cycles of the process.

Another key result from the reactor analysis is shown in the right-hand graph in figure 47, where the maximum temperature rise versus FeO weight loading of the carrier is shown for several different mass fractions of steam in the oxidizing gas (the balance is assumed to be inert gas). It can be seen that reducing the steam content in the oxidizing gas to as little as 20wt% has very little effect on the maximum temperature. Obviously, operation with lower steam partial pressures is advantageous since condensation of steam becomes much less of a concern, particularly at high-pressure operation. However, this would also result in the dilution of the hydrogen/steam exit gas stream, which might again require separation of H_2 from a non-condensable inert gas, unless the dilution with an inert gas is tolerable for the intended application.

Overall, the reactor model analysis indicates that a periodically operated fixed-bed is a very well-suited configuration for chemical looping steam reforming. This reactor concept is much less sensitive to changes in feed flow, allows operation in much more compact reactors than a fluidized bed, and entirely avoids the issues associated with circulating fluidized beds,

such as gas-solid separation, particle attrition, and blow-out of powdered solids. The well-established heat-integration between the two half cycles in a periodically operated fixed-bed is a further benefit for CLSR due to the strongly reduced exothermicity in comparison to CLC.

5.4 SUMMARY

In this chapter, we reported on a feasibility study of a syngas-fed CLSR process in a periodically operated fixed bed reactor. This process results in a water-gas-shift reaction in which the two half steps – oxidation of CO and reduction of H_2O - are conducted in different half-cycles of the process, hence conceptually allowing the complete de-coupling of thermodynamics and kinetics. Our study combined thermodynamic screening of (monometallic) oxygen carriers with the synthesis and reactive evaluation of a nanostructured carrier, and a simplified fixed-bed reactor modeling study in order to establish the feasibility of the process.

Thermodynamic screening of a wide range of metals yielded the well-known Fe-based carriers as the best candidates based on thermodynamic limits during oxidation and reduction, melting point, toxicity, and cost. Based on these results, nanostructured Fe-BHA carriers were synthesized, and the reduction and oxidation kinetics of these carriers was evaluated in fixed-bed reactor studies. The studies demonstrated the thermal stability of the material in repeated cycles and showed fast kinetics during oxidation with steam. Most significantly, the reaction studies suggest that at temperatures as high as 800°C complete conversion of CO and high yields of H_2 should be attainable via appropriate timing of the half cycles. At this temperature, a “conventional” WGS process is constrained by severe thermodynamic limitations. The chemical looping-based process allows breaking these limitations in an elegant and efficient way.

Finally, a reactor model, originally developed by Kuipers and co-workers, was adapted to study the feasibility of CLSR of syngas in a periodically operated fixed-bed reactor configuration. The analysis supports the suitability of this reactor concept for CLSR by showing that heat accumulation and hot spots in the reactor bed are unlikely, and demonstrating a remarkable robustness of this reactor configuration against changes in operating conditions, such as throughput and dilution of the steam feed.

Overall, the present feasibility study thus strongly supports the proposition of “chemical looping steam reforming” of synthesis gas as an interesting alternative to conventional WGS, which allows for the production of ultra-pure hydrogen streams with simultaneous capture of CO₂ in separate effluent streams. Similar to “conventional” chemical looping combustion, CLSR is furthermore in principle fuel-flexible, i.e. it should be possible to operate this process with a wide range of fuels, including natural gas, coal, and biomass, making CLSR a highly promising process for the efficient, robust and fuel-flexible production of ultra-clean hydrogen streams.

6.0 SUMMARY AND OUTLOOK

6.1 SUMMARY

This work consists of three parts: In the first part thermodynamic evaluation of oxygen carriers for CLC of synthesis gas and natural gas was carried out. In the second part, based on the results of the thermodynamic study, we investigated CLC of sulfur contaminated synthesis gas; and in the third and final part we studied the application of chemical looping for hydrogen production. Every aspect of this work is important with respect to the energy production for the future. The major objective of this study was to understand the concept and challenges of these next-generation energy technologies and to come up with the most appropriate materials solutions. The study demonstrated that both the processes (CLC and CLSR) are inherently highly intensified and, with the appropriate choice of the material, have potential to get commercialized. Nevertheless a thorough process simulation is needed for detailed comparison with conventional processes.

6.1.1 CLC of sulfur contaminated synthesis gas

As fossil fuel reserves are depleting with time, refineries are being fed with more and more dirty fuel which contain high amount of sulfur contaminants. These sulfur contaminants interact strongly with the metals used in the different processes and therefore it is essential to come up

with either robust materials or alternative process routes. In this work we studied the impact of sulfur contaminants in the inlet fuel on the performance of CLC. We observed that both Ni-BHA and Cu-BHA interact strongly with the H_2S in inlet synthesis gas. Ni, Cu and BaO from support get sulfidized upon contact with H_2S at the operating conditions of CLC. For Ni and Cu sulfidation is reversible but support sulfidation is irreversible. It was observed that both Ni-BHA and Cu-BHA are very stable in repeated redox cycles of CLC of sulfur contaminated synthesis gas. Moreover an increase in oxygen carrying capacity was observed due to the participation of sulfidized support in the redox process.

Due to the cyclic nature of the process with an inherent re-oxidation step and robustness of the material to high sulfur contamination in the fuel it was anticipated that these BHA based carriers can be used for deep desulfurization of the inlet fuel while satisfying all the requirements of CLC. Based on this idea a novel scheme of integrating desulfurization with simultaneous CO_2 capture in CLC was proposed. Cu was chosen as the candidate for desulfurization due to its high affinity for sulfur. While Cu in Cu-BHA was able to capture >90% of inlet sulfur, the remaining sulfur came out as SO_2 during the reduction step due to the reduction of sulfidized support. Nevertheless this study suggests that with appropriate selection of the support (non-reducible and sulfur resistant) complete desulfurization of fuel with simultaneous CO_2 capture is feasible.

6.1.2 Hydrogen production via CLSR in periodically operated fixed bed reactor

Chemical looping combustion (CLC) is a promising technology for the clean combustion of fossil and renewable fuels with inherent air separation and CO_2 capture. By replacing air with steam as oxidizing gas, CLC can be converted into a chemical looping steam reforming process (CLSR) which conceptually allows for the fuel-flexible production of ultra-clean hydrogen

streams without the need for further purification steps. When synthesis gas is used as fuel, the overall process of CLSR turns out to be the conventional water gas shift (WGS) reaction. CLSR is able to break the thermodynamic barriers on WGS by breaking down the WGS in two separate reactions.

We studied the CLSR process by combination of thermodynamic evaluation, kinetic studies and a reactor model. Thermodynamic evaluation of carriers resulted in Fe as the best candidate for the CLSR process. It was observed that Fe-BHA is thermally stable and highly active in repeated redox cycles of CLSR in a fixed bed reactor. Finally, a reactor model was developed to study the feasibility of CLSR in a fixed bed reactor configuration. It was observed that hot spots are unlikely in a fixed bed process and there is a possibility of heat integration between the reduction and oxidation step. Overall CLSR of synthesis gas is a promising alternative to conventional WGS for the production of ultra-pure hydrogen with simultaneous CO₂ capture.

6.2 OUTLOOK

6.2.1 Non-reducible and sulfur resistant supports for CLC with sulfur capture

In chapter 4, we proposed a novel scheme of in-situ desulfurization of syngas in CLC. Our experimental study showed that Cu-BHA can capture 90% of the sulfur in inlet synthesis gas at 900°C, but remaining 10% comes out as SO₂ in the fuel reactor exhaust. As discussed in section 4.3.6, BaSO₄, formed by sulfidation of BaO in BHA, is reducible and hence reacts with the syngas. This reduces the availability of syngas for CuO reduction which makes CuO available

for SO_2 producing reaction. Thus, even though BHA is a very stable support in sulfur environment it is not good for in-situ desulfurization scheme. Clearly, a proper support which is sulfur resistant and non-reducible is needed for this scheme. Silica can be a good choice because it is non-reducible and sulfur resistant, but detailed experimental studies should be carried out in order to verify its thermal stability and, if any, effect of elemental sulfur deposition within the silica pores.

6.2.2 Fe supported on silica for CLSR

In chapter 5 we discussed a scheme of hydrogen production by chemical looping steam reforming (CLSR). Fe-BHA used in the experimental studies of CLSR suffers from diffusion limitations. Section 5.3.3 explains this effect in detail. With decreasing Fe particle size these diffusion limitations are minimized. However, for Fe-BHA the smallest attainable particle size is $\sim 15\text{nm}$ which is not enough for completely eliminating the diffusion limitations caused by Fe_3O_4 overlayer. Lower bound on the particle size is inherent in the synthesis and hence can not be avoided. Thus, in order to achieve Fe particle size less than 15nm one should select either a different synthesis route or a different support. Silica could be a good choice because metals supported on silica can have very small diameters. Fe particle size of $\sim 5\text{nm}$ can significantly reduce the diffusion limitations and can increase the carrier conversion beyond 90%. However, silica is not thermally stable at very high temperatures especially above 600°C therefore a thorough kinetic evaluation of silica based material is needed in order to verify its suitability for the high temperature redox environment of CLSR.

APPENDIX A

NANOCOMPOSITE OXYGEN CARRIER SYNTHESIS

Table 5. A typical recipe for Cu-BHA (40.04 wt% Cu) synthesis

<u>Microemulsion</u>		MW	moles	mass (g)	vol (ml)
PEPP	(surfactant)	2000.00	0.0050	10.0	--
Pentanol	(co-surfactant)	88.15	1.3213	116.5	142.9
Iso-octane	(oil phase)	114.23	0.2621	29.9	43.4
H ₂ O	(water)	18.00	0.4732	8.5	--
Cu(NO ₃) ₂ *2.5H ₂ O	(metal salt)	232.59	0.0143	3.332	--
<u>Metal Alkoxides</u>					
Al-Isopropoxide		204.24	0.0213	4.3572	--
Ba-Isopropoxide		255.51	0.0018	0.4599	--
Isopropanol		60.10	1.0885	65.42	83

BIBLIOGRAPHY

- [1] Halmann, M.; Steinberg, M. *Greenhouse Gas Carbon Dioxide Mitigation: Science and Technology*; Lewis Publishers: Boca Raton, FL, USA, 2000.
- [2] Lyngfelt, A.; Leckner, B.; Mattisson, T. A fluidized-bed combustion process with inherent CO₂ separation; application of chemical-looping combustion. *Chemical Engineering Science*, 56(10):3101-3113, 2001.
- [3] Leion, H.; Mattisson, T.; Lyngfelt, A. The use of petroleum coke as fuel in chemical-looping combustion. *Fuel*, 86(12-13):1947-1958, 2007.
- [4] Richter Horst, J.; Knoche Karl, F. In *Efficiency and Costing*; AMERICAN CHEMICAL SOCIETY: WASHINGTON, D.C., 1983, p 71-85.
- [5] Ishida, M.; Zheng, D.; Akehata, T. Evaluation of a chemical-looping-combustion power-generation system by graphic exergy analysis. *Energy*, 12(2):147-154, 1987.
- [6] Hossain, M. M.; de Lasa, H. I. Chemical-looping combustion (CLC) for inherent CO₂ separations--a review. *Chemical Engineering Science*, 63(18):4433-4451, 2008.
- [7] Anheden, M.; Svedberg, G. Exergy analysis of chemical-looping combustion systems. *Energy Conversion and Management*, 39(16-18):1967-1980, 1998.
- [8] Cho, P.; Mattisson, T.; Lyngfelt, A. Comparison of iron-, nickel-, copper- and manganese-based oxygen carriers for chemical-looping combustion. *Fuel*, 83(9):1215-1225, 2004.
- [9] Consonni, S.; Lozza, G.; Pelliccia, G.; Rossini, S.; Saviano, F. Chemical-Looping Combustion for Combined Cycles With CO₂ Capture. *Journal of Engineering for Gas Turbines and Power*, 128(3):525-534, 2006.
- [10] Wolf, J.; Anheden, M.; Yan, J. Comparison of nickel- and iron-based oxygen carriers in chemical looping combustion for CO₂ capture in power generation. *Fuel*, 84(7-8):993-1006, 2005.
- [11] Wolf, J.; Yan, J. Parametric study of chemical looping combustion for tri-generation of hydrogen, heat, and electrical power with CO₂ capture. *International Journal of Energy Research*, 29(8):739-753, 2005.

- [12] Mattisson, T.; Johansson, M.; Lyngfelt, A. The use of NiO as an oxygen carrier in chemical-looping combustion. *Fuel*, 85(5-6):736-747, 2001.
- [13] Mattisson, T.; Lyngfelt, A.; Cho, P. The use of iron oxide as an oxygen carrier in chemical-looping combustion of methane with inherent separation of CO₂. *Fuel*, 80(13):1953-1962, 2001.
- [14] Mattisson, T.; Johansson, M.; Lyngfelt, A. Multicycle Reduction and Oxidation of Different Types of Iron Oxide Particles Application to Chemical-Looping Combustion. *Energy & Fuels*, 18(3):628-637, 2004.
- [15] Mattisson, T.; García-Labiano, F.; Kronberger, B.; Lyngfelt, A.; Adánez, J.; Hofbauer, H. Chemical-looping combustion using syngas as fuel. *International Journal of Greenhouse Gas Control*, 1(2):158-169, 2007.
- [16] Jerndal, E.; Mattisson, T.; Lyngfelt, A. Thermal Analysis of Chemical-Looping Combustion. *Chemical Engineering Research and Design*, 84(9):795-806, 2006.
- [17] Adánez, J.; de Diego, L. F.; García-Labiano, F.; Gayán, P.; Abad, A.; Palacios, J. M. Selection of Oxygen Carriers for Chemical-Looping Combustion. *Energy & Fuels*, 18(2):371-377, 2004.
- [18] Mattisson, T.; Järnäs, A.; Lyngfelt, A. Reactivity of Some Metal Oxides Supported on Alumina with Alternating Methane and Oxygen Application for Chemical-Looping Combustion. *Energy & Fuels*, 17(3):643-651, 2003.
- [19] Ishida, M.; Jin, H. CO₂ recovery in a power plant with chemical looping combustion. *Energy Conversion and Management*, 38(Supplement 1):S187-S192, 1997.
- [20] Ishida, M.; Jin, H.; Okamoto, T. Kinetic Behavior of Solid Particle in Chemical-Looping Combustion: Suppressing Carbon Deposition in Reduction. *Energy & Fuels*, 12(2):223-229, 1998.
- [21] Jin, H.; Okamoto, T.; Ishida, M. Development of a Novel Chemical-Looping Combustion: Synthesis of a Solid Looping Material of NiO/NiAl₂O₄. *Industrial & Engineering Chemistry Research*, 38(1):126-132, 1998.
- [22] Cho, P.; Mattisson, T.; Lyngfelt, A. Carbon Formation on Nickel and Iron Oxide-Containing Oxygen Carriers for Chemical-Looping Combustion. *Industrial & Engineering Chemistry Research*, 44(4):668-676, 2005.
- [23] Cho, P.; Mattisson, T.; Lyngfelt, A. Defluidization Conditions for a Fluidized Bed of Iron Oxide-, Nickel Oxide-, and Manganese Oxide-Containing Oxygen Carriers for Chemical-Looping Combustion. *Industrial & Engineering Chemistry Research*, 45(3):968-977, 2005.

- [24] Ryu, H.-J.; Bae, D.-H.; Han, K.-H.; Lee, S.-Y.; Jin, G.-T.; Choi, J.-H. Oxidation and reduction characteristics of oxygen carrier particles and reaction kinetics by unreacted core model. *Korean Journal of Chemical Engineering*, 18(6):831-837, 2001.
- [25] Zafar, Q.; Mattisson, T.; Gevert, B. Redox Investigation of Some Oxides of Transition-State Metals Ni, Cu, Fe, and Mn Supported on SiO₂ and MgAl₂O₄. *Energy & Fuels*, 20(1):34-44, 2005.
- [26] Corbella, B. M.; Palacios, J. M. Titania-supported iron oxide as oxygen carrier for chemical-looping combustion of methane. *Fuel*, 86(1-2):113-122, 2007.
- [27] Galvita, V.; Schröder, T.; Munder, B.; Sundmacher, K. Production of hydrogen with low CO_x-content for PEM fuel cells by cyclic water gas shift reactor. *International Journal of Hydrogen Energy*, 33(4):1354-1360, 2008.
- [28] Otsuka, K.; Yamada, C.; Kaburagi, T.; Takenaka, S. Hydrogen storage and production by redox of iron oxide for polymer electrolyte fuel cell vehicles. *International Journal of Hydrogen Energy*, 28(3):335-342, 2003.
- [29] Gupta, P.; Velazquez-Vargas, L. G.; Fan, L.-S. Syngas Redox (SGR) Process to Produce Hydrogen from Coal Derived Syngas. *Energy & Fuels*, 21(5):2900-2908, 2007.
- [30] Messerschmitt, Verfahren zur Erzeugung von Wasserstoff durch abwechselnde Oxidation und Reduktion von Eisen in von außen beheizten, in den Heizräumen angeordneten Zersetzern, German Patent DE 266863, Germany, 1911
- [31] Hacker, V.; Fankhauser, R.; Faleschini, G.; Fuchs, H.; Friedrich, K.; Muhr, M.; Kordes, K. Hydrogen production by steam-iron process. *Journal of Power Sources*, 86(1-2):531-535, 2000.
- [32] Huffman, G. P.; Wender, I. Fuel science in the year 2000: an introduction. *Fuel Processing Technology*, 71(1-3):1-6, 2001.
- [33] Hurst, S. Production of hydrogen by the steam-iron method. *Journal of the American Oil Chemists' Society*, 16(2):29-35, 1939.
- [34] Rydén, M.; Lyngfelt, A. Using steam reforming to produce hydrogen with carbon dioxide capture by chemical-looping combustion. *International Journal of Hydrogen Energy*, 31(10):1271-1283, 2006.
- [35] Matar, S.; Hatch, L. F. *Chemistry of petrochemical processes, second edition*; Gulf professional publishing, 2001.
- [36] Wolf, J.; Anheden, M.; Yan, J. In *International Pittsburgh Coal Conference* Newcastle, New South Wales, Australia 2001.

- [37] Copeland, R.; Alptekin, G.; Cessario, M.; Gerhanovich, Y. In *Proceedings of the first national conference on carbon sequestration* Washington, DC, 2001.
- [38] H., L. The utilization of natural gas for ammonia process. *Transactions of the Faraday Society*, 25(462-472, 1929.
- [39] Ashcroft, A. T.; Cheetham, A. K.; Foord, J. S.; Green, M. L. H.; Grey, C. P.; Murrell, A. J.; Vernon, P. D. F. Selective oxidation of methane to synthesis gas using transition metal catalysts. *Nature*, 344(6264):319-321, 1990.
- [40] Ashcroft, A. T.; Cheetham, A. K.; Green, M. L. H.; Vernon, P. D. F. Partial oxidation of methane to synthesis gas using carbon dioxide. *Nature*, 352(6332):225-226, 1991.
- [41] Bartholomew, C. H. Mechanisms of catalyst deactivation. *Applied Catalysis A: General*, 212(1-2):17-60, 2001.
- [42] García-Labiano, F.; Adánez, J.; de Diego, L. F.; Gayán, P.; Abad, A. Effect of Pressure on the Behavior of Copper-, Iron-, and Nickel-Based Oxygen Carriers for Chemical-Looping Combustion. *Energy & Fuels*, 20(1):26-33, 2005.
- [43] Tian, H.; Guo, Q.; Chang, J. Investigation into Decomposition Behavior of CaSO₄ in Chemical-Looping Combustion. *Energy & Fuels*, 22(6):3915-3921, 2008.
- [44] Song, Q.; Xiao, R.; Deng, Z.; Shen, L.; Xiao, J.; Zhang, M. Effect of Temperature on Reduction of CaSO₄ Oxygen Carrier in Chemical-Looping Combustion of Simulated Coal Gas in a Fluidized Bed Reactor. *Industrial & Engineering Chemistry Research*, 47(21):8148-8159, 2008.
- [45] Krylov, O. V. Catalytic reactions of partial methane oxidation. *Catalysis Today*, 18(3):209-302, 1993.
- [46] Buyevskaya, O. V.; Wolf, D.; Baerns, M. Rhodium-catalyzed partial oxidation of methane to CO and H₂. Transient studies on its mechanism. *Catalysis Letters*, 29(1):249-260, 1994.
- [47] Mallens, E. P. J.; Hoebink, J. H. B. J.; Marin, G. B. An investigation on the reaction mechanism for the partial oxidation of methane to synthesis gas over platinum. *Catalysis Letters*, 33(3):291-304, 1995.
- [48] De Groote, A. M.; Froment, G. F. Simulation of the catalytic partial oxidation of methane to synthesis gas. *Applied Catalysis A: General*, 138(2):245-264, 1996.
- [49] Otsuka, K.; Wang, Y.; Sunada, E.; Yamanaka, I. Direct Partial Oxidation of Methane to Synthesis Gas by Cerium Oxide. *Journal of Catalysis*, 175(2):152-160, 1998.
- [50] Hu, Y. H.; Ruckenstein, E. Catalytic Conversion of Methane to Synthesis Gas by Partial Oxidation and CO₂ Reforming. *ChemInform*, 35(49):2004.

- [51] Freni, S.; Calogero, G.; Cavallaro, S. Hydrogen production from methane through catalytic partial oxidation reactions. *Journal of Power Sources*, 87(1-2):28-38, 2000.
- [52] Mattisson, T.; Johansson, M.; Lyngfelt, A. The use of NiO as an oxygen carrier in chemical-looping combustion. *Fuel*, 85(5-6):736-747, 2001
- [53] Sedor, K. E.; Hossain, M. M.; de Lasa, H. I. Reactivity and stability of Ni/Al₂O₃ oxygen carrier for chemical-looping combustion (CLC). *Chemical Engineering Science*, 63(11):2994-3007, 2008.
- [54] Wang, B.; Yan, R.; Lee, D. H.; Liang, D. T.; Zheng, Y.; Zhao, H.; Zheng, C. Thermodynamic Investigation of Carbon Deposition and Sulfur Evolution in Chemical Looping Combustion with Syngas. *Energy & Fuels*, 22(2):1012-1020, 2008.
- [55] Kirchhoff, M.; et al. Engineering high-temperature stable nanocomposite materials. *Nanotechnology*, 16(7):S401, 2005.
- [56] Tian, H.; Chaudhari, K.; Simonyi, T.; Poston, J.; Liu, T.; Sanders, T.; Veser, G. t.; Siriwardane, R. Chemical-looping Combustion of Coal-derived Synthesis Gas Over Copper Oxide Oxygen Carriers. *Energy & Fuels*, 22(6):3744-3755, 2008.
- [57] Liu, T.; Simonyi, T.; Sanders, T.; Siriwardane, R.; Veser, G. Nanocomposite Oxygen Carriers for Chemical-looping Combustion. *ACS Fuel Chemistry Preprints*, 51(2):2006.
- [58] Liu, T.; Simonyi, T.; Sanders, T.; Siriwardane, R.; Veser, G. in preparation. 2010.
- [59] Solunke, R.; Veser, G. Nanocomposite Oxygen Carriers for Chemical-Looping Combustion of Sulfur-Contaminated Synthesis Gas. *Energy & Fuels*, 23(10):4787-4796, 2009.
- [60] Machida, M.; Eguchi, K.; Arai, H. Effect of additives on the surface area of oxide supports for catalytic combustion. *Journal of Catalysis*, 103(2):385-393, 1987.
- [61] Arai, H.; Machida, M. Thermal stabilization of catalyst supports and their application to high-temperature catalytic combustion. *Applied Catalysis A: General*, 138(2):161-176, 1996.
- [62] Garcia-Labiano, F.; de Diego, L. F.; Adanez, J.; Abad, A.; Gayan, P. Reduction and Oxidation Kinetics of a Copper-Based Oxygen Carrier Prepared by Impregnation for Chemical-Looping Combustion. *Industrial & Engineering Chemistry Research*, 43(26):8168-8177, 2004.
- [63] Abad, A.; Mattisson, T.; Lyngfelt, A.; Johansson, M. The use of iron oxide as oxygen carrier in a chemical-looping reactor. *Fuel*, 86(7-8):1021-1035, 2007.
- [64] Yasyerli, S.; Dogu, G.; Ar, I.; Dogu, T. Activities of Copper Oxide and Cu^{II}V and Cu^{II}Mo Mixed Oxides for H₂S Removal in the Presence and Absence of Hydrogen and

Predictions of a Deactivation Model. *Industrial & Engineering Chemistry Research*, 40(23):5206-5214, 2001.

[65] Pike, J.; Chan, S.-W.; Zhang, F.; Wang, X.; Hanson, J. Formation of stable Cu₂O from reduction of CuO nanoparticles. *Applied Catalysis A: General*, 303(2):273-277, 2006.

[66] Solunke, R. D.; Vesper, G. Nanocomposite Oxygen Carriers for Chemical-Looping Combustion of Sulfur-Contaminated Synthesis Gas†. *Energy & Fuels*, 23(10):4787-4796, 2009.

[67] Cheng, X.; Shi, Z.; Glass, N.; Zhang, L.; Zhang, J.; Song, D.; Liu, Z.-S.; Wang, H.; Shen, J. A review of PEM hydrogen fuel cell contamination: Impacts, mechanisms, and mitigation. *Journal of Power Sources*, 165(2):739-756, 2007.

[68] Noorman, S.; van Sint Annaland, M.; Kuipers. Packed Bed Reactor Technology for Chemical-Looping Combustion. *Industrial & Engineering Chemistry Research*, 46(12):4212-4220, 2007.

[69] Eigenberger, G.; Niekens, U. Catalytic combustion with periodic flow reversal. *Chemical Engineering Science*, 43(8):2109-2115, 1988.

[70] Neumann, D.; Gepert, V.; Vesper, G. Some Considerations on the Design and Operation of High-Temperature Catalytic Reverse-Flow Reactors. *Industrial & Engineering Chemistry Research*, 43(16):4657-4667, 2004.

[71] Neumann, D.; Vesper, G. Catalytic partial oxidation of methane in a high-temperature reverse-flow reactor. *AIChE Journal*, 51(1):210-223, 2005.

[72] Liu, T.; Temur, H.; Vesper, G. Autothermal Reforming of Methane in a Reverse-Flow Reactor. *Chemical Engineering & Technology*, 32(9):1358-1366, 2009.